Internal Variability
in the Regional Climate Model
REMO

Kevin Sieck

Hinweis

Die Berichte zur Erdsystemforschung werden vom Max-Planck-Institut für Meteorologie in Hamburg in unregelmäßiger Abfolge herausgegeben.

Sie enthalten wissenschaftliche und technische Beiträge, inklusive Dissertationen.

Die Beiträge geben nicht notwendigerweise die Auffassung des Instituts wieder.

Die "Berichte zur Erdsystemforschung" führen die vorherigen Reihen "Reports" und "Examensarbeiten" weiter.

Notice

The Reports on Earth System Science are published by the Max Planck Institute for Meteorology in Hamburg. They appear in irregular intervals.

They contain scientific and technical contributions, including Ph. D. theses.

The Reports do not necessarily reflect the opinion of the Institute.

The "Reports on Earth System Science" continue the former "Reports" and "Examensarbeiten" of the Max Planck Institute.

Anschrift / Address

Max-Planck-Institut für Meteorologie
Bundesstrasse 53
20146 Hamburg
Deutschland

Tel.: +49-(0)40-4 11 73-0
Fax: +49-(0)40-4 11 73-298
Web: www.mpimet.mpg.de

Layout:

Bettina Diallo, PR & Grafik

Titelfotos:
vorne:
Christian Klepp - Jochem Marotzke - Christian Klepp
hinten:
Clotilde Dubois - Christian Klepp - Katsumasa Tanaka

Internal Variability
in the Regional Climate Model
REMO

Kevin Sieck

aus Hamburg

Hamburg 2013

Kevin Sieck
Max-Planck-Institut für Meteorologie
Bundesstrasse 53
20146 Hamburg

Als Dissertation angenommen
vom Department Geowissenschaften der Universität Hamburg

auf Grund der Gutachten von
Prof. Dr. Martin Claussen
und
Dr. Daniela Jacob

Hamburg, den 11. November 2013
Prof. Dr. Christian Betzler
Leiter des Departments für Geowissenschaften

Internal Variability
in the Regional Climate Model
REMO
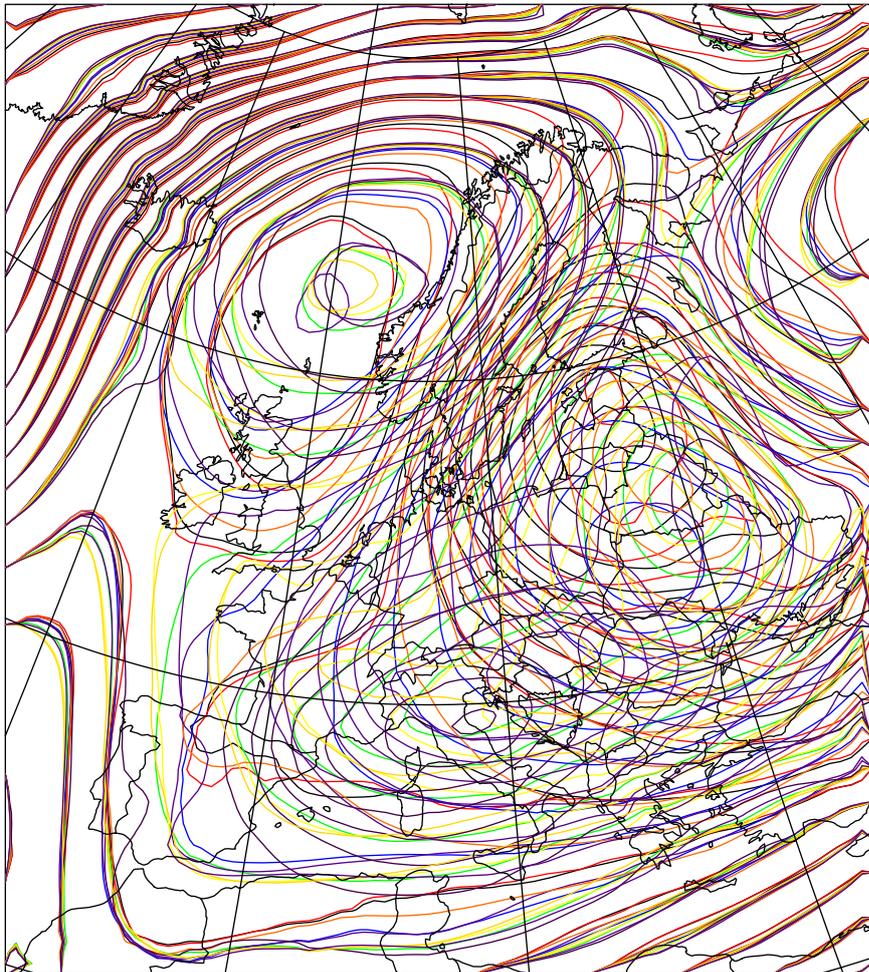
Kevin Sieck

Hamburg 2013

Summary

Internal variability in regional climate models has been discussed in the literature for more than a decade, but still many open questions remain. In this study, a ten member ensemble of the regional climate model REMO is used to investigate internal variability on a European domain. The temporal evolution of internal variability shows the typical episodic evolution known from other studies in the mid-latitudes. In Europe, however, distinct maximums in seasonal mean internal variability of mean-sea-level pressure and near-surface temperature appear in winter and spring that have not been reported for domains of the size in the present study. A circulation type analysis performed on the boundary data shows that the variability of the large-scale forcing, namely the prevailing weather regime, is closely connected to the domain average internal variability especially in winter. The most pronounced differences are found between NAO negative and positive like circulation patterns. A correlation between a daily NAO index and daily domain averaged internal variability produced a Pearson correlation of 0.51 over the extended winter season from October to March. From the close connection between jet stream strength and NAO a simple internal variability index is constructed using the zonal wind speed in 500 hPa from the forcing data. Results show a correlation of up to 0.7 between zonal wind and domain averaged internal variability. This makes it possible to diagnose internal variability episodes already from the forcing data without running an entire ensemble to get an estimate for the internal variability which is needed to be able to judge on the significance of regional climate informations.

Zusammenfassung

Interne Variabilität in regionalen Klimamodellen war ein wichtiges Thema der Fachliteratur während der vergangenen zehn Jahre. Viele Fragen sind dennoch offen geblieben. Ein Ensemble des regionalen Klimamodells REMO bestehend aus zehn Simulation wird verwendet, um die interne Variabilität regionaler Klimamodelle über Europa zu untersuchen. Der zeitliche Verlauf der internen Variabilität zeigt den von anderen Studien bekannten für die mittleren Breiten typischen episodischen Charakter. In Europa jedoch treten sowohl im reduziertem Bodendruck im Winter als auch der bodennahen Temperatur im Frühjahr ausgeprägte Maxima in der saisonal gemittelten internen Variabilität auf. Maxima zu diesen Jahreszeiten wurden bislang in keiner anderen Studie erwähnt, die Modellgebiete ähnlicher Größe untersucht hat. Eine Wetterlagenklassifikation der Randdaten zeigt, dass besonders im Winter die Variabilität der Randdaten eng mit der räumlich gemittelten internen Variabilität des Modellgebiets zusammenhängt. Die größten Unterschiede ergeben sich hierbei zwischen Zirkulationsmustern, die der positiven und negativen Phase der NAO ähnlich sehen. Die Korrelation eines täglichen NAO Index und der internen Variabilität gemittelt über das Modellgebiet ergibt einen Koeffizienten von 0.51 für das Winterhalbjahr von Oktober bis März. Aus dem engen Zusammenhang zwischen der NAO und der stärke des polaren Strahlstroms wird mit Hilfe der zonalen Windgeschwindigkeit in $500\,\text{hPa}$ aus den Randdaten ein einfacher interner Variabilitäts-Index entwickelt. Ergebnisse zeigen, dass eine Korrelation von bis zu 0.7 zwischen zonaler Windgeschwindigkeit und räumlich gemittelter interner Variabilität besteht. Daraus ergibt sich die Möglichkeit, die interne Variabilität eines regionalen Klimamodells nur mit Hilfe der Randdaten abzuschätzen, was für die Einschätzung der Signifikanz regionaler Klimasignale wichtig ist.

Contents

References   **115**

Acknowledgements   **125**

List of Tables

List of Figures

List of Abbreviations and Acronyms

AMO Atlantic Multidecadal Oscillation

CMIP Coupled Model Intercomparison Project

CORDEX Coordinated Regional Climate Downscaling Experiment

COST European Cooperation in Science and Technology

DWD Deutscher Wetterdienst (German Weather Service)

ECHAM ECMWF Hamburg model

ECHAM4.5 Version 4.5 of ECHAM

ECHAM5-HAM Version 5 of ECHAM with HAM extension

ECMWF European Centre for Medium-Range Weather Forecasts

ECV Explained Cluster Variance

ENSO El Nino Southern Oscillation

EOF Empirical Orthogonal Function

ERA-40 ECMWF 40 year re-analysis

ERA-15 ECMWF 15 year re-analysis

EUROCORDEX European part of CORDEX

GCM General Circulation Model, commonly referred to as Global Climate Model

HAM Hamburg Aerosol Model

IPCC Intergovernmental Panel on Climate Change

MERCURE Modelling European Regional Climate: Understanding and Reducing Errors

MiKlip Mittelfristige Klimaprognosen (Decadal Predictions)

MSLP Mean-sea-level pressure

NAO North-Atlantic Oscillation

NCEP National Centers for Environmental Prediction

NST Near-surface temperature

RCM Regional Climate Model

RCP Representative Concentration Pathway

REMO Regional Model

REMO5.0 Version 5.0b of REMO

REMO-HAM REMO with HAM extension

SANDRA Simulated Annealing and Diversified Randomization clustering

TFP Thermal Front Parameter

Chapter 1

Introduction

Regional climate models are frequently used and widely accepted tools for current climate simulations and future climate change projections because of their consistent representation of physical processes at a high resolution. These models are integrated on a limited domain and obtain their initial and boundary conditions from global climate models or gridded analysis of observations. In this way, a regional climate model acts as a magnifying glass to deliver climate information on the regional to local scale that are often needed in, e.g., climate change impact studies. To deliver robust information, it is of importance to study their uncertainties. Apart from uncertainties introduced by the boundary conditions and model formulations, it has been shown that regional climate models are subject to uncertainties that stem from processes intrinsic to the model (see, e.g., Laprise et al., 2008, 2012, and references therein). In this study, this form of uncertainty, referred to as the *internal variability* of a regional climate model, is investigated for a domain located over Europe. It is shown, how internal variability changes with season and how it depends on the variability of the boundary conditions. Furthermore, it is demonstrated how the variability of the boundary conditions can be used to determine the strength of internal variability from the prevailing weather regime.

Before climate change impacts can be assessed, typically an entire *modeling chain* is followed (Jacob, 2009). The modeling chain usually starts with a climate change scenario and continues with one global and one to multiple regional climate modeling steps (see Figure 1.1). A large part of the uncertainty already lies in the construction of the climate change scenarios because of unknown future human activities such as the emission of greenhouse gases or land-use changes. In studies on future climate
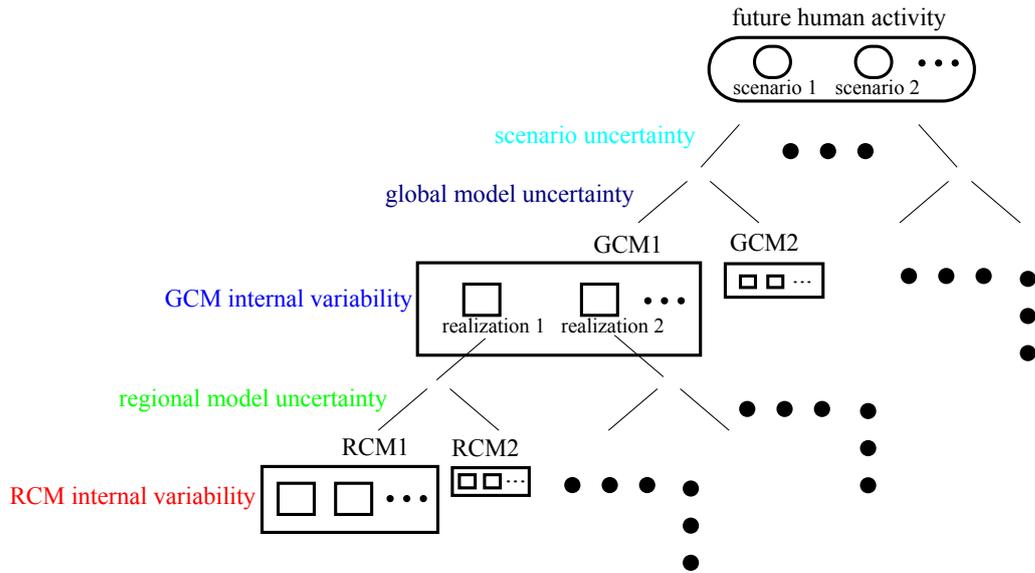
Figure 1.1: The model chain and it's uncertainties from the perspective of a regional climate modeler. Each climate modeling step (rectangular boxes) can be split up into forcing uncertainty, model uncertainty, and internal variability. The three corresponding components for a global climate model – scenario uncertainty, global model uncertainty, and global model internal variability – form the forcing uncertainty for the regional model. At the regional scale, regional model uncertainty and regional internal variability complete the set of uncertainties that influence regional climate variability.

change that entered the fourth assessment report of the *Intergovernmental Panel on Climate Change* (IPCC) the *scenario uncertainty*, as this is referred to, was tackled by several equally plausible emission scenarios based on storylines of possible future human activity (SRES, 2000). The problem of scenario uncertainty is tackled differently in the upcoming fifth assessment report. In this report, only *representative concentration pathways* (RCPs) are considered, which do not describe full scenarios respectively storylines. The basis is formed by a range of radiative forcing values for the year 2100 from which integrated assessment models calculate the necessary input data for climate models such as land use and emissions (Vuuren et al., 2011). This method enables a parallelization of the climate modeling and scenario developing process, but still results in a scenario uncertainty in the sense of an uncertainty range of different radiative forcings.

For each climate modeling chain link, the uncertainties can be categorized into three main parts: forcing, model response and internal variability (e.g., Tebaldi and Knutti, 2007). For global climate models, the *forcing uncertainty* stems from *scenario uncertainty* as well as from unknown changes in future natural forcings such

as volcanic eruptions or changes in solar activity. Scenario uncertainty is tackled simply by running multiple emission scenarios with the same global climate model. Although it has been shown that large volcanic eruptions have the potential to influence the climate on multidecadal time scales (see Timmreck, 2012, for a review), changes in future natural forcings are typically not considered, as their influence is usually treated as low compared to the influence from human activities.

Model uncertainty is expressed by different responses of climate models to the same external forcing (Deser et al., 2012). Many processes in the climate system such as convection or turbulence have to be parameterized as they can not be resolved. This produces differences in the solutions of climate models and is sometimes referred to as *structural uncertainty* (Palmer and Williams, 2009). Assuming that different modeling centers develop their global climate models independently, and that their errors are distributed randomly, a suit of models can be run in inter-comparison projects to tackle the problem of structural uncertainty, as in the case of the Coupled Model Intercomparison Project (CMIP). Although models are usually not developed completely independently, this *multi-model approach* has proven to be a successful tool to tackle model errors (e.g., Hagedorn et al., 2005; Tebaldi and Knutti, 2007).

Internal variability of a global climate model derives from the chaotic nature of the climate system (e.g. Hasselmann, 1976), which is why it is also often referred to as *natural variability* or *natural internal variability.* Complex interactions between different components of the climate system such as atmosphere and ocean, result in low frequency fluctuations around a mean state, thus causing internal variability. Some prominent examples for these fluctuations are the El Nino Southern Oscillation (ENSO) or the Atlantic Multidecadal Oscillation (AMO). Internal variability is usually estimated from modeling studies as observational records are too short and influenced by external forcings such as the solar cycle. In model studies, internal variability is estimated from long time integrations with fixed (often preindustrial) external forcings (Collins et al., 2001). In climate change projections, however, internal variability is usually estimated from a couple of realizations from one model using the same forcing but perturbed initial conditions.

In the case of regional climate models, the above listed uncertainties can be viewed as the forcing uncertainty. The problem is that there is no metric of how to combine these uncertainties and include them into the forcing of regional climate models. In principle, one would have to run all scenarios from all global climate model realizations to cover the entire range of uncertainties for regional climate change studies.

In practice, this procedure is not feasible. In addition, regional climate models are subject to model uncertainty as well, although Deque et al. (2007) found that forcing uncertainty is typically larger than model uncertainty in regional climate models. Nevertheless model uncertainty is not negligible and a multi-model approach is followed similar to CMIP. In the European Commission's 6th Framework Programme project ENSEMBLES, a global climate model/regional climate model matrix was set up, to cover the uncertainty range of one scenario but different global climate model/regional climate model combinations.

In the past decade, an awareness that regional climate models are subject to internal variability has risen. This finding means that although a regional climate model is constrained by it's lateral boundary conditions that impose the large-scales on to the regional model, the self-generated fine-scale motions do not have a unique solution (Laprise et al., 2012). The term internal variability, in this manner, should not be confused with the internal variability of a global climate model (Bellprat et al., 2012). The most important difference between them is that regional climate models are constantly forced by time-varying boundary conditions (or a time varying external forcing), which is different to the definition for a global climate model that requires a constant forcing (Collins et al., 2001). Still, a regional model shows a certain sensitivity to its initial conditions that are intrinsic to the model similar to global models and, therefore, the term internal variability is used for regional models as well. In addition, the procedure to get an estimate of internal variability from a regional model is similar to the method used to estimate internal variability in global model climate change projections.

As long as model domains of regional climate models are small, their internal variability contributes only marginally to the entire modeling chain. In recent years, with increasing computer power, domain sizes have grown larger. Lucas-Picher et al. (2008b) and Braun et al. (2012) have shown that in such cases the internal variability of a regional climate model can play an important role in the uncertainty of the downscaled climate information. This uncertainty is especially true for parameters important to the hydrological cycle. Christensen et al. (2001) already show that the internal variability of a regional climate model can become as large as internal variability in a global climate model when only one season is considered. Weisse et al. (2000) found in a sensitivity study that large differences between two ensembles of slightly modified model versions, often occur simultaneously with large internal variability within the ensembles themselves. They conclude that the comparison between only two runs, e.g., in sensitivity studies, can be misleading due to internal

variability.

The strength of internal variability in a regional climate model is sensitive to a number of factors. Alexandru et al. (2007) showed that a sufficiently big domain can enhance internal variability. If local processes play an important role, the internal variability of certain parameters such as precipitation, mean-sea-level pressure or near-surface temperature can grow large in a regional climate model (e.g., Giorgi and Bi, 2000; Caya and Biner, 2004). In addition, the location of the domain on the globe and the season plays a role for the strength of internal variability (e.g., Giorgi and Bi, 2000; Christensen et al., 2001; Caya and Biner, 2004; Rinke and Dethloff, 2000; Lucas-Picher et al., 2008b; Laprise et al., 2012). Lucas-Picher et al. (2008a) show that, for a domain over North-America, the flow regime of the external forcing governs the internal variability of a regional climate model as an additional factor. They also point out that the findings might change for different regions of the world. Laprise et al. (2012) found that the temporal evolution of internal variability undergoes certain episodes of stronger and weaker internal variability and that it is not a phenomenon specific to one model.

In an attempt to quantify important processes that create internal variability during summer, Nikiema and Laprise (2011) derived equations to compute tendencies of potential temperature and relative vorticity internal variability. They found that for potential temperature deviations between ensemble members, condensation and convection play the most important role in generating potential temperature internal variability. With regards to the internal variability of relative vorticity, it is mainly the transport of relative vorticity itself and the horizontal wind fluctuations that contribute to its generation. A case study by Diaconescu et al. (2012) shows that hydrodynamic instabilities associated with baroclinic processes play an important role in the rapid growth of internal variability during their investigated episode in December 1992.

Most of the studies on internal variability in the mid-latitudes concentrated on the North-American continent. For Europe, a systematic study on internal variability is still lacking. In addition, the connection between weather regimes and internal variability of a regional climate model has not been investigated for the mid-latitudes. Furthermore, no attempt to infer from the lateral boundary forcing on the strength of internal variability in a regional climate model has been made. In this study, these gaps are closed by answering the following research questions:

- *How does internal variability change with season over Europe?*

- *How do weather regimes influence the internal variability of a regional climate model throughout different seasons?*

- *Is it possible to determine the strength of internal variability from the variability of the boundary data?*

The thesis is structured as follows; after introducing the regional climate model REMO and the analysis method in Chapter 2, the characteristics of internal variability of REMO for different seasons on a domain over Europe is covered in Chapter 3. The connection of internal variability to weather regimes for different seasons using a circulation type analysis is investigated in Chapter 4. How this relation can be used to infer on the strength of internal variability during the winter season is presented in Chapter 5. A summary of the results including a comprehensive discussion, concluding remarks, and an outlook is given in Chapter 6.

Chapter 2

Experimental Set-up and Analysis Method

All simulations to investigate internal variability in a regional climate model over Europe were carried out with the regional climate model REMO (REgional MOdel), developed at the Max Planck Institute for Meteorology (Jacob and Podzun, 1997). In this study, version 5.0b (referred to as REMO5.0 hereafter) is used. The advantage of using REMO5.0 is that it is both well tested and computational efficient allowing for several ensemble members to be run in a relatively short time. As more fundamental issues of regional climate modeling are investigated in this study, the results are not expected to change with different model versions or even different regional climate models and can be generalized as also pointed out by Laprise et al. (2012). In Section 2.1 REMO5.0 is described in detail with a summary of additions to the model since then. This is followed by the explanations of the experimental set-up and analysis methods in Sections 2.2 and 2.3.

2.1   The Regional Climate Model REMO

The regional climate model REMO is a limited-area hydrostatic three-dimensional model of the atmosphere. It consists of two major parts. The first part, commonly called dynamical core, solves the primitive equations of the atmosphere (e.g. Holton, 2004). The dynamical core originates from the former weather forecasting model *Europamodell* (Majewski, 1991) of the Deutscher Wetterdienst (German Weather Service) (DWD). The second part consists of the parameterization schemes,

that describe important physical processes that are not resolved by the dynamical core. To allow for climate studies and consistent physical parameterizations with the global climate model of the Max Planck Institute for Meteorology the ECMWF Hamburg model (ECHAM), the Europamodell parameterizations were replaced by the parameterization scheme of ECHAM4.5 (version 4.5 of ECHAM, Roeckner et al., 1996). Herewith, uncertainties due to different parameterizations between driving and regional model can be avoided.

The prognostic variables of REMO are the horizontal wind $\vec{u}$, surface pressure p_s, temperature T, specific humidity q_s and cloud liquid water q_w. The temporal discretization is done by a leap-frog scheme with semi-implicit correction. A time filtering following Asselin (1972) is applied that allows for much longer time steps of the leap-frog scheme than usual. The vertical discretization is achieved by hybrid σ-coordinates (Simmons and Burridge, 1981). This technique combines the benefits of terrain following coordinates (σ-system) at the ground and pressure coordinates in the free atmosphere (p-system). Figure 2.1 shows a schematic of the vertical discretization in hybrid coordinates. Dotted lines with full number subscripts on the respective hybrid σ-level denote the levels where the prognostic variables are defined (given as φ). Half levels are given as solid lines mark the edges of each grid box in the vertical. Here the vertical velocity ω is diagnosed.

In the horizontal plane, REMO uses a spherical Arakawa-C grid (Arakawa and Lamb, 1977) where all prognostic variables φ except for the horizontal wind $\vec{u}$ are defined at the center of each grid box (see Figure 2.2). The zonal and meridional wind components $\vec{u} = (u, v)$ are defined at the edges of the grid being perpendicular to the edge. The centers of the grid boxes themselves are located on a geodetic grid.

When the tropics are not the area of study, REMO is usually run on a rotated grid to have similar grid box sizes and an optimized time step. This is done by turning the poles of the grid in such a way that the equator is running across the center of the area of interest.

As REMO is only simulating parts of the Earth (e.g., Europe) it requires information for the prognostic variables at the lateral boundaries. REMO, therefore, is nested into a data set that describes the circulation outside the domain. This can either be information from a global climate model (e.g., ECHAM) or *perfect boundary conditions* from observations or (re-)analysis (e.g., ECMWF 40 year reanalysis (ERA-40)). In all cases the driving data is interpolated to the REMO grid in all three dimensions. The horizontal interpolation is done by using a 16-point
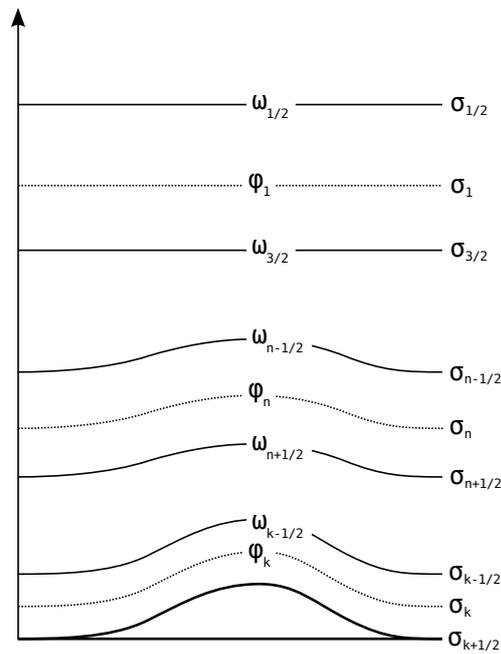
Figure 2.1: Schematic of the vertical discretization in hybrid coordinates (taken from Teichmann, 2009). Full levels are given as dotted lines and show where the prognostic variables (φ) are defined. The vertical velocity ω is diagnosed at half-levels.
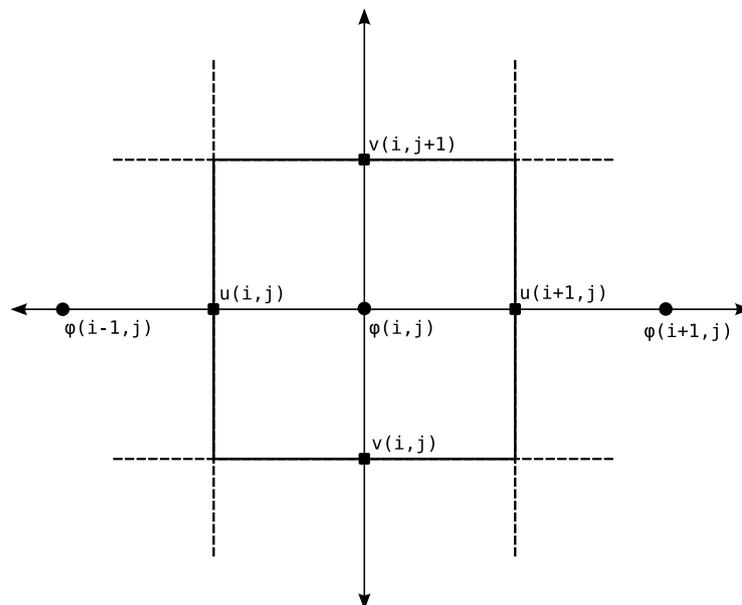

Figure 2.2: Schematic of the horizontal discretization on the Arakawa-C grid (taken from Teichmann, 2009). Circles depict the centers of each grid box (i, j) where the scalar prognostic variables φ are defined. On the edges the zonal (u) and meridional (v) wind components given as squares are defined.

formula for all atmospheric data, surface pressure and orography. Surface values are interpolated using a bilinear interpolation with respect to the land-sea mask. In the vertical column, one-dimensional tension splines (e.g., de Boor, 1978) are used for interpolation. Hydrostatic adjustments are performed during the interpolation to take into account height differences between the driving data and REMO grid.

The upper boundary condition is implemented as the *radiative upper boundary condition* by Bougeault (1983); Klemp and Durran (1983). This prevents the reflection of vertically propagating internal gravity waves that might occur when the usual assumption for coarse resolution hydrostatic models of a vanishing vertical velocity would be used. A relaxation scheme by Davies (1976) is used to adjust the model solution to the lateral boundary conditions. The model solution is gradually relaxed to the boundary conditions over the *sponge zone*, which is eight grid-boxes wide in REMO. The frequency with which the lateral boundary forcing is typically updated is 6 hours. A linear interpolation in time is done to provide lateral boundary informations for each time step. If REMO is not coupled to an ocean model, sea-surface temperatures are taken from the boundary forcing and similarly sea-ice concentrations when available.

To avoid sharp jumps in resolution, which can cause artificial wave reflections and breaking, it is possible to nest a high-resolution REMO domain into a low-resolution REMO domain. This technique is called double-nesting and is used to get high-resolution information which is required, e.g., in hydrological impact studies. Typical horizontal resolutions for REMO are between 0.5° and 0.088° (approx. 10 km at the model equator). Higher resolutions would violate the hydrostatic assumption and are therefore not used with the hydrostatic core.

REMO can be run in two different modes. The first one is the forecast mode in which the model is initialized with forcing data every 24 h in order to keep the model's solutions as close as possible to the forcing data. The second mode is the climate mode in which the model is initialized once at the beginning of the simulation and after that only updated at the lateral boundaries so that the regional model is able to create its own climate. In this study, as for most applications, the climate mode of REMO is used.

As mentioned above, the parameterization schemes of REMO5.0 are taken from the global climate model ECHAM4.5. The soil scheme consists of five layers for the heat budget with increasing thickness towards the bottom. The soil hydrology is parametrized using a bucket scheme, which takes into account vegetation effects

such as the interception of precipitation in the canopy. The effects of snow pack on the heat and water budgets are taken into account as well. The boundary layer parameterization scheme is based on the Monin-Obukhov similarity theory (Louis, 1979) with a turbulent kinetic energy closure after Brinkop and Roeckner (1995). Convection is parametrized using the Tiedtke (1989) mass-flux scheme with a closure based on convective available energy by Nordeng (1994). Stratiform clouds are computed from the mass mixing ratio of water vapor and cloud water. As microphysical processes the condensation of water vapor, evaporation of cloud water, the formation of precipitation and evaporation of precipitation are taken into account. The sub-grid scale formation of stratiform clouds is implemented using the formulation of Sundqvist (1978). The radiation parameterization is based on the developments of Fouquart and Bonnel (1980) and Morcrette et al. (1986). Modifications such as the consideration of additional greenhouse gases are implemented into this scheme (the reader is referred to Roeckner et al., 1996, for further details).

In addition to the parameterizations of ECHAM4.5, REMO5.0 includes several changes. One major difference is the handling of gravity waves. As it is assumed that orographic gravity waves are resolved by the typical resolutions of REMO, the parameterization of orographic gravity waves is switched off. One completely new development specific to the REMO parameterizations is the consideration of the yearly cycles in albedo, vegetation fraction and leaf area index (Rechid and Jacob, 2006). It has been proved that the consideration of these yearly cycles improves the yearly cycles of temperature and precipitation in the model when compared to observations. Other changes are resolution dependent modifications, such as changes in the threshold of relative humidity to form sub-grid scale clouds, for example.

2.1.1 New Developments since REMO5.0

As already mentioned above, several new developments have been incorporated into REMO since REMO5.0. One important change is the consideration of sub-grid scale variations of surface types (Semmler, 2002). The former approach only considered one surface type per grid box; either land, water or sea-ice. In the now implemented tile approach the surface is transformed to fractions of these three types. This allows for the calculation of surface fluxes for each fraction separately and for a more realistic representation of the climate, particularly in coastal regions. This scheme was extended by Kotlarski et al. (2010) to allow for the dynamic calculations of glaciers as a fourth surface type.

The work of Pfeifer (2006) incorporated cloud ice into the prognostic variables, to account for a more realistic representation of clouds. Furthermore, the convection scheme of REMO was extended to include an additional class allowing for cold convection. Cold convection appears, e.g., when cold air masses travel over warm water. In this case heavy precipitation events could occur that are not captured by models without cold convection parameterization. Rechid (2009) introduced a phenology scheme into REMO that dynamically models the growing season of vegetation. This allows for a more realistic representation of the growing season when using REMO in climate change studies, because it can be expected that the growing season changes in a changing climate. To investigate air quality in mega-cities Teichmann (2009) incorporated online-chemistry and transport processes based on a REMO5.0 branch with chemistry (Langmann, 2000) into REMO. A further important development is the inclusion of aerosols into a new branch REMO-HAM (Pietikäinen et al., 2012). This work extends REMO with the aerosol module of ECHAM5-HAM (Stier et al., 2005) and enables the study of aerosol effects in a regional modeling framework. To push REMO to even higher resolution Göttel (2009) developed a non-hydrostatic extension to the existing dynamical core. This enables fine scale simulations allowing for resolved convection in REMO.

All these developments add important processes to the model. These processes, however, should not change the fundamental behavior of the model and as such one can justify the use of REMO5.0 for the study of internal variability without the added complexity of the most recent versions. The results from REMO5.0 ought to be transferable to newer version or even other regional climate models. In the following section the experimental set up of REMO will be explained in detail.

2.2   Experimental set up

All research in this work has been done with the same ensemble of ten members using the regional climate model REMO5.0. In this section, the experimental set up used to investigate the internal variabilityof REMO over Europe is described. The internal variability is estimated from the inter-member variance of the REMO ensemble. Following earlier work by Alexandru et al. (2007) and Lucas-Picher et al. (2008b), the ensemble is initialized with a time lag of one day. As simulation period the ten years from 1979 to 1988 are taken, because it allows to compare the results to earlier studies such as Jacob et al. (2001). Alexandru et al. (2007) have shown that
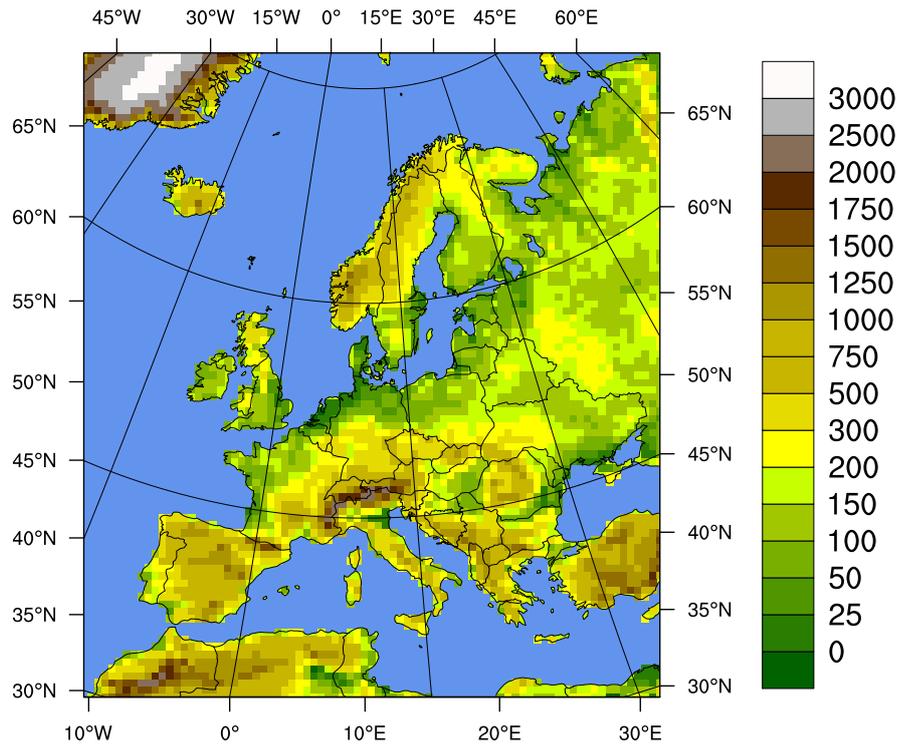
Figure 2.3: Domain of the REMO simulations with the orography in m.

an ensemble of ten members is the required number of members to get an robust estimate of internal variability in a regional climate model.

The target area of the simulations is Europe that is covered by a domain with 81x91 grid boxes (see Figure 2.3). The horizontal resolution is set to 0.5° ($\approx$ 55 km at domain center) which allows for a time step of 300 s. In the vertical 20 levels are used with the top level being at 10 hPa. The domain was chosen for computational efficiency and because it is one of the best tested domains of REMO.

As lateral boundary forcing and initial atmospheric conditions, ERA-40 reanalysis data (Uppala et al., 2005) is taken. The spectral resolution of ERA-40 is TL159 which corresponds to a resolution of 1.125° or approximately 125 km at the equator. The number of vertical levels in ERA-40 is 60 but for REMO only the 49 lowest levels were used for interpolation, as REMO does not extend as far as ERA-40 in the vertical. These perfect boundary conditions are used to investigate the models behavior under *observed* climate conditions. It therefore avoids difficulties in the interpretation of simulation results that might occur when using a global climate model that may introduce biases, e.g., in the flow patterns.

The update frequency for atmospheric fields and sea-surface temperatures was 6-
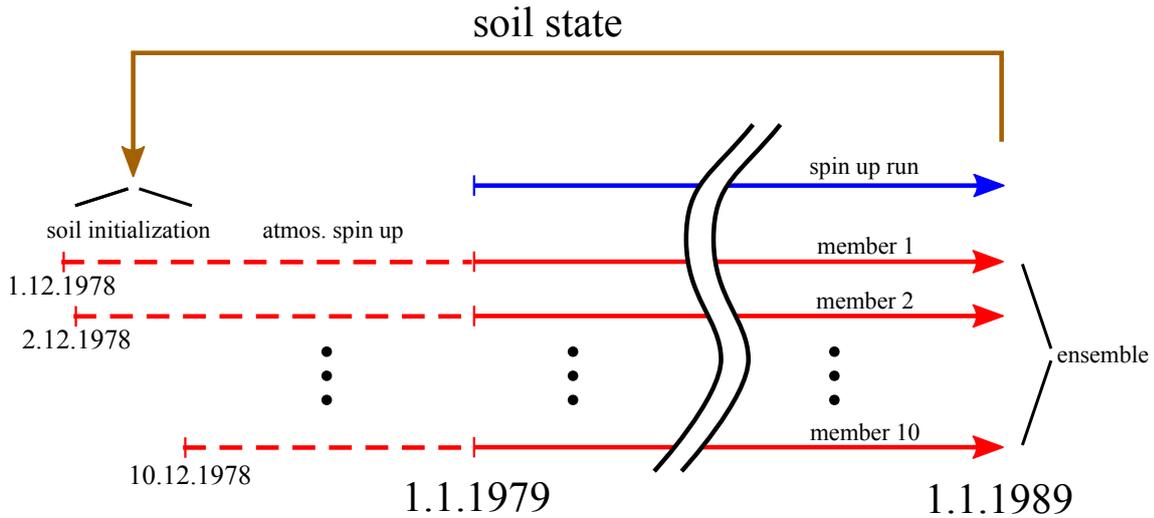
Figure 2.4: Schematic of the spin up and ensemble generation procedure. After running 10 years of spin up (blue arrow) the soil state is used to initialize the ensemble. The ensemble generation is achieved by choosing a lag of one day for the atmosphere initialization (red dashed lines). Only results from 1st of January 1979 0:00 are taken into account for analysis (red solid).

hourly. No large scale forcing such as spectral nudging was applied inside the domain and all simulations were run in climate mode. Hence, the model is free to develop its own mesoscale climate.

All simulations used for the analysis were initialized in warm start mode. This means that the initial values for soil moisture and temperature were taken from a simulation, where the deepest soil layer shows a yearly cycle but no trend in temperature. This is a standard procedure for REMO to avoid long term spin up effects from the soil scheme during the experiment. The spin up simulation was run with the same boundary data for the same time period from 1979 to 1988. The last state of the soil moisture and temperature from the 1st of January 1989 at 0:00 was used to initialize the ensemble runs starting in December 1978. The initialization of the ensemble started on the 1st of December 1978 with a one day lag between each member of the ensemble. Figure 2.4 shows a schematic of the spin up and ensemble generation procedure. It has been shown by Giorgi and Bi (2000) and Lucas-Picher et al. (2008b) that the perturbation method of the initial state does not matter for the level of internal variability after an atmospheric spin up of approximately 20 days. For the analysis, only results starting from the 1st of January 1979 0:00 were taken into account.

2.3   Analysis Method of Internal Variability

Similar to the experimental set up, the analysis method of internal variability is based on the approach of Alexandru et al. (2007) and Lucas-Picher et al. (2008b). To estimate the internal variability, the inter member variance s_φ^2 is used to characterize the spread of the ensemble. In this study, the unbiased variance estimator according to Lucas-Picher et al. (2008b) is taken, to avoid an artificial bias in the estimation of s_φ^2 which might occur due to the small ensemble size. The unbiased variance estimator is defined as

$$s_\varphi^2(i,j,k,t) = \frac{1}{M-1} \sum_{m=1}^{M} (\varphi(i,j,k,t,m) - \langle\varphi\rangle(i,j,k,t))^2 \tag{2.1}$$

where $\varphi(i,j,k,t,m)$ is the value of a parameter φ (e.g., temperature or precipitation) in the three dimensional grid (i,j,k) at output time t for ensemble member m. The variable M is the total number of ensemble members. The term $\langle\varphi\rangle(i,j,k,t)$ corresponds to the ensemble mean and is defined as

$$\langle\varphi\rangle(i,j,k,t) = \frac{1}{M} \sum_{m=1}^{M} \varphi(i,j,k,t,m). \tag{2.2}$$

As s_φ^2 gives the inter member variance for each grid cell at each output time step t (6-hourly in this study), it is useful to reduce the dimensions by spatial and temporal averages in order to gain a more comprehensive overview. For the time evolution of internal variability s_φ^2 is averaged over the horizontal domain by

$$\{s_\varphi^2\}(k,t) = \frac{1}{I \cdot J} \sum_{i=1}^{I} \sum_{j=1}^{J} s_\varphi^2(i,j,k,t) \tag{2.3}$$

with I and J being the number of grid boxes in the x- and y-direction or zonal and meridional direction, respectively. Although the grid rotation is optimized for similar sized grid boxes, it is stretched identical to a regular longitude/latitude grids, thus area weights are applied. For all spatial means the sponge zone of eight grid boxes is omitted on each horizontal edge of the domain. As the sea-surface temperature is identical in each simulation, spatial averages are computed with and without water

points, by applying the land-sea mask of REMO prior to the spatial averaging. To investigate the climatology of the spatial distribution, the time average $\overline{s_\varphi^2}$ for each grid point is computed by

$$\overline{s_\varphi^2}(i,j,k) = \frac{1}{N}\sum_{t=1}^{N} s_\varphi^2(i,j,k,t) \tag{2.4}$$

with N being the number of time steps.

The equations above are used to compute the variance on a output step basis. It is also important to know the variance on longer time scales. Therefore, time averages over several output steps are computed to get, e.g., monthly means. The variance of the time averages between the different ensemble members is computed by

$$s_{\overline{\varphi}}^2(i,j,k) = \frac{1}{M-1}\sum_{m=1}^{M} \left(\overline{\varphi}(i,j,k,m) - \langle\overline{\varphi}\rangle\,(i,j,k)\right)^2 \tag{2.5}$$

where $\overline{\varphi}(i,j,k,m)$ is the temporal average for every ensemble member m at every grid point (i,j,k) and $\langle\overline{\varphi}\rangle\,(i,j,k)$ the time averaged ensemble mean. It is important to note the difference between equation (2.4) and (2.5). With equation (2.4) the climatology of the variance based on the output time step is computed, whereas (2.5) yields the variance of time averages longer than the output time step.

The equations above are used for all internal variability estimations in the following Chapters 3, 4 and 5. Analysis methods specific to each chapter, e.g., the circulation type analysis used in Chapter 4, are discussed in detail in the corresponding chapters.

Chapter 3

Characteristics of Internal Variability over Europe

As introduction into the main parts of this work, the general characteristics of internal variability over Europe are discussed first. Generally one presents a comparison of model performance to observations. However, several studies evaluating the performance of REMO5.0 on the present domain have been conducted. The most important biases are a overestimation of precipitation in the Baltic Sea catchment (Jacob et al., 2001) and the summer drying (Hagemann et al., 2004) in south eastern Europe. For additional information, the reader is referred to the literature (e.g., Jacob et al., 2001; Hagemann et al., 2004; Jacob et al., 2005; Rechid and Jacob, 2006). Furthermore, the performance of the model plays not such an important role for the sensitivity of the model to perturbed initial conditions. The main question that is tackled in this chapter is: *How does internal variability change with season over Europe?* The chapter is structured as follows: First, the temporal evolution for different parameters is investigated in Section 3.1. This is followed by an analysis of the spatial patterns in Section 3.2. Finally, in Section 3.3 the behavior of internal variability on different climatic time scales is discussed. Some concluding remarks are given in Section 3.4.

3.1   Temporal Evolution

The temporal evolution of spatial mean internal variability ($\{s_\varphi^2\}$) is investigated for mean-sea-level pressure, near-surface temperature, and precipitation. To retain the

dimensions of each variable and ease the interpretation the square root of the inter member variance for every variable is taken at the end of each calculation. Figure 3.1 depicts the temporal evolution of internal variability over the entire simulation period for mean-sea-level pressure, near-surface temperature, and precipitation. Blue lines show the results for the entire domain, whereas green lines depict land-points only.

The internal variability of the mean-sea-level pressure (Figure 3.1 (a)) shows occasionally strong oscillations around a mean value of 1 hPa. Most maximum values of around 2.5 hPa, and in one case over 4 hPa, appear in winter or spring. Autumn shows relatively low internal variability in most years. This results in a mean annual cycle of the internal variability with highest values in spring and lowest in autumn (see Figure 3.2 (a)). The internal variability in autumn, generally speaking, is half as large as internal variability in spring. The differences between all and land-only spatial mean internal variability is not big. This can be related to the fact that pressure is a quite smooth and large-scale influenced quantity and does not depend strongly on land-sea contrasts.

The internal variability of the near-surface temperature (Figure 3.1 (b)) shows similar results in terms of local maximums and minimums to that of the mean-sea-level pressure. Both are well correlated (correlation coefficient 0.92), but there are important differences. The first difference is the season with maximum values. For temperature the largest internal variability appears in winter and then gradually reduces until autumn (see also Figure 3.2 (b)). The second difference is that internal variability becomes larger compared to internal variability of mean-sea-level pressure if only land-points are taken into account. There are two reasons for this. The first reason are the prescribed sea-surface temperatures. The near-surface temperature in the model is strongly bound to the sea-surface temperature over water. Hence, it cannot show high internal variability. The second reason is the soil scheme which calculates soil and surface temperatures dynamically. Every modeled soil process, and their interactions, can influence the near-surface temperature. Since there are many more degrees of freedom in the diagnostics of the near-surface temperature, the internal variability is expected to be much higher over land. One extreme example would be, if there was snow in a specific grid box for one member while the other member showed snow-free conditions. In this case, near-surface air temperatures can be very different during, e.g., cloud-free nights, thus leading to larger internal variability.
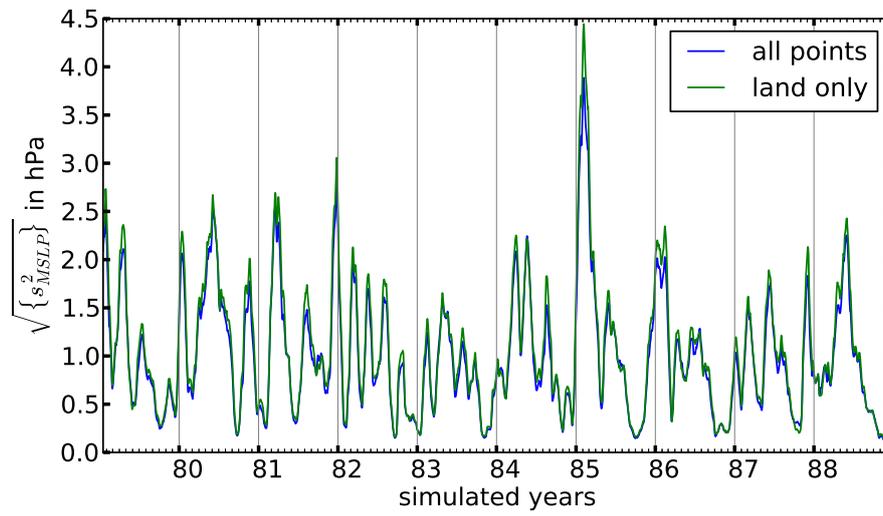
(a) mean-sea-level pressure
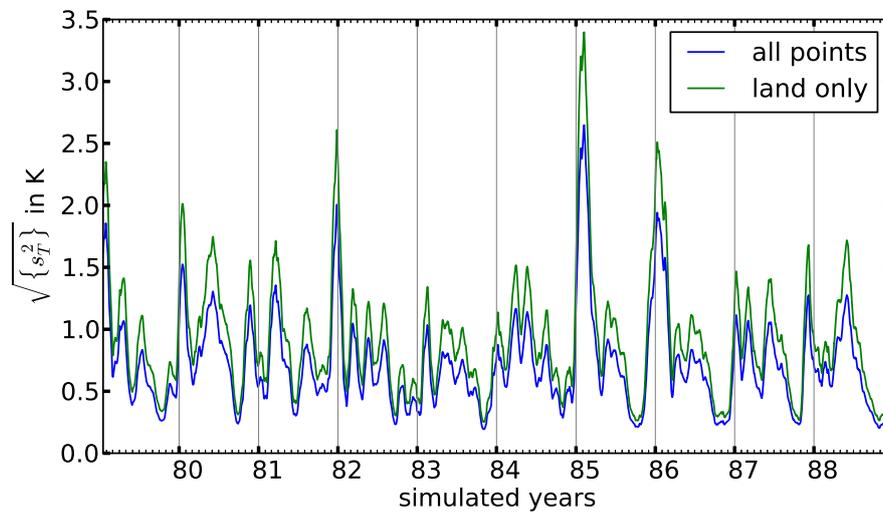
**(b)** near-surface temperature
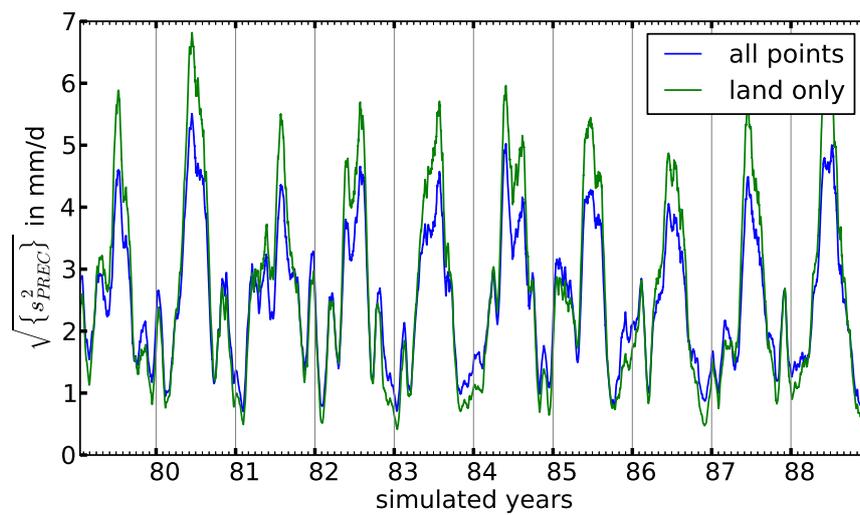
(c) Precipitation

Figure 3.1: Square root of area averaged internal variability of (a) mean-sea-level pressure, (b) near-surface temperature, and (c) precipitation over the entire domain (blue line) for the entire simulation period. The green line is the same but only for land-points. A 30 day moving average has been applied to each line.
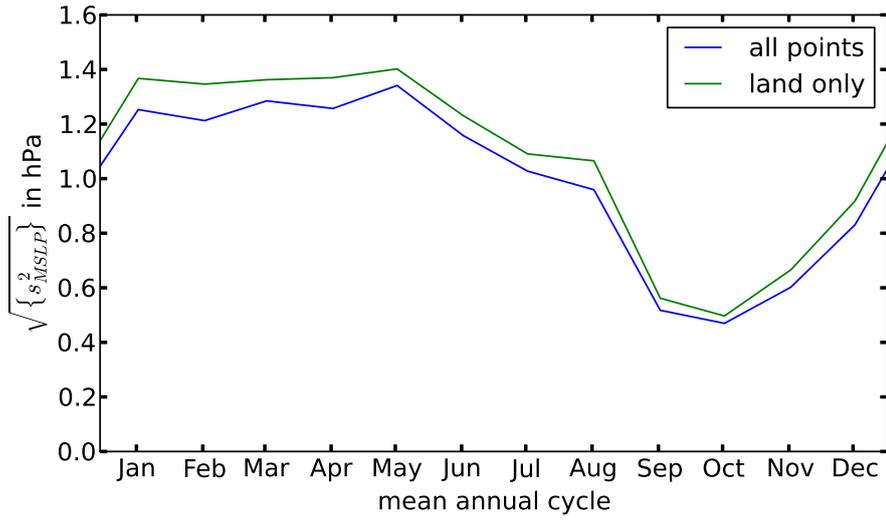
(a) mean-sea-level pressure
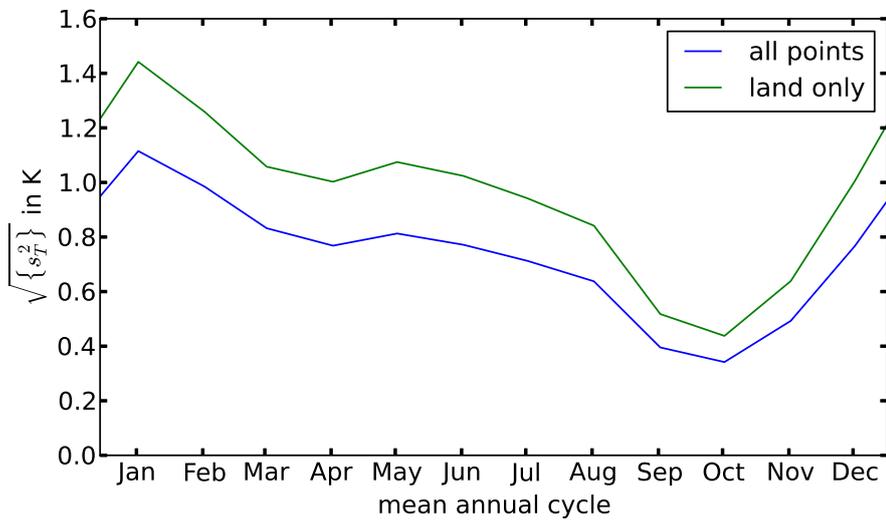
(b) near-surface temperature
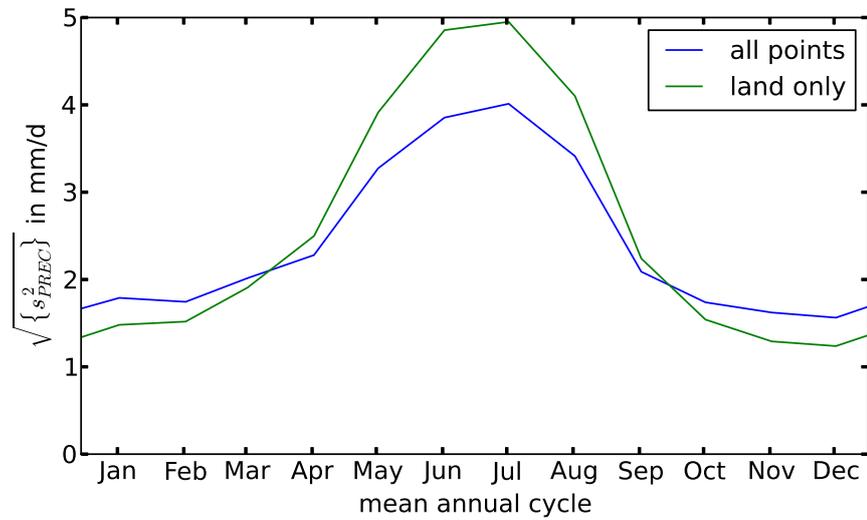
(c) Precipitation

Figure 3.2: Mean annual cycle of internal variability from multi year monthly mean internal variability.

The internal variability of precipitation behaves quite differently compared to the two previous quantities described (see Figure 3.1 (c)). Here, the mean annual cycle (Figure 3.2 (c)) shows a clear maximum in summer and a minimum in winter. This is linked to the much stronger convective activity in summer, which leads to a more heterogeneous precipitation field due to the non-linear nature of the processes involved. Noteworthy is the stronger annual cycle in internal variability of precipitation over land. During winter the internal variability over land is generally smaller compared to the total internal variability. This is again related to convective activity. In winter, most of the convective precipitation falls over open water because of warm sea-surface temperatures, thus leading to higher internal variability over the oceans. During periods of high internal variability in mean-sea-level pressure the internal variability of precipitation is also enhanced (e.g., summer of 1980) indicating that there is a correlation between the internal variability of these two parameters, too.

The annual cycles of mean-sea-level pressure and temperature internal variability (Figure 3.2 (a) and Figure 3.2 (b)) are different to the results found by Caya and Biner (2004) for North-America and Giorgi and Bi (2000) for Eastern China. In both studies the summer internal variability is generally much higher compared to the winter internal variability. They argue that local processes are more important and forcing from the boundaries is reduced in summer compared to winter. Thus concluded that the regional climate model is therefore better able to develop its own climate and variability. Their studies, however, are limited by the length of the simulations. Both studies investigate only one year or single seasons, respectively. If one would have considered only one year, e.g., year 84 in the present study, a similar conclusion could have been drawn. Hence, it might have been by chance that they missed periods of high internal variability in winter. Another reason for the low internal variability in winter might be the target area. Both studies investigate internal variability on northern-hemisphere mid-latitude domains. As the northern-hemisphere mid-latitudes are rather heterogeneous, it is very likely that the location of the domain will play a role in the development of internal variability.

Lucas-Picher et al. (2008b) mention that the location of the domain might play a role, but they argue that the differences of their annual cycle, for example in mean-sea-level pressure internal variability with high values in spring and low values in fall, compared to Giorgi and Bi (2000) and Caya and Biner (2004) with only high internal variability in summer are mainly a result of domain size. As the domain size of the present study is comparable to the one from Giorgi and Bi (2000), another

reason for the differing results in annual cycles is presented.

Laprise et al. (2012) pointed out that the internal variability in a regional climate model is connected to the prevailing weather regime. As the forcing from the boundaries (especially in small domains) is quite strong, only episodes with weak forcing can lead to higher internal variability. One weather regime having the potential for reducing the boundary forcing are persistent high-pressure episodes, e.g., blocking episodes. The phenomenon of a blocking is generally characterized by a meandering jet stream. As the jet is a strong forcing in West-East direction in mid-latitude domains due to the high wind speeds, a meandering would result in a weaker forcing. Hence, the regional climate model has a greater ability to create its own climate, which implies that small differences between two members of the regional climate model ensemble can grow. Thus, leading to higher internal variability.

The northern-hemisphere blocking frequencies as a function of longitude (D'Andrea et al., 1998) are shown in Figure 3.3 (a). It can be seen that Eastern-China (90°E – 120°E) and Eastern-North-America (120°W – 60°W) are regions with a minimum in blocking frequency almost all year long. Europe (15°W – 45°E) in turn has a maximum in blocking frequency with a minimum in autumn. This could explain why the annual cycle of internal variability in the present study is more similar to the annual cycle of internal variability in the study by Lucas-Picher et al. (2008b) who investigate entire North-America including parts of the secondary maximum in blocking frequency east of 180°W.

In addition to the differences in annual cycles of internal variability between different regions in the mid-latitudes, the blocking frequencies can also explain the seasonal variations in internal variability. From the mean annual cycle of internal variability it can be seen that internal variability is reduced in autumn compared to other seasons. As an example Figure 3.3 (b) shows the mean annual cycle of the 500 hPa-geopotential height. This cycle correlates quite nicely with the Hovmöller diagram in blocking frequency over Europe (Figure 3.3 (a) around 0° longitude). Showing that months with high (low) internal variability generally show a high (low) frequency of blockings.

The importance of weather regimes in terms of circulation types for internal variability in REMO over Europe is picked up again in Chapters 4 and 5. In the following section the focus is on the spatial distribution of internal variability.
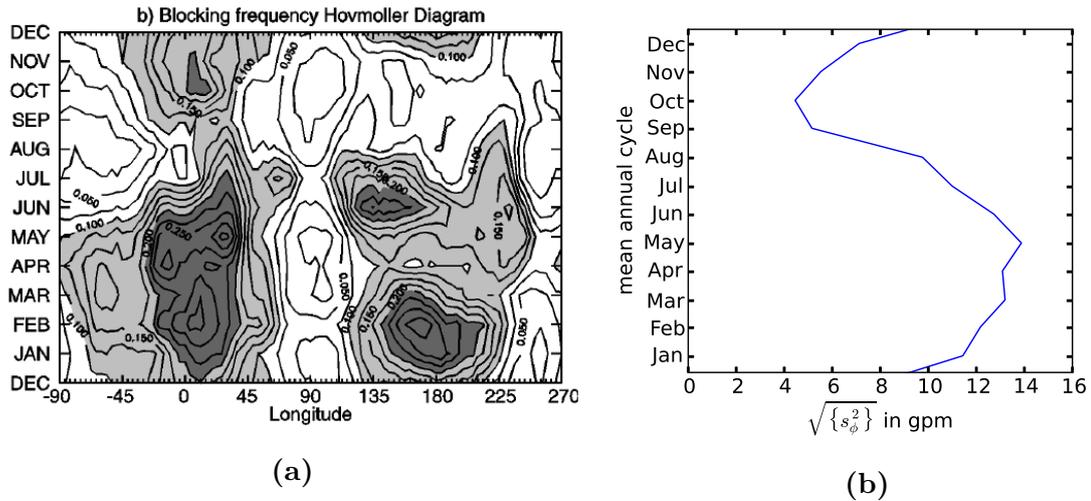
Figure 3.3: Comparison between (a) blocking frequency in a Hovmöller diagram (longitudinal-seasonal) from observations between 1949-1994 (taken from D'Andrea et al. (1998) Figure 2b) and (b) the mean annual cycle internal variability (from multi year monthly means) of the $500\,\mathrm{hPa}$-geopotential height.

3.2 Spatial Patterns

In this section, spatial patterns of seasonal mean internal variability according to equation (2.4) are analyzed. It is important to analyze the spatial distribution of internal variability in order to identify regions with a high sensitivity to the initial conditions of a simulation. These are also regions were the influence from the lateral boundary forcing is weak and local effects such as land-atmosphere coupling play an important role.

First, the spatial patterns of mean-sea-level pressure is discussed. Figure 3.4 shows the spatial patterns of mean seasonal mean-sea-level pressure internal variability. For all seasons the highest values of internal variability are found in the North-East sector of the domain. The location of the maximum is slightly altered with respect to the season but the biggest differences can be found in the strength of internal variability. As already seen in the seasonal spatial means the highest values are found in spring with a maximum of more than $2.4\,\mathrm{hPa}$. The maximum values for winter and summer are pretty similar with $2.2\,\mathrm{hPa}$ and $2\,\mathrm{hPa}$, respectively. For autumn the maximum only reaches $1\,\mathrm{hPa}$.
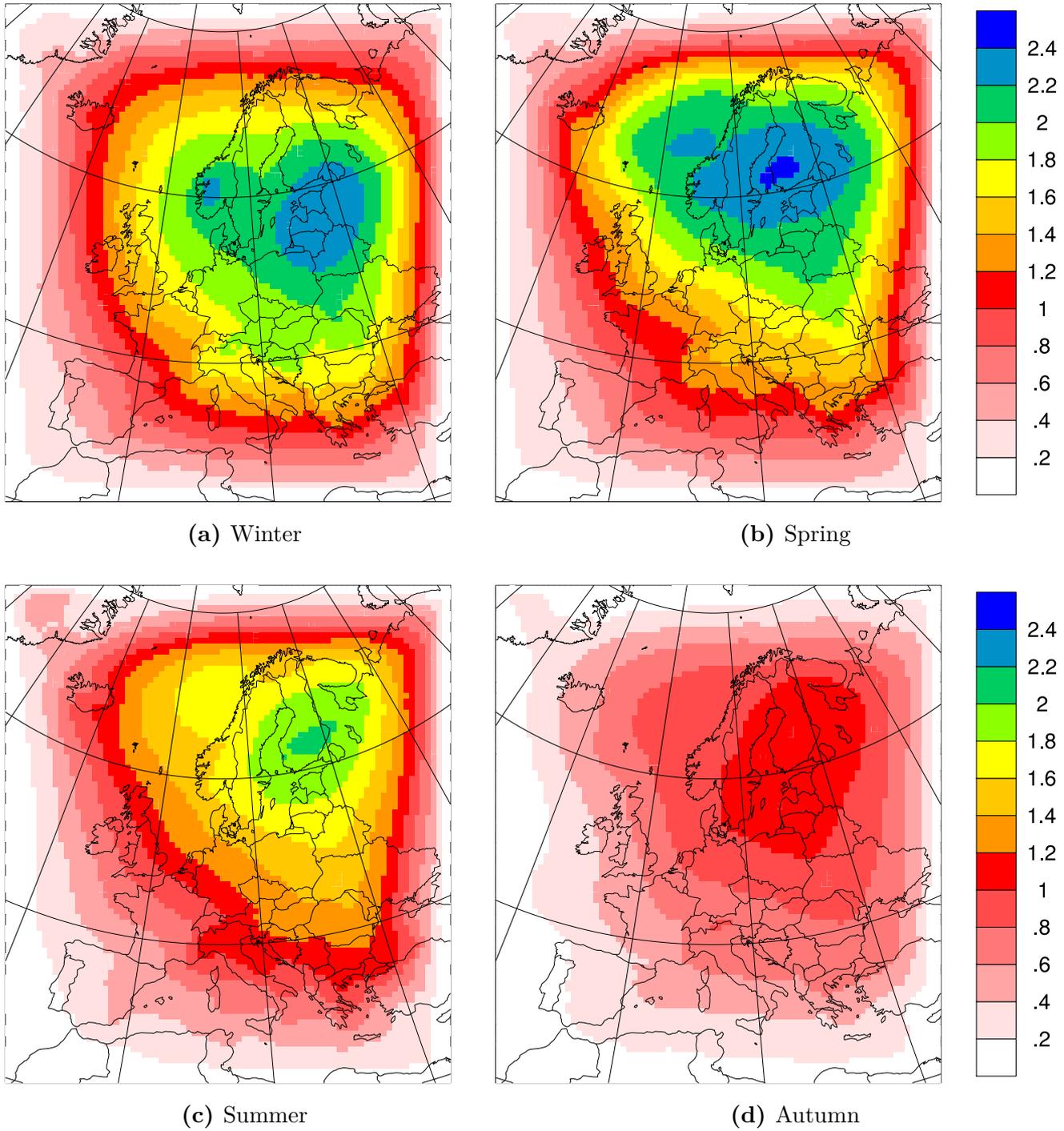
Figure 3.4: Spatial patterns of seasonal mean mean-sea-level pressure internal variability in hPa.

In general, the patterns look rather smooth with only a few local effects such as the local maximums over the Norwegian mountains or the alps. One reason might be that mean-sea-level pressure is strongly forced by the driving data. This is due to the direct connection between mean-sea-level pressure and surface pressure, which is a driving field at the boundaries. In addition, the pressure values in the grid are horizontally connected due to horizontal advection and numerical diffusion. Thus the pattern looks much more homogeneous.

The spatial patterns of mean-sea-level pressure internal variability do not show large differences to previous studies. It is known from other studies that the highest values of internal variability are expected to be close to the eastern boundary of a northern-hemisphere mid-latitude domain. Lucas-Picher et al. (2008a) demonstrated that the residency time of air parcels within the domain is usually the longest towards the eastern boundary due to the predominant westerly flow in the mid-latitudes and correlates linearly with the spatial pattern of internal variability. Thus the deviations of air parcel trajectories between ensemble members grows with the time the air parcel stays inside the domain. Depending on the flow regime for each season, this alters the location of the internal variability maximum a little but places it towards the eastern boundary due to predominant westerly flow.

Although near-surface temperature and mean-sea-level pressure are highly correlated in their spatial mean temporal evolution of internal variability, the seasonal mean spatial patterns look quite different. Figure 3.5 shows the spatial pattern of seasonal mean internal variability of near-surface temperature for the four seasons. The area with the largest internal variability is in the north-eastern sector around the Baltic Sea and has much more heterogeneity compared to the spatial pattern of mean-sea-level pressure internal variability. One noteworthy feature is the zone of higher internal variability in the North-Atlantic, near Greenland. This local maximum of internal variability shows the area of the sea-ice edge, which is typically characterized by large differences in surface fluxes. It is a good example for how local scale, non-linear processes can trigger internal variability in near-surface temperatures.

(a) Winter

(b) Spring

(c) Summer

(d) Autumn
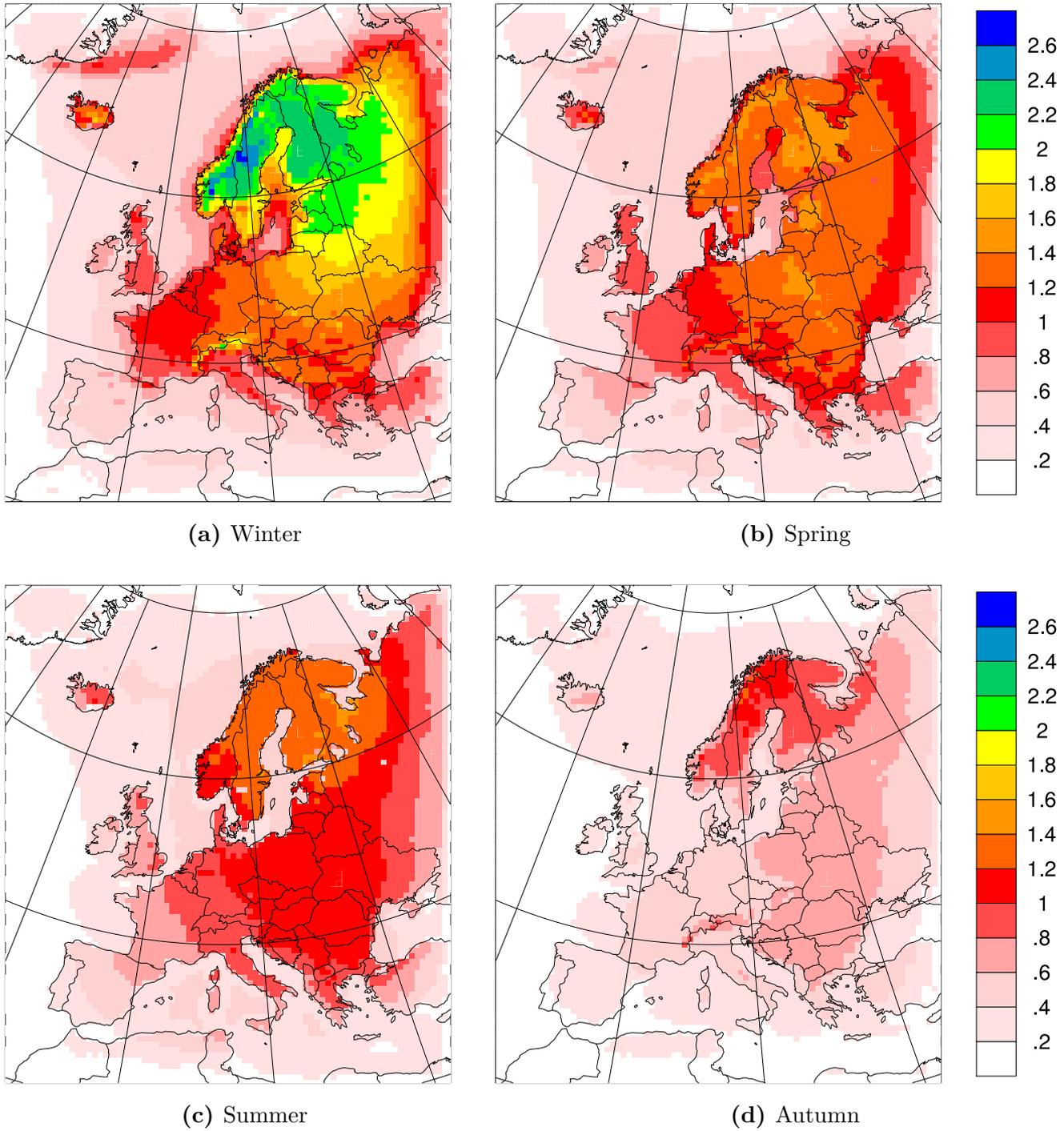
Figure 3.5: Spatial patterns of seasonal mean near-surface temperature internal variability in K.

Comparing the seasons it becomes evident that the variations in terms of maximum internal variability values across the seasons are higher compared to mean-sea-level pressure internal variability. In winter the maximum internal variability reaches more than 2.6 K along the Norwegian Mountains and central Sweden (Figure 3.5 (a)). In Spring (Figure 3.5 (b)) internal variability is reduced up to 1.8 K. The pattern of internal variability is more homogeneous and shows no clear maximum. Similarly homogeneous patterns, with weaker gradients of internal variability, can also be seen for summer and autumn. In summer the maximum of 1.6 K and is located between Baltic and White Sea (Figure 3.5 (c)). In autumn the weakest maximum of only up to 1.2 K is present in northern Scandinavia (Figure 3.5 (d)).

The stronger difference in the spatial patterns of internal variability of mean-sea-level pressure and near-surface temperature show that internal variability is more correlated in time than in space. One reason for the stronger difference in the spatial pattern is that near-surface temperature in one grid box is in principle independent from the neighboring boxes. The independence originates from the soil parameterization that does not take horizontal communication between the grid boxes into account. Horizontal communication arises from the atmosphere, but the influence on near-surface temperature is usually strongest from the surface. Thus, near-surface temperature is largely influenced by local heterogeneities.

One supporting observation for the hypothesis that snow-covered areas have the potential of generating high near-surface temperature internal variability (see Chapter 3.1) is the behavior of near-surface temperature internal variability over the Alpine ridge. Especially in winter but also in the transition seasons, spring and autumn, the ridge sticks out with a local maximum in internal variability. No recognizable effect can be seen in summer. Neglecting the stronger forcing close to the boundaries, one can see that the snow-pack pattern correlates quite well with the internal variability pattern of near-surface temperature especially in winter (not shown).

(a) Winter

(b) Spring

(c) Summer

(d) Autumn
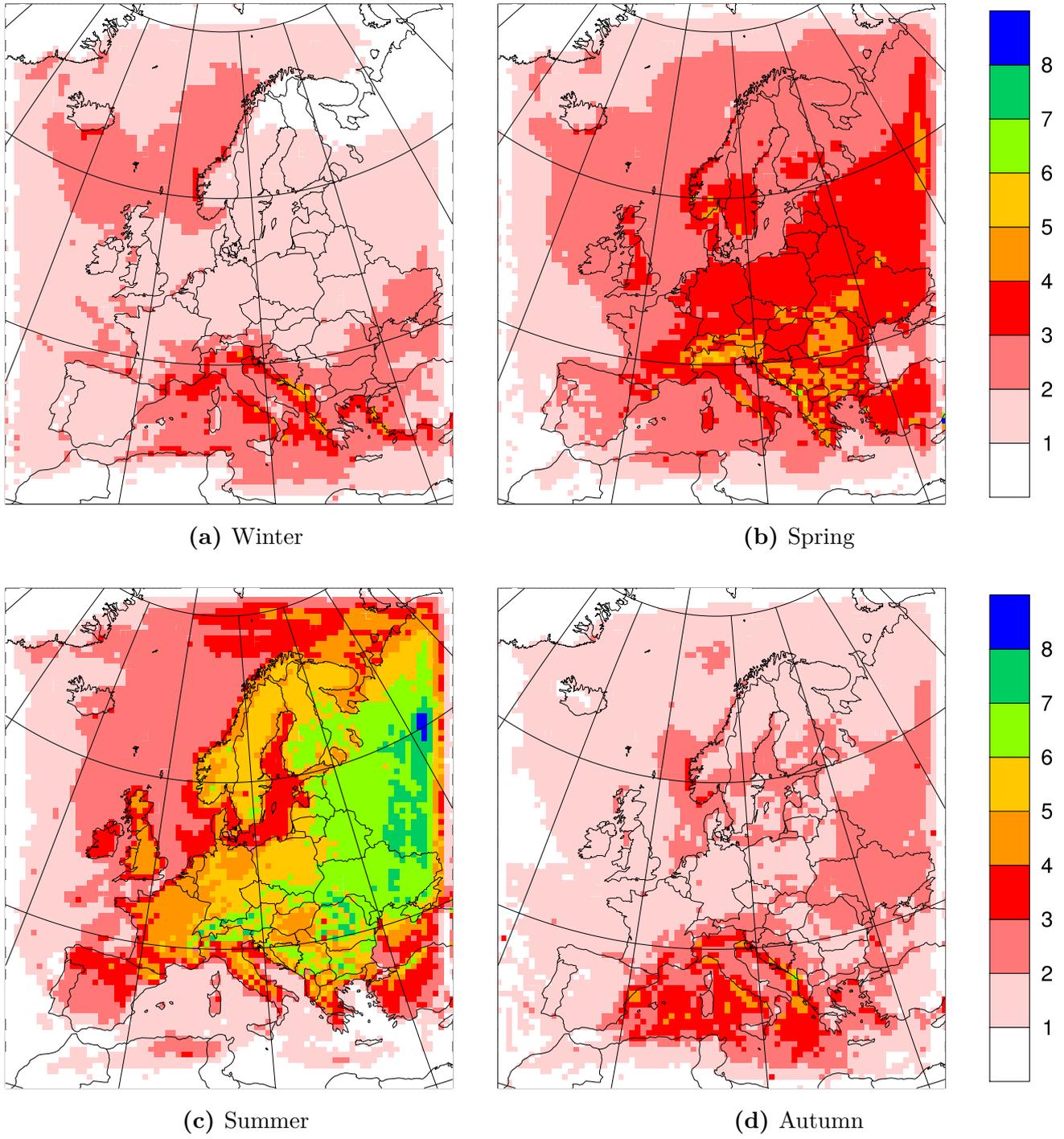
Figure 3.6: Spatial pattern of seasonal mean precipitation internal variability in mm/d.

For precipitation the picture changes. As already seen in the temporal evolution of precipitation internal variability, in winter the larger variability can be found over water (Figure 3.6 (a)). The highest values of more than 5 mm/day appear along the coasts of the Mediterranean Sea[1]. These are also the areas where a similar amount of precipitation is coming from the large and sub-grid scale precipitation schemes. In regions where the large-scale precipitation dominates the total precipitation sum internal variability tends to be lower (not shown), because the sub-grid scale precipitation schemes are expected to be more sensitive to local effects and large scale flow perturbations. Where the contribution of sub-grid scale precipitation is high, the internal variability can be stronger.

In spring the internal variability of precipitation amount is already higher over land, although the highest values with about 6 mm/day can still be found at the Adriatic Sea (Figure 3.6 (b)). The summer shows a much higher internal variability especially over land (Figure 3.6 (c)) with values of around 8 mm/day close to the outflow boundary. Besides the land-sea contrast, a gradient from west to east with increasing internal variability is visible. This gradient can be explained by the increasing importance of local processes for precipitation in a more continental climate regime.

Over land the sub-grid scale precipitation dominates in the total precipitation sum in most of the regions. Here the same argument as for winter holds that in sub-grid precipitation dominated areas the internal variability is stronger. In autumn (Figure 3.6 (d)) again the Mediterranean Sea is the area with the highest precipitation internal variability. In general in can be stated that precipitation internal variability shows a highly heterogeneous pattern and seems to be mostly driven by local effects such as land-sea contrasts or mountain ranges.

The sharp drop of precipitation internal variability at the eastern boundary that becomes especially evident in summer, is a result of the boundary relaxation that suppresses internal variability close to the domain edges. Here, the prognostic variables are forced to the same value for each member. Thus the parameterized processes and variables will also be similar. In REMO though results can still differ, because some prognostic variables such as temperature are only relaxed towards the lateral boundaries under inflow conditions.

Cretat and Pohl (2012) have shown that different convection schemes yield different

---

[1]The reader ought to bear in mind that coast lines are coarser in the model compared to the displayed map. The map serves to help orientate the reader, which is usually sufficient but may cause some confusion in this particular case.

strengths of internal variability in precipitation. Nevertheless, spatial patterns and temporal evolution show quite some correlation. Thus, it can be expected that the strength of internal variability in precipitation would change for REMO, if different a parameterization than the mass-flux scheme by Tiedtke (1989) was employed. The spatial patterns, however, would be expected to be of similar shape.

3.3   Internal Variability of Temporal Averages

In the previous sections, the temporal evolution and spatial patterns of the climate of internal variability on a six hourly basis was discussed. This section focuses on the effects of internal variability on longer time scales using different climate time scales. It allows to estimate on which time scales internal variability is important. It is referred to as internal variability of the climate, to prevent confusions with the previous sections. Here, climate is used in the sense of a temporal average that is longer than the output time step. For the analysis, several temporal averages within the ten years of simulation are computed for each ensemble member separately. Followed by estimating the internal variability of the climate by calculating the variance $s_{\overline{\varphi}}^2$ between the ensemble members at every grid point using Equation (2.5).

First, the spatial patterns of two different averaging periods are analyzed. Figure 3.7 shows the spatial patterns of near-surface temperature internal variability of the climate for averaging periods of 10 and 100 days. For both averaging periods the mean internal variability of the climate is small compared to the output time step based internal variability. This means that on average internal variability of the climate for this domain does not play a big role. Still two centers of action can be identified from Figure 3.7. These are the Baltic Sea region as expected from the previous results and south eastern Europe. One noteworthy feature in the case of south eastern Europe is that local maximums of internal variability of the climate are in regions surrounded by mountain ranges. Here the flow seems to be less constrained by the large scale circulation. A similar local maximum can be seen in the Po valley, too.

The mean internal variability of the climate, however, does not show the real sensitivity of different regions to internal variability of the climate, because of a rather noisy temporal evolution of internal variability. As such, the two regions identified as centers of action are analyzed in more detail. Two boxes located over central Sweden and East Hungary (black boxes in Figure 3.7), with the size of 4×4 grid
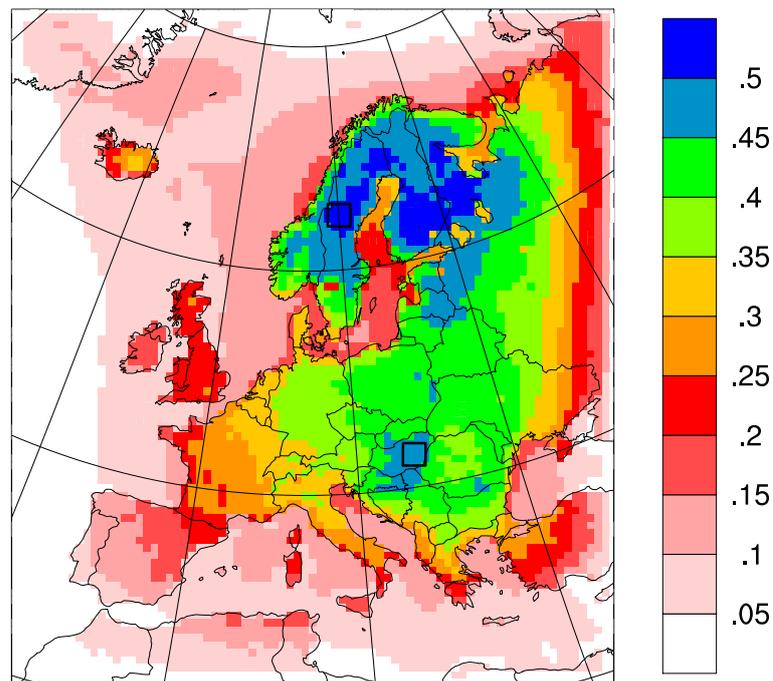
(a) 10 days average
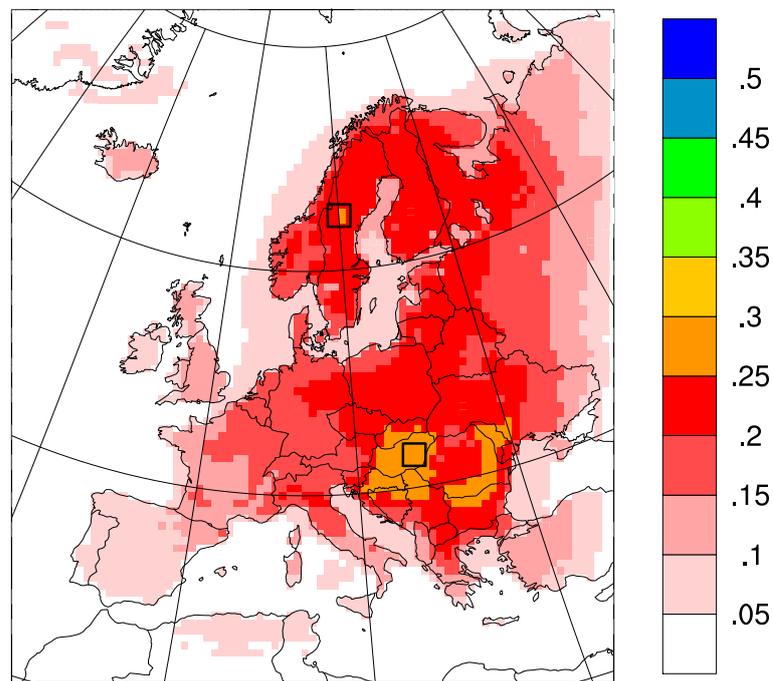
(b) 100 days average

Figure 3.7: Spatial patterns of near-surface temperature internal variability of the climate mean in K for averaging periods of (a) 10 days and (b) 100 days. The two areas marked with the black boxes are used for the charts in Figure 3.8.
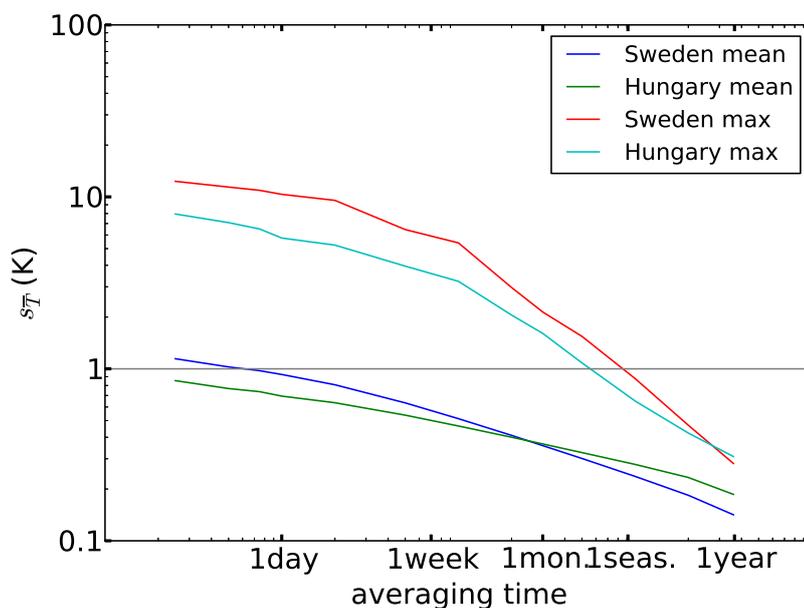
Figure 3.8: Internal variability of the climate for near-surface temperature over different averaging periods and two different areas. Blue and dark green showing the mean internal variability of the climate for Sweden and South-Eastern Europe. Red and light green showing the maximum of internal variability of the climate for Sweden and South-Eastern Europe. Note that both axis have a logarithmic scale.
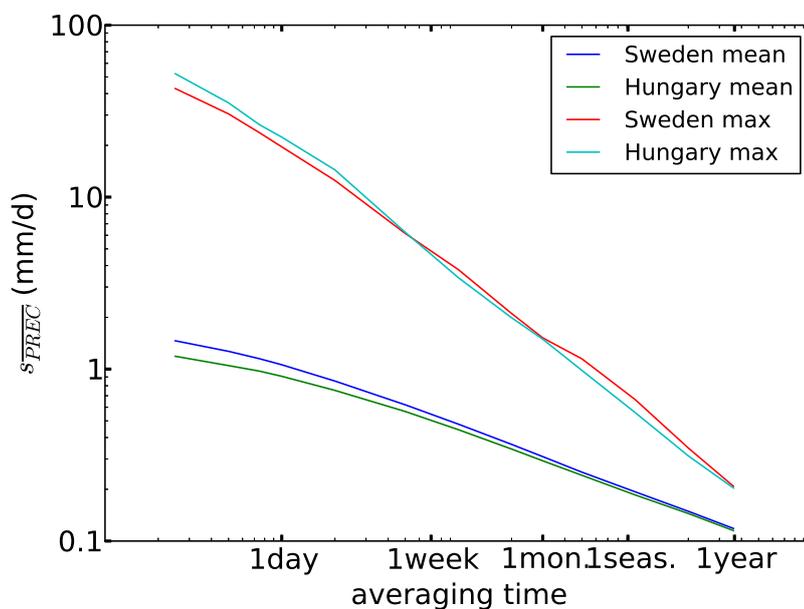
Figure 3.9: Same as Figure 3.8 but for precipitation.

boxes in each region, are picked to compute internal variability of the climate for several averaging periods. Figure 3.8 shows the box field means of near-surface temperature internal variability of the climate for the two regions. To get an estimate for the possible extreme cases the maximums of internal variability of the climate are shown as well. It can be seen that the mean internal variability of the climate for Sweden is higher for short time scales, but also decreases faster towards longer averaging periods compared to internal variability of the climate in Hungary. This was already expected from Figure 3.7, where in the 10 days average the central Sweden box shows stronger internal variability compared to Hungary. In the 100 days average case the stronger internal variability can be found over Hungary. In the maximum case, however, the behavior is a little bit different. Up to roughly a week internal variability of the climate can be large with values above 6 K in central Sweden. It is noteworthy that internal variability of the climate can still be in the order of 1 K in extreme cases after averaging over one season. In Hungary the maximum internal variability of the climate is generally lower, but does not drop so fast. This can be interpreted as a longer memory in internal variability of the climate for this region. Or in other words: The differences in near-surface temperature between members of a time-lagged ensemble average out faster in Sweden than in Hungary.

Figure 3.9 shows the internal variability of the climate of precipitation over different time averages for the two regions. There are hardly any differences in the evolution of internal variability of the climate between both regions. At first glance this is surprising because the precipitation regimes are quite different. The ratio between sub-grid and large scale precipitation would suggest a higher variability for Hungary. Here the ratio of precipitation from the sub-grid scale is usually higher. But the fact that total precipitation amounts are larger in Sweden might compensate for this effect, because a larger overall variability can be expected.

3.4   Conclusions

It has been shown that internal variability of a regional climate model in Europe is similar to other regions in the northern hemisphere mid-latitudes. Specifically the episodic character of internal variability with strong and weak phases, most probably connected to the prevailing weather regime, are similar. But there are also important differences. In Europe the peak internal variability for mean-sea-level pressure and near-surface temperature are found in spring and winter, respectively. The internal

variability of precipitation in turn shows more the behavior expected from earlier studies with weak internal variability in winter and strong internal variability in summer. This rather mixed picture in annual cycle leads to the conclusion that internal variability for different variables is differently influenced by the large scale forcing (or weather regime). The fact that the annual cycle of internal variability for mean-sea-level pressure and near-surface temperature looks similar to the annual cycle of the blocking frequency can explain the difference to the other mid-latitude locations. In the following chapter the influence of circulation types on the internal variability of different variables will be picked up. In terms of internal variability on longer time scales the effects do not seem to be much important after one season. This is most likely to change if bigger domains and more grid points are used, as already shown by Lucas-Picher et al. (2008b) for a domain over North-America.

Chapter 4

Influence of Circulation Types on Internal Variability

As seen in the previous chapter internal variability of a regional climate model undergoes alternating cycles of high and low variability. Internal variability is especially strong in winter which has not been reported for such a small domain. A key to understanding this variability is the boundary forcing. It has been shown that the blocking frequency in the Euro-Atlantic sector is coherent with the internal variability of the 500 hPa-geopotential height. In this chapter, the investigation is taken further by performing a circulation type classification on the boundary data. The main question is: *How do weather regimes influence the internal variability of a regional climate model throughout different seasons?* In Section 4.1 the concept of circulation type classifications is introduced and the Simulated Annealing and Diversified Randomization clustering (SANDRA) circulation type classification, used in the present study, is explained. Results from the circulation type classification are presented in Section 4.2 and concluding remarks follow in Section 4.3.

4.1   Circulation Type Classification

The principle idea behind a circulation type classification is to assign weather situations to clusters of circulation (or weather) types, or in other words, to group similar weather maps into representative classes. Circulation type classifications exhibit a long history in meteorology and climatology. They have proven to be a useful tool for understanding and interpreting atmospheric processes as well as linking atmos-

pheric processes and surface climate (see Huth et al., 2008, for a comprehensive review). Many different methods of classifying weather situations into circulation types exist. The coarsest distinction is the division into subjective, hybrid and objective methods. First, in the beginning of circulation type classifications subjective methods were mainly used for classification, e.g., daily weather charts were grouped into synoptic situations as done in the *Großwetterlagen* classification by the DWD (Hess and Brezowsky, 1952). In this case, the definition of the types and the assignment to them is normally done by expert knowledge. Meteorologists decided which circulation type the weather chart of a particular day belongs and hence was subjective.

Hybrid or mixed classification methods evolved out of pure subjective methods. Taking again the example of the Großwetterlagen, James (2007) developed an algorithm processable by a computer which assigned the weather charts to the classification types. With increasing computer power objective methods became more and more popular. The main difference to subjective methods is that usually no prior definition of circulation types is done, but the circulation types typically evolve during the classification process itself. These methods are generally used in a much broader community, because they search for general patterns in data. The term objective can be misleading here, and should only be understood in the sense that the classification process itself is objective. Most of the methods still require expert decisions prior to the actual classification process, e.g., such as setting the number of classification types.

The group of objective methods can be further split into a number of sub-families that are discussed in more detail in Huth (1996). One popular and often used subfamily are *k*-means methods (e.g. Hartigan, 1975), because of the fast and easily implementable algorithm. The *k*-means algorithm, but also other objective methods, try to minimize the within-type variance. This means that the (Euclidean) distance of each member of a class to the center of this class, called centroid, should be as short as possible. The major problem here is to find the global optimum among all possible classifications. Due to their formulation, many algorithms only find local optimums. *Simulated annealing* can overcome this problem of finding only a local optimum and is part of the SANDRA classification method used in this study (presented in Section 4.1.2).

4.1.1   Circulation Type Classification in Climate Science

The use of circulation type classifications in climate science has become popular in
recent years. Demuzere et al. (2009) successfully applied a circulation type classifi-
cation to data from a global climate model. They show how pressure fields change
in a changing climate and demonstrate that Western and Central Europe face an
increase in Western circulation and anticyclonic circulation types under an A1B
emission scenario. In a study of present and future storm events, Donat et al.
(2010) show how a change in the frequency of Westerly flow is linked to a change
in storminess over Europe. Plavcova and Kysely (2011) show that biases in daily
minimum and maximum temperature in an ensemble of regional climate models can
partly be explained by over- and underestimations of characteristic circulation types
in the driving global climate model data. A recent study by Cretat et al. (2011)
shows the usefulness of boundary data classification to investigate the influence of
different weather regimes on internal variability for a South-African domain. With
their circulation type classification they are able to attribute strong and weak in-
ternal variability phases to recurrent synoptic situations of the inflow/outflow mass
fluxes through the domain boundaries.

To investigate the influence of boundary forcing variability on the internal variability
of REMO, a circulation type classification of the boundary data has been performed.
As input data for the circulation type classification not the original ERA-40 data has
been used, but rather the interpolated ERA-40 data which is used to drive REMO.
This allows one to directly investigate the variability in the forcing data that might
be altered due to the interpolation procedure. In addition, the domain for the
circulation type classification has been extended by 30 grid boxes in the zonal and
20 grid boxes in the meridional direction at each boundary. The extension has been
done to account for influences from the flow in the vicinity of the model domain.
Figure 4.1 shows the orography of the boundary data domain. The REMO domain
used for the simulations is shown as a black rectangle.

To perform the circulation type classification of the boundary data, the circulation
type classification software of the European Cooperation in Science and Technology
(COST) Action 733 *Harmonisation and Applications of Weather Type Classifications
for European regions* (Philipp et al., 2010) in version 1.0 was used. As there are
many different kind of classification methods available, several set-ups with different
methods were tested. It was found that the outcomes did not depend too much on
the method which gives confidence in the robustness of the results. Here, one set
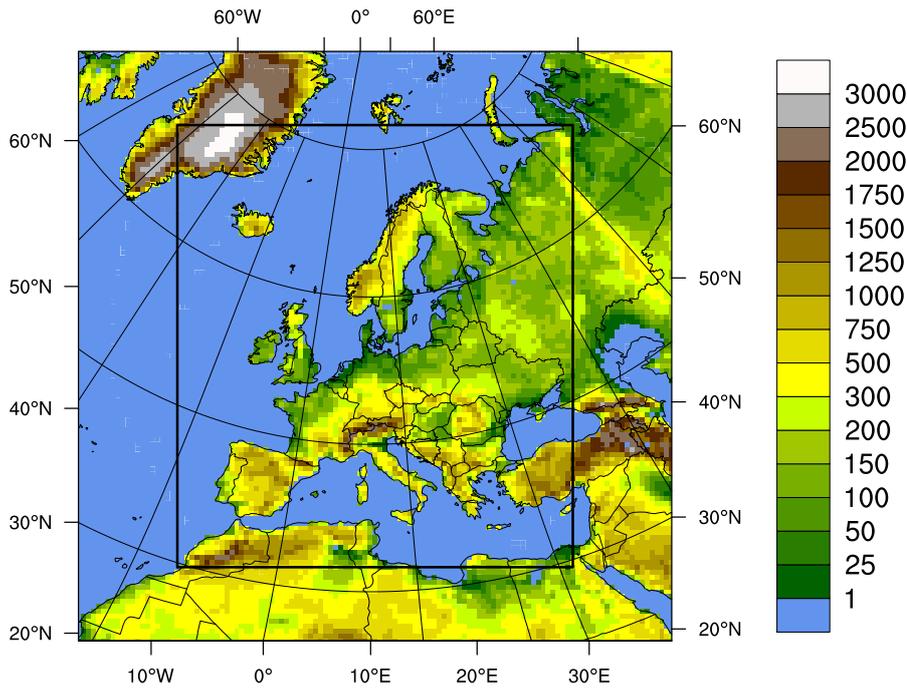
Figure 4.1: Orography of the circulation type classification domain the in m. The domain for the REMO simulations is indicated by the black rectangle.

up for the SANDRA classification method is presented.

4.1.2   The SANDRA Circulation Type Classification

The SANDRA circulation type classification method by Philipp et al. (2007) combines the two concepts of *simulated annealing* and *diversified randomization.* The aim of the algorithm is to have a minimum within-type variability for each class of the classification (Philipp et al., 2010). The basic idea of simulated annealing is that during the search for the global optimum also less optimal states are allowed. Figure 4.2 illustrates this in a typical optimization problem for a one dimensional case. The task in this example is to find the highest hill along the shown transect across a mountain range. If the starting point is at the red line, most algorithms will only search the gray shaded section and find the local maximums to the left or the right, because they would only be allowed to find *more optimal*[1] states. A more optimal state would mean in this case that only paths uphill are allowed, because the new state is higher (more optimal) compared to the old. Starting at the black

---

[1]The term *more optimal* is a commonly used term in the field of optimization algorithms, which can be understood in the sense of better.
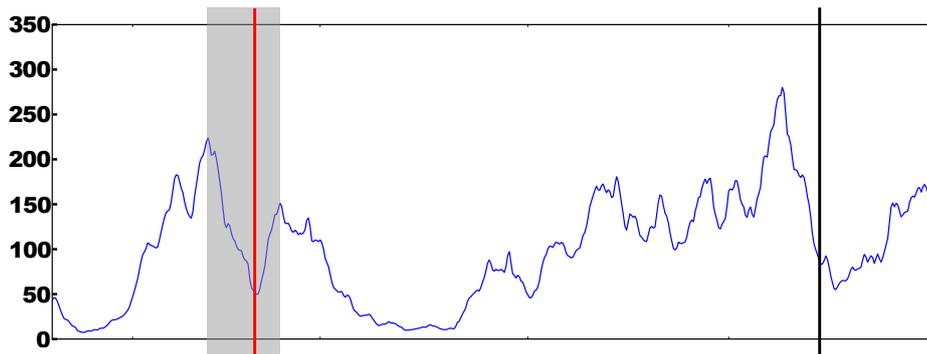
Figure 4.2: Schematic to indicate the optimization problem of finding the highest hill. Many algorithms like conventional *k*-means can only find the local maximums in the gray shaded section when starting at the red line. Finding the global maximum depends on the starting point. More sophisticated methods like SANDRA have a higher probability to find the global maximum regardless of the starting point because they allow downhill paths during the optimization procedure and can search the entire cross section. See text for more details.

line compared to the red one would yield the global optimum, but this happens only by chance due to the adequate initial conditions. This is a typical problem of normal *k*-means methods and demonstrates one of their major disadvantages that is the poor consistency between two classifications when using different starting points (Huth, 1996).

With simulated annealing less optimal states or paths downhill are allowed with a certain probability. In principle, this algorithm allows to search the entire cross section for the highest mountain. The probability to go downhill is controlled by the *acceptance probability function* that depends on the current and new state as well as a *cooling temperature*. The cooling temperature is the reason for the term annealing. It describes the process of controlled cooling of metals in metallurgy to optimize the alignment of metal molecules. The cooling temperature in simulated annealing decreases with every iteration of the search, making it less likely to go downhill (or move to less optimal states), thus leading to a termination of the algorithm. Depending on the starting temperature and the cooling factor used to reduce the temperature from one iteration to the next, the SANDRA method can be computationally demanding.

To allow for the algorithm to terminate in a reasonable time, Philipp et al. (2007) make use of the concept of diversified randomization. Diversified randomization runs

a simple circulation type classification method several times with randomized start-
ing partitions. In addition, the classification process is randomized itself. By using
performance measures in the comparison of different runs, the best run is picked as
the classification. This procedure makes it more likely to reach the global optimum
without running the algorithm infinite times. The combination of both simulated
annealing and diversified randomization have been proved to lead to partitions that
are closer to the global optimum and more stable in terms of consistency compared
to the commonly used *k*-means classification methods. Beck and Philipp (2010)
showed that for circulation type classifications using mean-sea-level pressure as in-
put parameter, SANDRA often times shows the best skill in performance measures
for circulation type classifications.

Set-up of SANDRA

The assumptions needed for SANDRA prior to the classification procedure are based
on the work done in COST Action 733 and by Philipp et al. (2007). Philipp et al.
(2007) could show that finding the perfect number of types a priori is not straightfor-
ward and often subjective decisions have to be made. As the focus is on the influence
of the large-scale flow on internal variability, the parameters used to perform the
classification are daily means of mean-sea-level pressure and 500 hPa-geopotential
height. Tests have been performed with different parameters and parameter com-
binations, e.g., to include vorticity or leave out mean-sea-level pressure, but results
were not very sensitive to these choices (not shown). The combination of mean-sea-
level pressure and 500 hPa-geopotential height lead to the best Explained Cluster
Variance (ECV) value (Philipp et al., 2007) among the tested parameter combina-
tions.

The boundary forcing data is split into the four seasons winter (December-February),
spring (March-May), summer (June-August) and autumn (September-November).
This is done to account for the strong seasonality in the northern hemisphere extra-
tropics (e.g., Wallace et al., 1993). In the second step, seven circulation types are
chosen for winter and summer, and nine for spring and autumn. This gives 32 circu-
lation types in total for the entire year. It has been shown by Philipp et al. (2007)
that a higher number of circulation types are required in the transition seasons spring
and autumn to get a more balanced distribution in the number of assigned days per
circulation type. Tests with different numbers of circulation types showed that the
chosen numbers yield similar results for all seasons in terms of ECV. It should be

noted that the ECV only allows to compare the quality of the classification between different parameter sets for a given number of types, but cannot determine the best number of types itself. For the number of types the present study relies on the experience from COST Action 733 and is a compromise between a good separation of types, within-type variance and number of days assigned to one type for a solid statistical analysis. The result of the classification is a time series, where for each season the daily means of the boundary data are assigned to one circulation type.

4.2 Results

The Figures 4.3 through 4.7 show the 28 different circulation types for the four seasons as calculated by the SANDRA method. All depict the centroids of the mean-sea-level pressure in colored shades and the 500 hPa-geopotential height as contour lines for each circulation type. The centroids are calculated as the mean field from all days assigned to one circulation type. The numbers below each circulation type is the number of days that were assigned to each circulation type. For a better distinction all circulation types are numbered consecutively starting in winter. The circulation type number is given in each figure in the lower right corner. In addition the median and interquartile range of daily field mean internal variability for mean-sea-level pressure, near-surface temperature and precipitation are given as error-bar charts for each season.

4.2.1 Winter

In the circulation type classification for winter, many of the circulation types shown in Figure 4.3 (a)–(g) can be associated with well known European circulation types from other classification methods such as, e.g., the Großwetterlagen classification by Gerstengarbe and Werner (2005). One good example is circulation type 1 that shows a subtropical high shifted the north-east and a low over the Barents Sea. This circulation type is similar to a *Nordwestlage*, where the low pressure systems are traveling from Iceland over Scandinavia towards Russia. Another typical circulation type would be circulation type 6 which can be associated with a *Westlage*. In the case of a Westlage, the tracks of the synoptic disturbances are shifted to the south, so that they can influence central Europe. Overall circulation type 6 shows a strong meridional gradient in mean-sea-level pressure similar to circulation type 5.
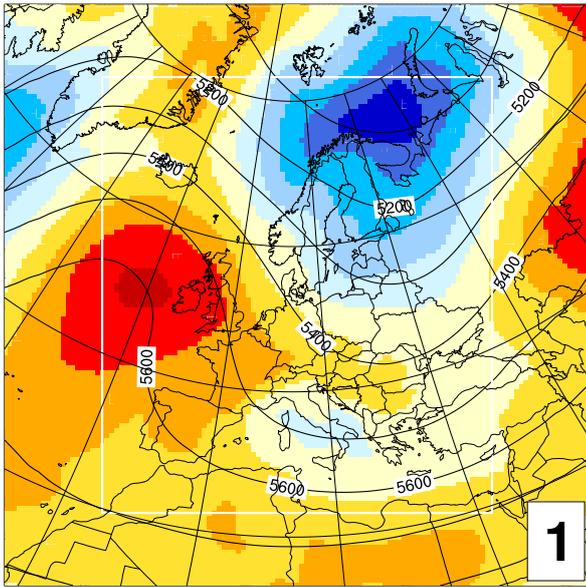
(a) 126 days
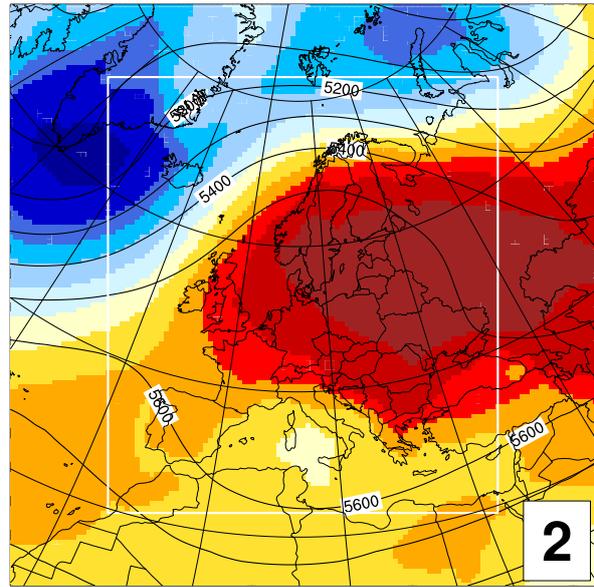
(b) 116 days
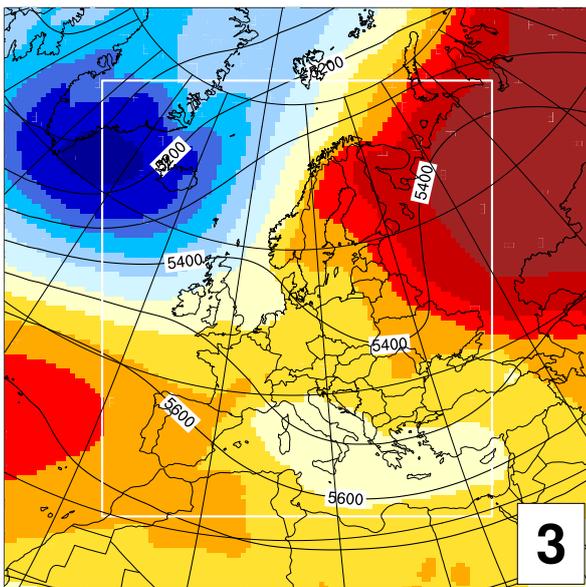
(c) 151 days
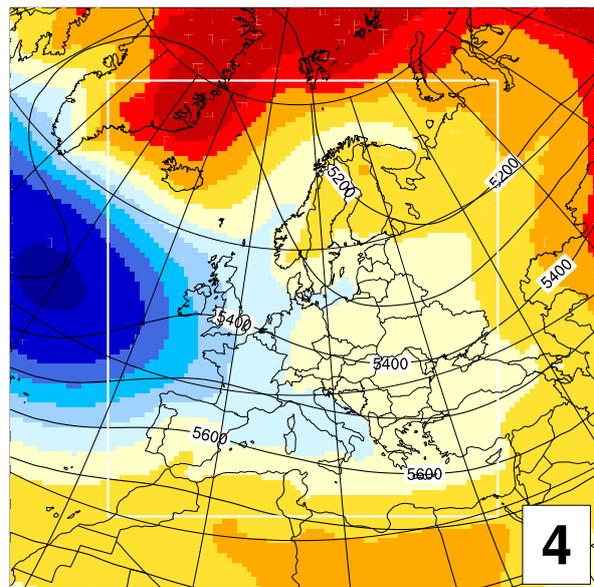
(d) 83 days

Figure 4.3: (a)–(g) winter circulation types of the boundary data. Colored shades show the centroids of mean-sea-level pressure field in hPa. Solid lines are the centroids of the 500 hPa-geopotential height field in gpm with a 100 gpm contour interval. The white rectangle highlights the position of the model domain. The circulation type number is given in the lower right corner of each figure. In (h) the level of internal variability for mean-sea-level pressure (MSLP, blue), near-surface temperature (TEMP, green), and precipitation (PREC, red) is given for each circulation type. Dots indicate the median internal variability and errorbars the corresponding interquartile range.
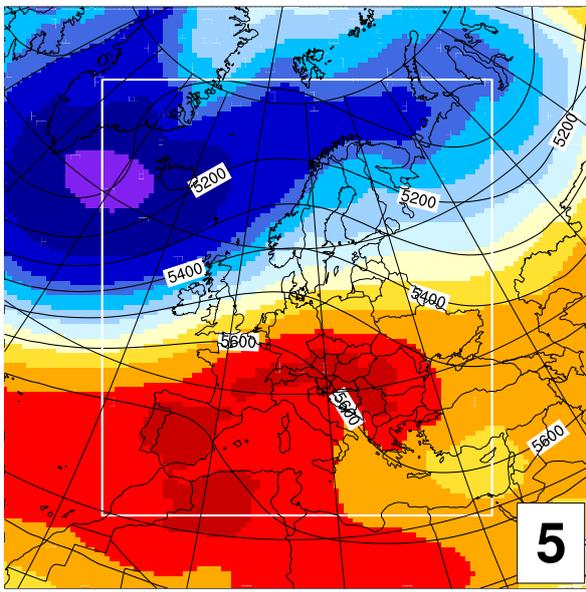
(e) 154 days
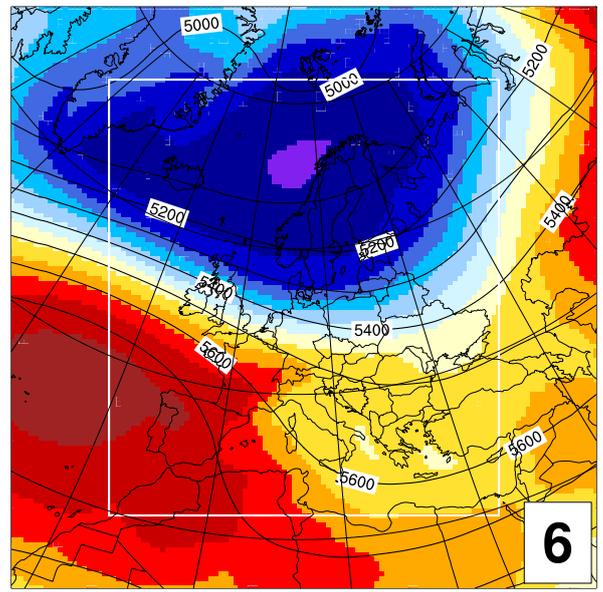
(f) 139 days
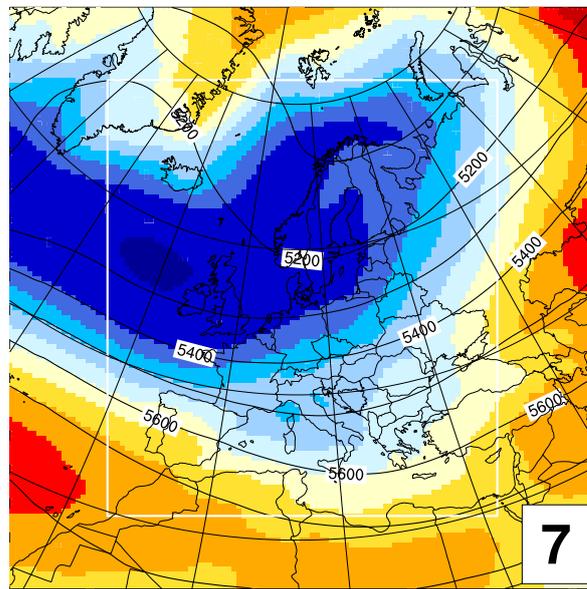
(g) 134 days
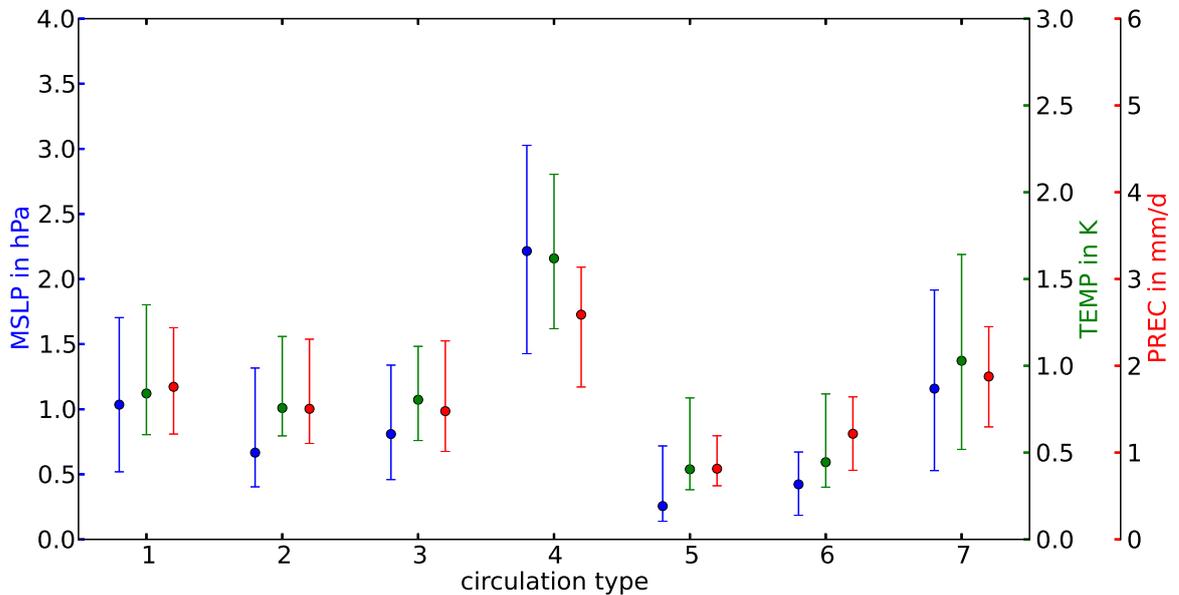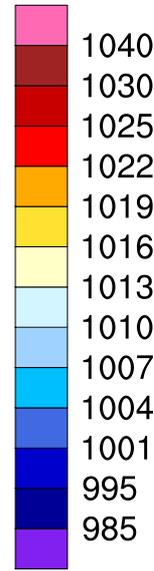
(h)

Figure 4.3: *Continued.*

Figure 4.3 (h) shows the median (dot) and the interquartile range (error-bars) of internal variability for mean-sea-level pressure, near-surface temperature and precipitation for each winter circulation type. It can be seen that in winter certain circulation types, such as type circulation type 4, show a higher median of internal variability than others (e.g., circulation type 6). The circulation types can be roughly categorized into three internal variability groups, with low, medium, and high internal variability. The low internal variability group, consisting of circulation type 5 and circulation type 6, has the strongest meridional mean-sea-level pressure gradients amongst all the winter circulation types. Such situations lead to higher wind speeds and thereby stronger forcing from the boundaries inside the domain. As a consequence, the evolution of internal variability inside the domain is suppressed or quickly advected out of the domain. This is also reflected in the corresponding internal variability strengths. Both mean-sea-level pressure patterns can also be related to a positive phase of the NAO that is characterized by enhanced storm activity and higher wind speeds in central Europe. The median of mean-sea-level pressure internal variability only reaches values of about $0.4\,\text{hPa}$ and near-surface temperature internal variability is only about $0.4\,\text{K}$. For precipitation circulation type 5 and circulation type 6 have different medians, of $0.8\,\text{mm/d}$ and $1.2\,\text{mm/d}$, respectively. The difference can be explained by the higher fraction of convective precipitation in the total precipitation in circulation type 6 compared to circulation type 5. A higher fraction of convective precipitation leads to more variability due to the non-linear and more local processes involved. Thus resulting in higher median internal variability in precipitation.

The medium internal variability group consists of circulation type 1 through circulation type 3 and circulation type 7. For these circulation types the meridional gradients in mean-sea-level pressure are weaker than the low internal variability group. The model has more freedom to develop its own circulation and hence internal variability is stronger. The mean-sea-level pressure internal variability has median values reaching from $0.7\,\text{hPa}$ to $1.3\,\text{hPa}$ and median near-surface temperature internal variability of $0.8\,\text{K}$ to $1\,\text{K}$. Median precipitation internal variability varies between $1.5\,\text{mm/d}$ to $1.9\,\text{mm/d}$.

The high internal variability group is only represented by circulation type 4. Correspondingly meridional mean-sea-level pressure gradients are weak in the center of the domain. The mean-sea-level pressure pattern even shows a outflow zone in the North-West of the domain so that the predominant westerlies cannot suppress internal variability inside the domain. Circulation type 4 can also be associated

with the negative phase of the NAO. Here the storms are usually forced to travel towards the Mediterranean. Central and northern Europe are dominated by dry and cold conditions. The median internal variability reaches 2.2 hPa for mean-sea-level pressure, 1.6 K for near-surface temperature, and 2.5 mm/d for precipitation.

If normalized by the maximum median, mean-sea-level pressure internal variability is almost ten times smaller in the median between circulation type 5 and circulation type 4. The difference becomes smaller with a factor four for near-surface temperature and a factor three for precipitation internal variability. This supports the argument that the internal variability of large-scale parameters such as mean-sea-level pressure is stronger affected by the the forcing field variability as mentioned earlier in Section 3.2, confirming that internal variability in winter is governed by the variability of the boundary forcing.

For winter most of the circulation types are quite distinct, i.e., the differences in distributions of internal variability assigned to these types are highly significant as defined by the Kruska-Wallis-Test. Hence, the flow patterns of these circulation types are linked to the internal variability in the regional climate model. Despite the fact that winter circulation types are linked to the internal variability of a regional climate model, there is still a substantial amount of variability. One reason can be attributed to the transitions between different circulation types because internal variability has a memory, as shown by Nikiema and Laprise (2011) for example. This means that pockets of internal variability need to be advected out of the domain, or dissipated by diffusion within the domain, to lower the level of internal variability. In the opposite direction when going from a lower to a higher internal variability state, it takes some time to fully develop internal variability. This argument is supported by the transition probabilities between the circulation types (not shown). For winter there exists a transition cascade from circulation type 1 to circulation type 4 and then to circulation type 7. This means that the probability of entering circulation type 4 is highest from circulation type 1 and the highest probability of leaving circulation type 4 is moving to circulation type 7. This cascade links the circulation types with the highest levels of internal variability in winter for the investigated parameters mean-sea-level pressure, near-surface temperature and precipitation. This shows the connection between circulation type transition and internal variability for these circulation types and explains parts of the variability of internal variability within each circulation type.

As seen earlier, the mean-sea-level pressure patterns similar to negative and positive
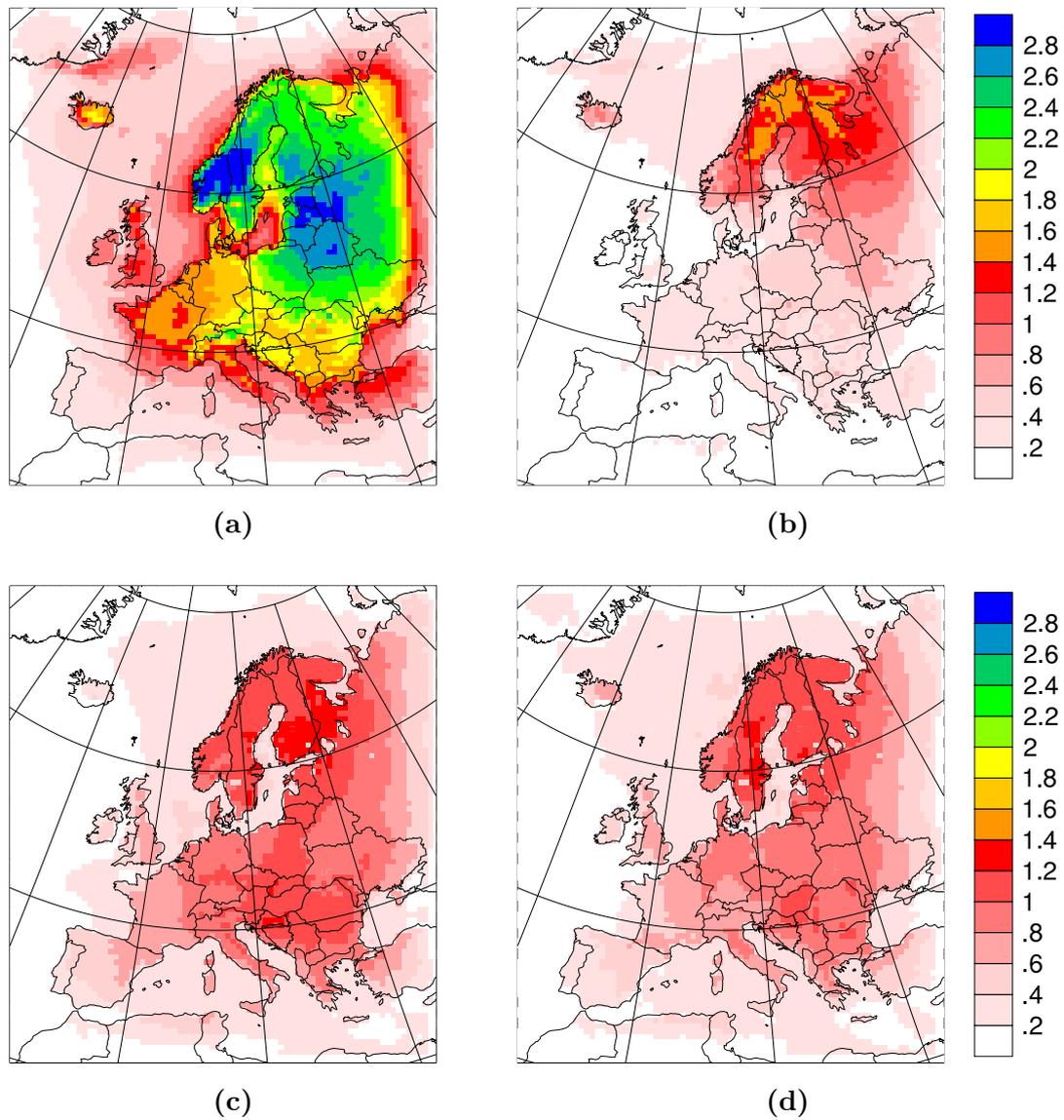
Figure 4.4: Composites of daily mean near-surface temperature internal variability in K for winter (a) circulation type 4 and (b) circulation type 6 and summer (c) circulation type 18 and (d) circulation type 23.

phases of the NAO have large impacts on the spatial mean internal variability. Though their spatial patterns are quite different. Figure 4.4 depicts the composites for near-surface temperature internal variability of circulation type 4 and circulation type 6. A large area centered around the Baltic Sea is subject to large internal variability in case of NAO negative like situations. Here, the mean near-surface temperature internal variability can easily reach 2.5 K and more. In the case of circulation type 6 (Figure 4.4 (b)) the center of main internal variability is shifted to the north and is much weaker with only up to 1.6 K of mean near-surface temperature internal variability. These two patterns closely correspond to the typical tracks of storms in negative and positive phases of the NAO. The main flow in NAO negative situations is weaker and tends to be near the northern and/or southern boundaries of the domain. In NAO positive situations the flow is generally stronger and towards the center of the domain, thus suppressing internal variability in the center.

4.2.2   Spring

The circulation type classification for spring is shown in Figure 4.5 (a)–(i). Several spring circulation types have similarities with the winter circulation types, e.g., circulation type 14 that looks similar to the positive NAO-like patterns circulation type 5 and circulation type 6, though the occurrence of circulation type 14 is less frequent. Other examples include circulation type 16, which is similar to circulation type 1, but with the trough moved further to the south; and circulation type 11 that is similar to circulation type 3. In spring also different circulation types appear with generally weaker gradients in mean-sea-level pressure. The appearance of new circulation types with weaker gradients in the transition season spring is to be expected as summer mean-sea-level pressure gradients are weaker in Europe. This leads also to a problem in the circulation type classification for spring. The number of days assigned to circulation type 9 is much higher compared to the remaining circulation types. It is a circulation type that pools a lot of typical summer flow situations. To minimize this pooling effect the number of circulation types was set to nine for the transition seasons as mentioned earlier. A higher number would improve the balance further, but would also lead to circulation types having less than 40 days. This would make reliable statistics difficult. During the optimization phase for finding the best number of circulation types it turned out that nine classes are a good compromise for the transition seasons giving similar numbers in the ECV as winter and summer circulation type classifications.
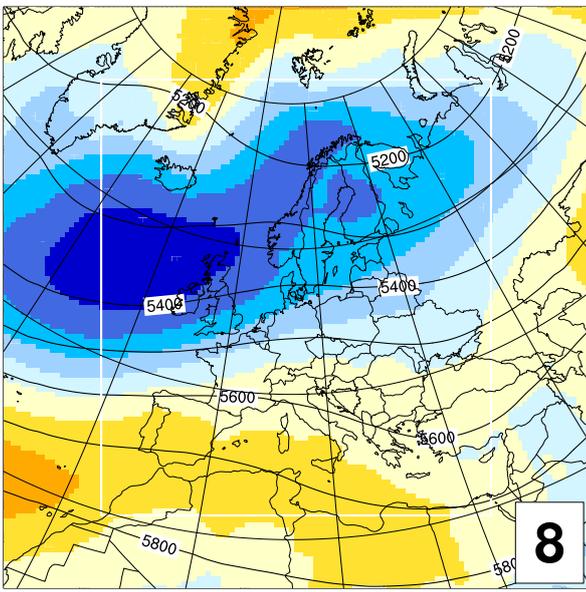
(a) 98 days
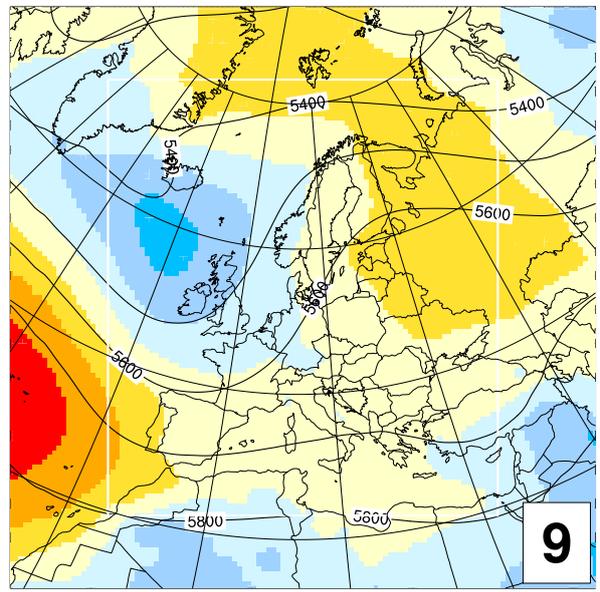
(b) 182 days
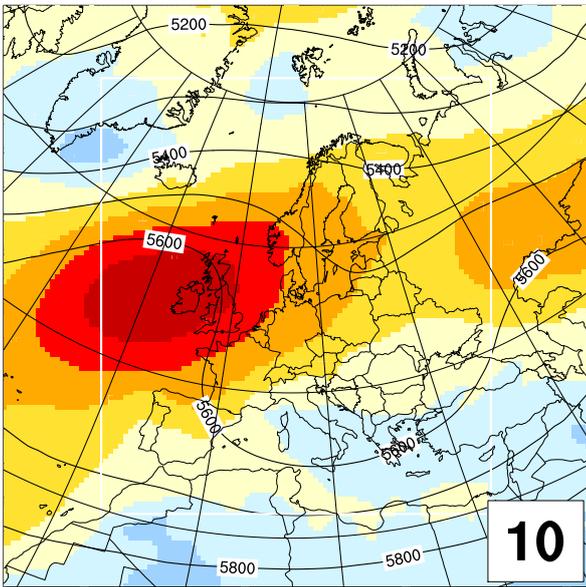
(c) 121 days
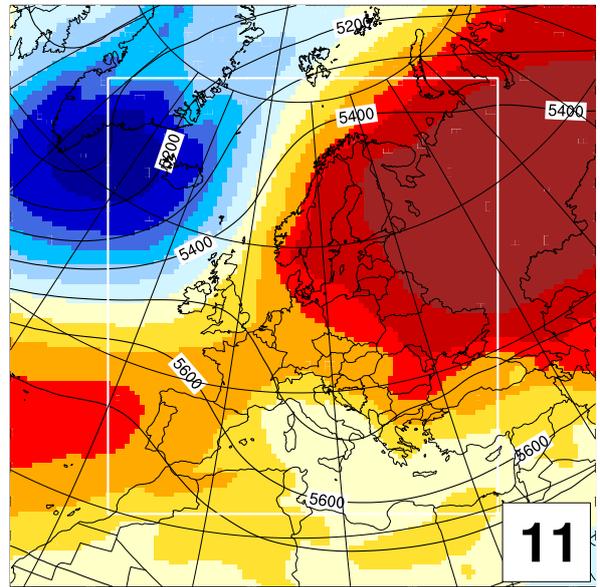
(d) 59 days
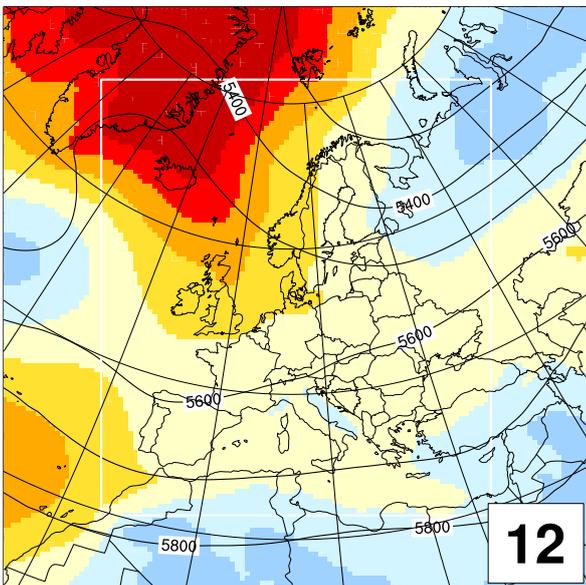
(e) 104 days
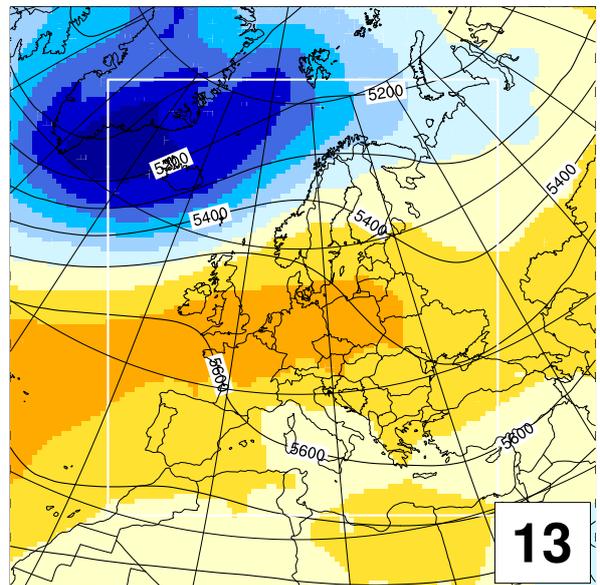
(f) 93 days

Figure 4.5: Same as Figure 4.3 but for spring circulation types.
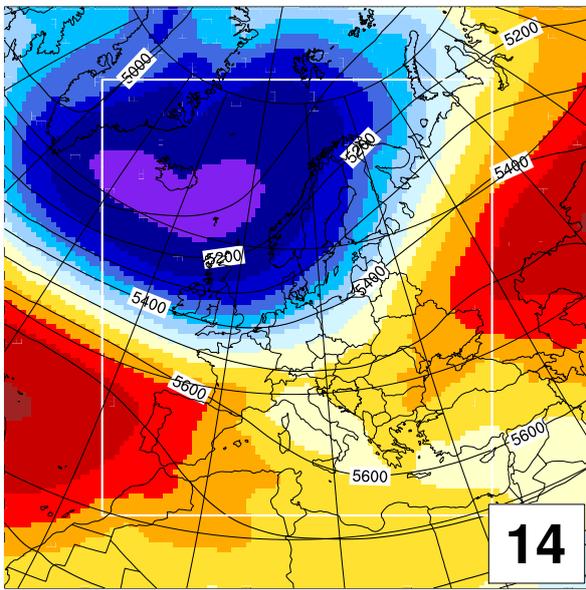
(g) 43 days
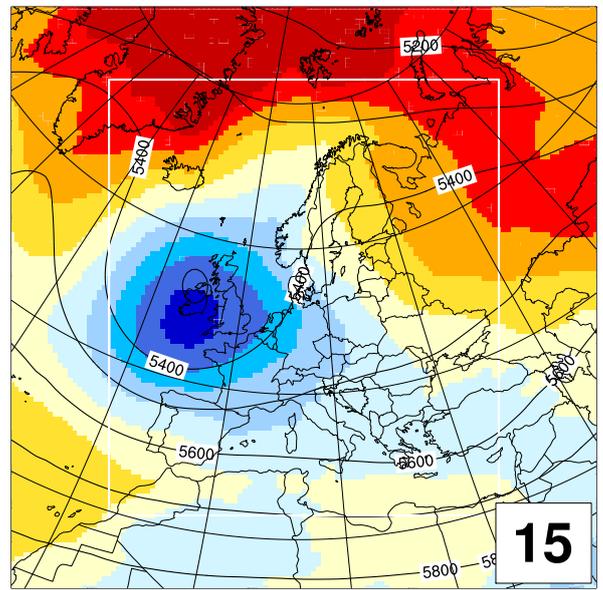
(h) 93 days
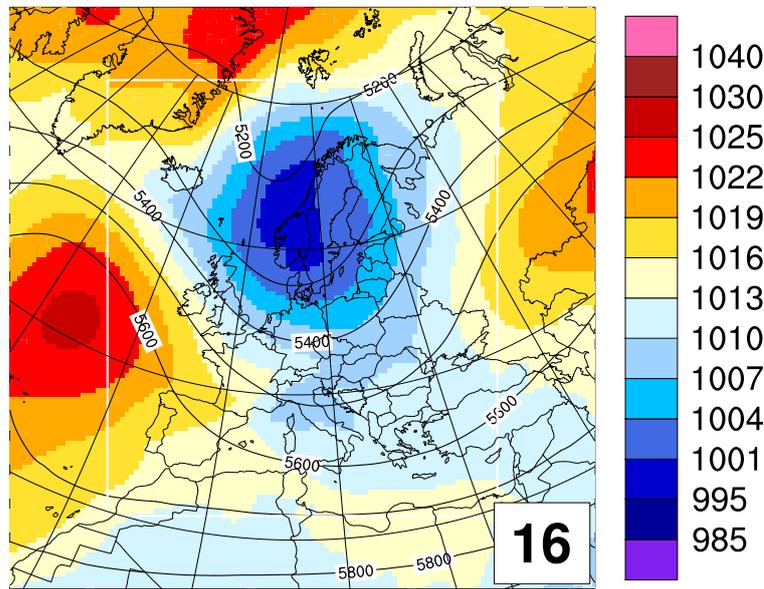
(i) 127 days
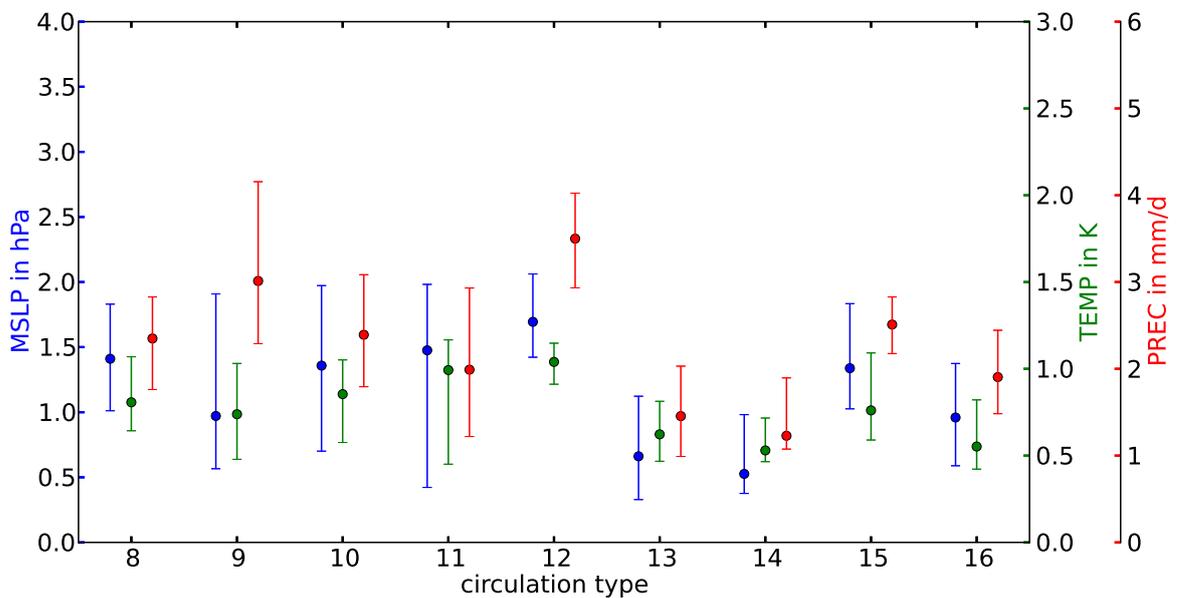
(j)

Figure 4.5: *Continued.*

In terms of internal variability for each circulation type in spring, the picture is not as clear as for winter. Circulation type 14 with the strongest forcing from westerly flow (Figure 4.5 (b)) has the weakest internal variability for all three parameters. In the case of near-surface temperature this is only half of the internal variability compared to circulation type 12 with a median of 1 K. The major difference to winter is that for at least mean-sea-level pressure and near-surface temperature no circulation type with really high internal variability exists (Figure 4.5 (h)). One reason might be that there is no corresponding circulation type to circulation type 4 in spring. This means that the dynamic situation found with circulation type 4 does not occur in spring, which seems to be a necessary condition for strong internal variability at least during this time of the year. Only for precipitation circulation types with higher internal variability compared to winter appear. This is especially the case for circulation type 9 and circulation type 12. They show generally weaker forcing from the boundaries and represent more summer circulation types. This is in good agreement to the finding of Chapter 3 that in spring precipitation internal variability is getting stronger especially towards summer compared to winter.

4.2.3   Summer

The summer circulation types in Figure 4.6 (a)–(g) show a rather different picture compared to those of winter. All circulation types show different strengths of the sub-tropical high over the Azores with varying influences on central Europe; reflecting the different flow regime of the summer months compared to winter. The strength of internal variability is very similar for all circulation types (Figure 4.6 (h)), except for circulation type 19 which has lower median values for all three parameters compared to the other circulation types. Circulation type 19 has the strongest forcing from westerlies in summer (Figure 4.6 (c)) that looks similar to a positive NAO-like pattern. Interestingly circulation type 19 resembles a positive NAO-like pattern of autumn NAO (Hurrell et al., 2003, see). The high frequency of occurrence towards late August (not shown) shows that circulation type 19 can indeed be identified as a circulation type that marks a transition towards autumn. Nevertheless internal variability is stronger compared to similar circulation types such as circulation type 5 in winter or circulation type 14 in spring for at least mean-sea-level pressure and precipitation. One reason is the weaker gradient in mean-sea-level pressure, but also the higher importance of local processes in summer play a role. This means that flow patterns can only modulate the internal variability within the

domain in summer. Most of the internal variability is more related to regional and local-scale processes as already suggested by, e.g., Christensen et al. (2001).

The independence of the internal variability from the boundary conditions in summer can also be seen in the spatial pattern, which looks rather similar for different circulation types. To demonstrate this Figure 4.4 shows the mean internal variability of near-surface temperature for (c) circulation type 18 and (d) circulation type 23. Except for small differences in strength the patterns are the same. Both are also rather similar to the overall summer mean pattern (Figure 3.5 (c)). Hence, the development of internal variability in summer is governed by local processes.

4.2.4 Autumn

The autumn circulation types in Figure 4.7 (a)–(i) show many similarities to the spring circulation types. This is to be expected, as both are transition seasons. One major difference between these two seasons is that autumn is dominated by what Gerstengarbe and Werner (2005) define as *Westlagen*. This means that westerlies dominate the flow and storms can travel rather unhampered through the domain. Circulation type 27, circulation type 29, and circulation type 32 are representatives of the *Westlagen* and appear more often in autumn compared to the other seasons. Therefore, the strength of internal variability is the lowest among all seasons for mean-sea-level pressure and near-surface temperature. Only precipitation is of similar strength in internal variability compared to spring.

It is noteworthy that no pattern representing a negative NAO phase is found for autumn. This is in good agreement with earlier studies, because negative NAO phases are also in close relation to blocking situations over Europe. As seen earlier, the frequency of blockings in the Euro-Atlantic sector is at a minimum in autumn (see Figure 3.3 (a)). The link between NAO negative phases associated with blockings and high internal variability inside the model domain is further investigated in the following chapter.

In autumn the problem of an unbalanced assignment of days to circulation types, as seen for spring, is not so crucial. Here, the increase from seven to nine circulation types helps to better separate the different types (not shown). The overall weak internal variability can only partly be explained by the domination of westerly flows, otherwise one would expect levels of internal variability similar to circulation type 5 and circulation type 6. One explanation might be the memory in internal variability
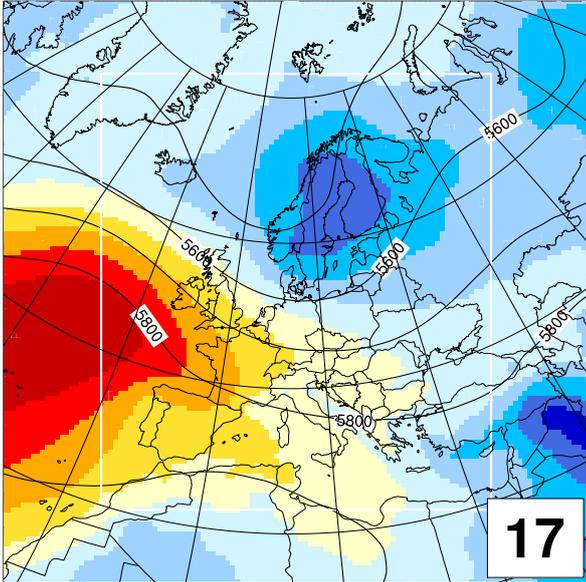
(a) 123 days
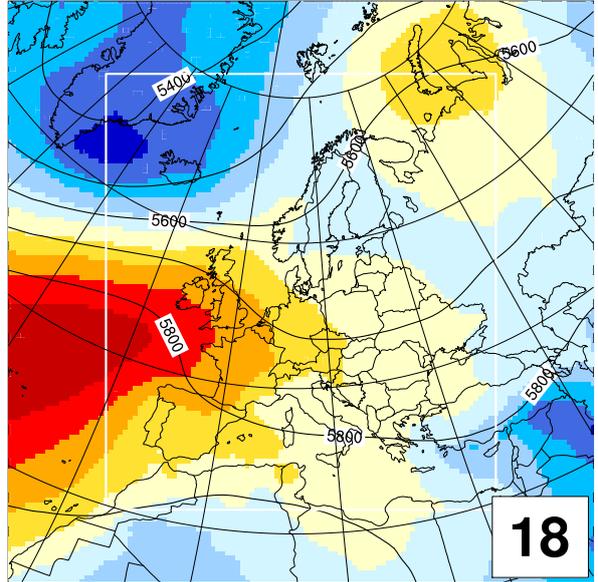
(b) 121 days
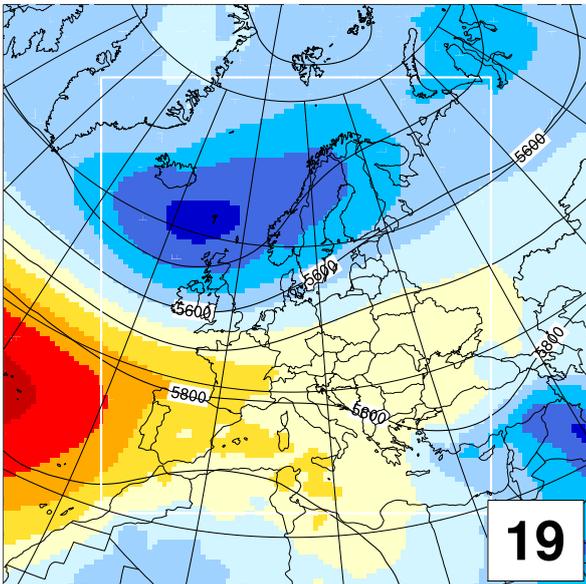
(c) 122 days
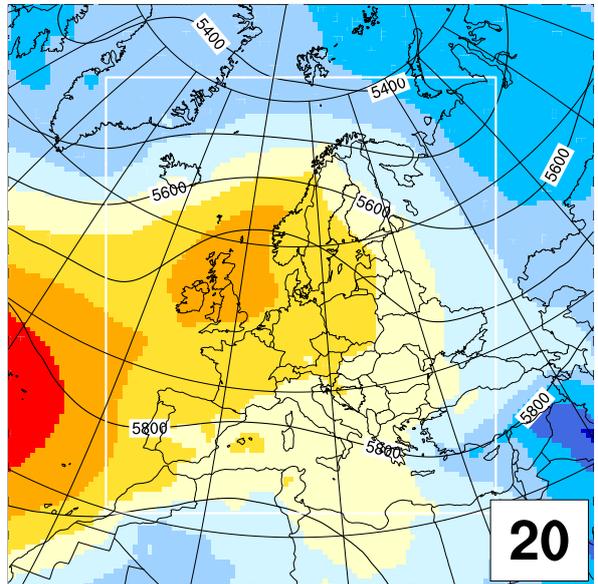
(d) 147 days

**Figure 4.6:** Same as Figure 4.3 but for summer circulation types.
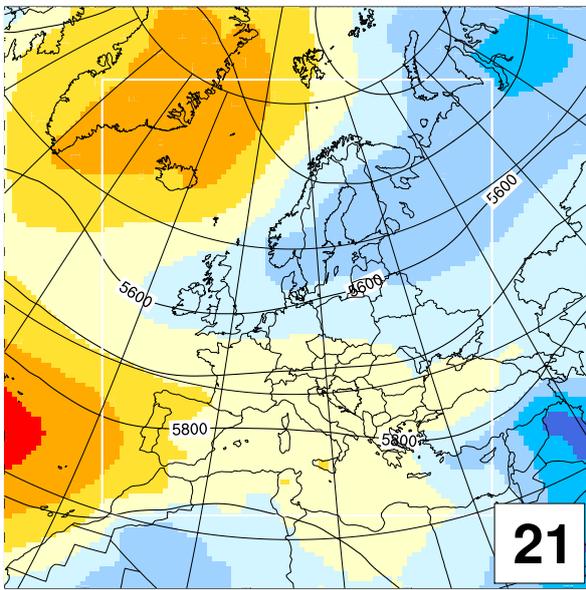
(e) 127 days
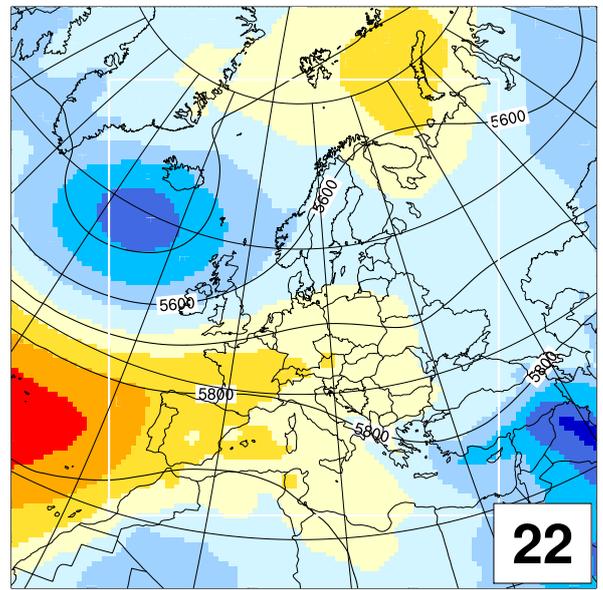
(f) 157 days
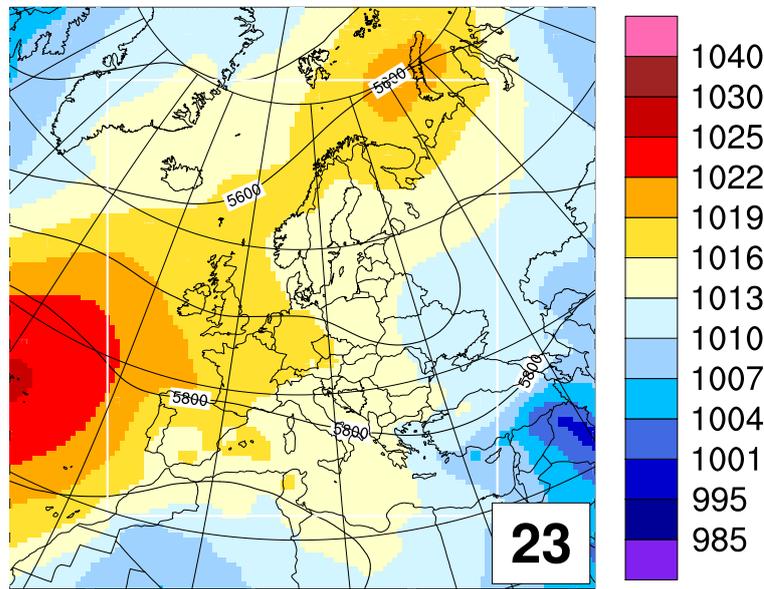
(g) 123 days
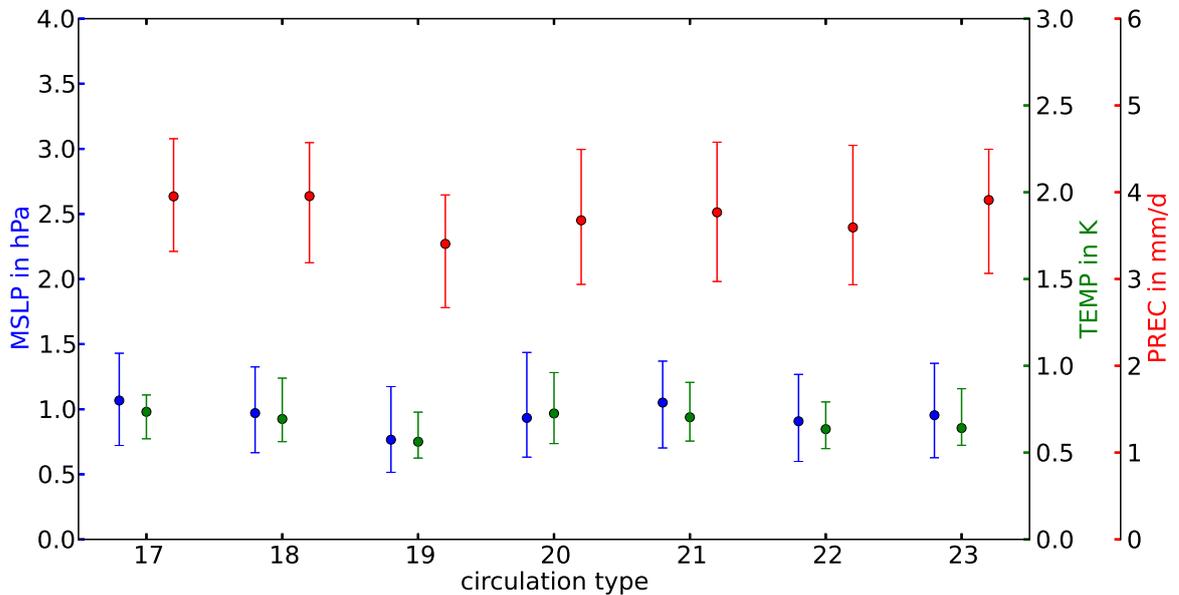
(h)

**Figure 4.6:** *Continued.*
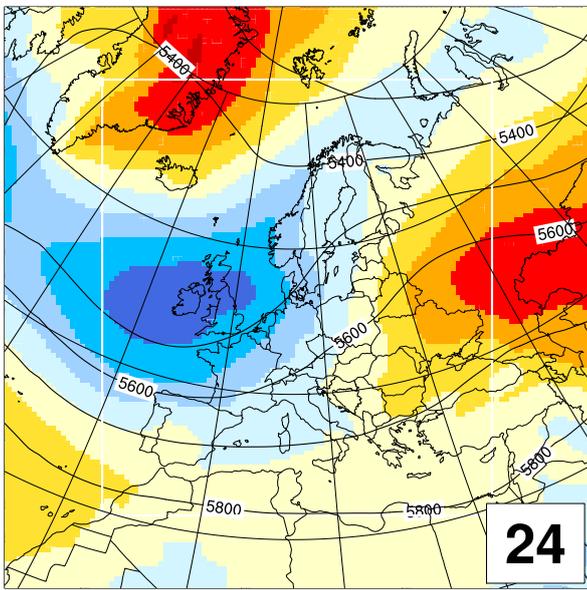
(a) 97 days
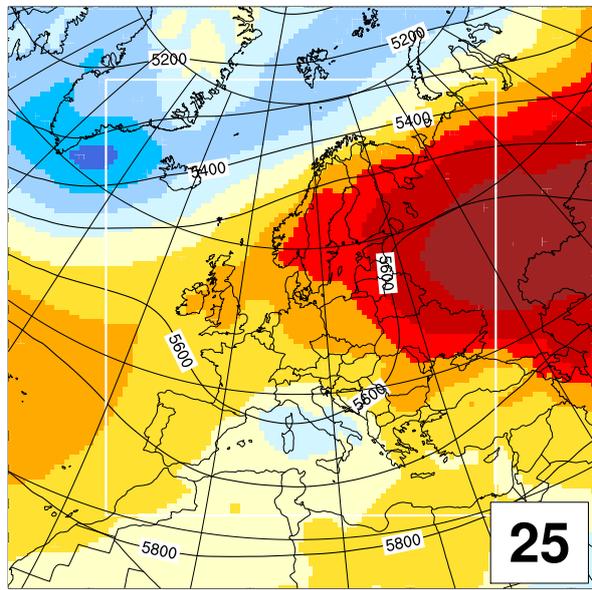
(b) 65 days
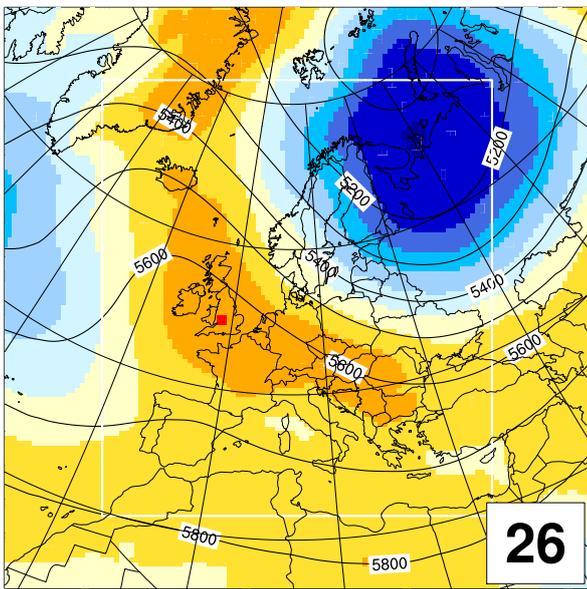
(c) 90 days
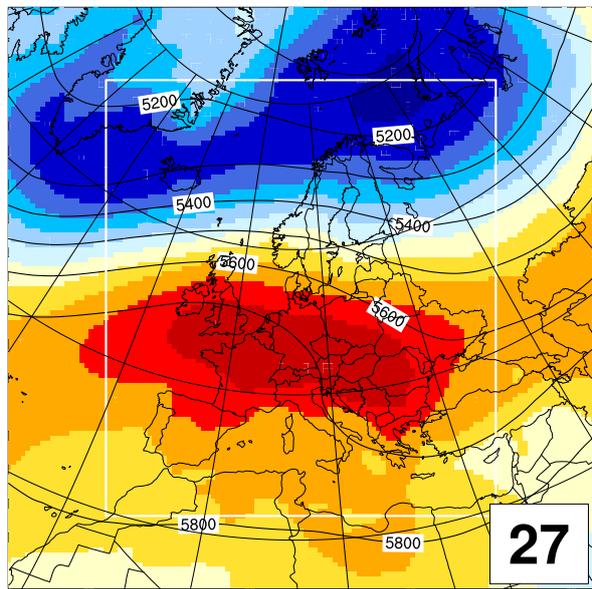
(d) 95 days
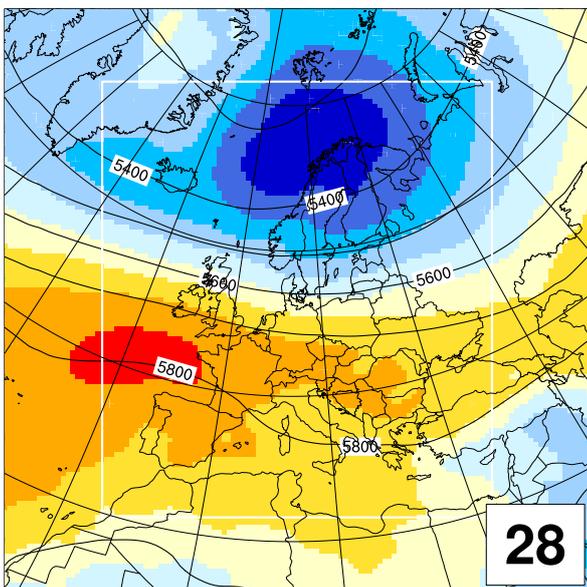
(e) 132 days
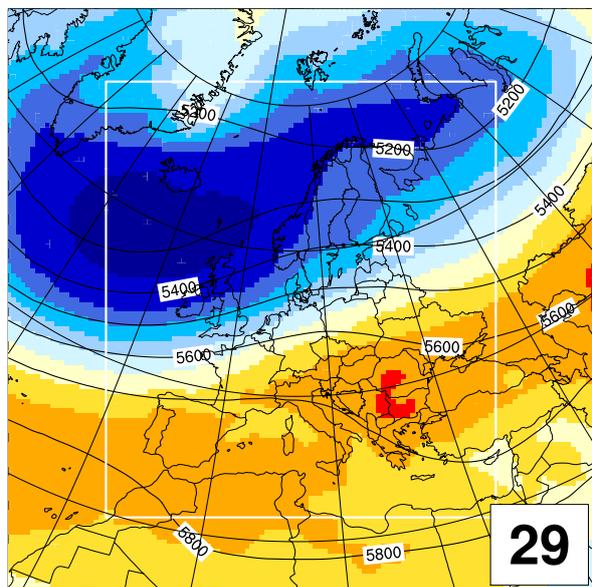
(f) 94 days

**Figure 4.7:** Same as Figure 4.3 but for spring circulation types.
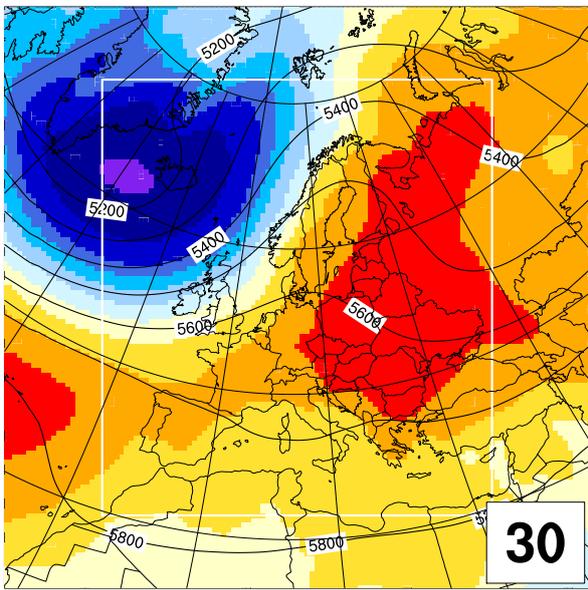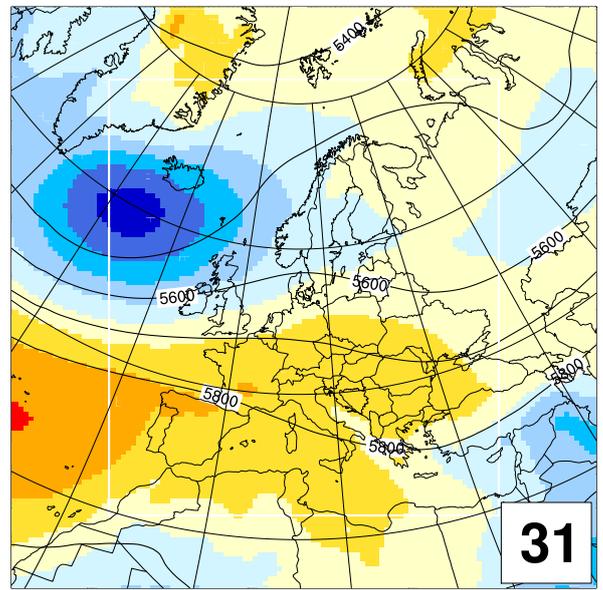
(g) 99 days   **(h)** 126 days
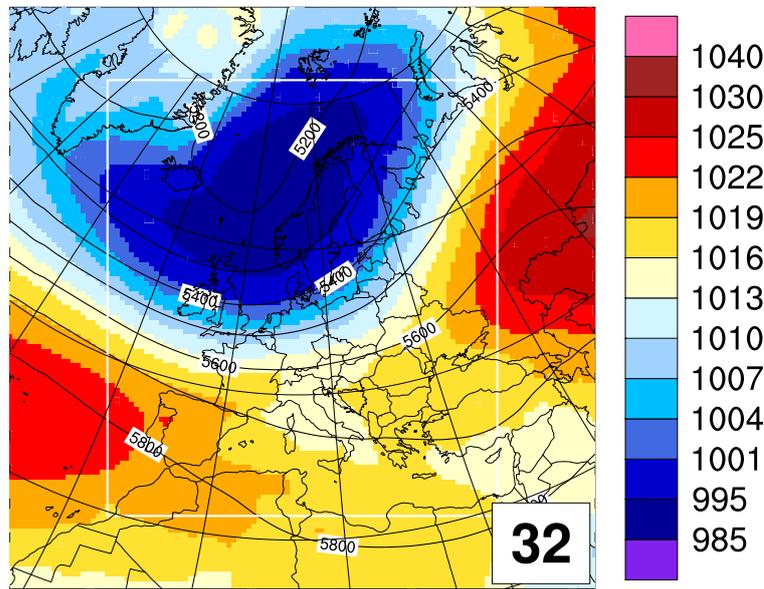
(i) 112 days
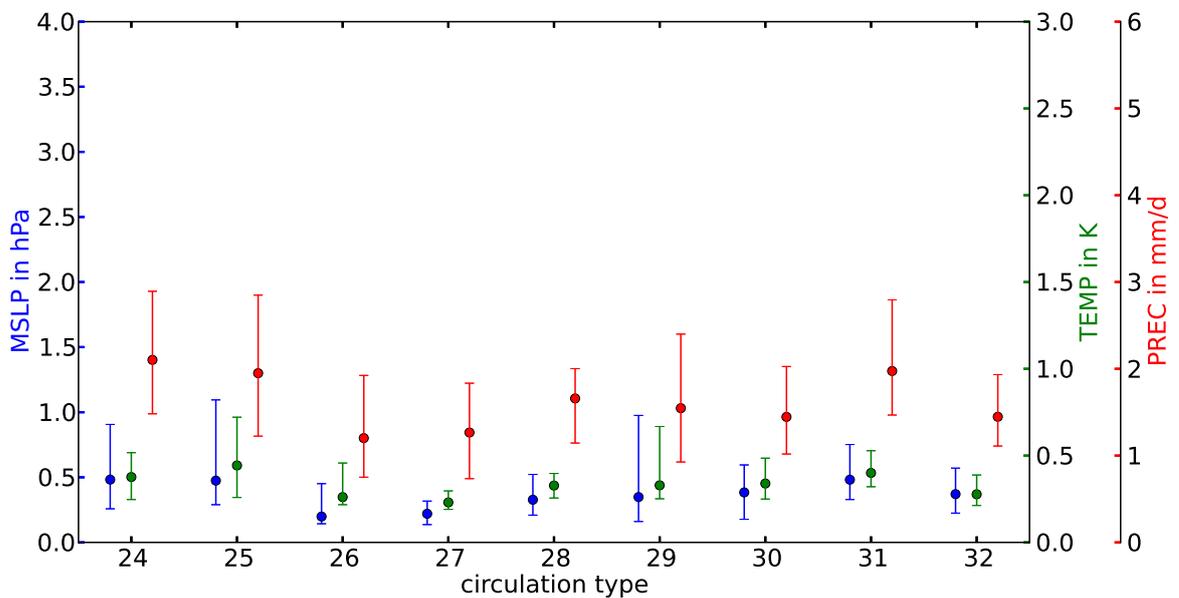
(j)

Figure 4.7: *Continued.*

mentioned earlier. As there are hardly any situations that can build up internal variability, it can be expected that internal variability is lower in circulation types that are comparable to other seasons.

4.3   Conclusions

The circulation type classification of the lateral boundary forcing has shown that the episodic behavior of internal variability can be related to the variability of the boundary forcing as already speculated by Laprise et al. (2012). This is especially the case for the winter season. In winter, NAO-like patterns have the strongest influence on the strength of internal variability inside the domain, with high (low) internal variability for NAO negative (positive) like circulation types. This can be explained by the strength of the westerly flow that is stronger in NAO positive compared to NAO negative phases (Hurrell et al., 2003). For summer the weakest influence of circulation types on the strength of internal variability is found, which leads to the same conclusion drawn by Caya and Biner (2004) and Christensen et al. (2001) that internal variability in summer is closely related to local processes. The transition seasons show a mixed behavior. In both seasons circulation types with strong westerly flows show in general weaker internal variability and vice versa. This effect, however, becomes weaker for parameters that are more related to local processes like precipitation. Together with a deeper analysis of the role of different NAO phases, the processes leading to high internal variability phases are investigated in more detail in the following chapter.

Chapter 5

The Role of Winter NAO for the Internal Variability

In this chapter, the links between positive and negative NAO patterns with states of weak and strong internal variability, as found in Chapter 4, are further investigated. The winter season is selected because the relationship between NAO and internal variability is strongest. To better understand the processes related to the generation of internal variability a case study of a high internal variability event, during a strongly negative NAO phase, is presented. To quantify the dependence of internal variability on NAO phases, a daily NAO index is used and correlated with the field-mean internal variability. Building upon a theory which links eddy-driven jet stream regimes to different phases of the NAO, an attempt is made to diagnose internal variability phases from an the lateral boundary data. The main research question tackled in this chapter is: *Is it possible to determine the strength of internal variability from the variability of the boundary data?* In the following Section 5.1 the NAO and the derivation of the daily NAO index is explained. In Section 5.2 results from the different views on internal variability are presented and conclusions are given in Section 5.3.

5.1   The North Atlantic Oscillation (NAO)

The NAO has been intensively studied during the last decades because of its influences on the climate from the East-American coast to Siberia (see Hurrell et al., 2003, for a review). The NAO is the predominant mode of climate variability and
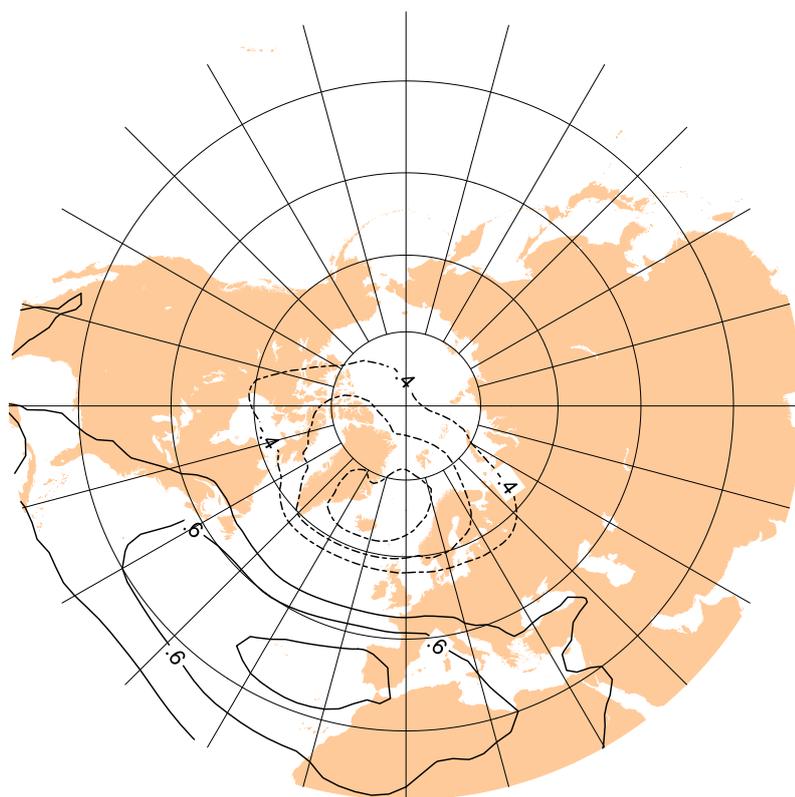
Figure 5.1: Correlation map computed from the first principle component of an EOF analysis of winter (December to February) monthly mean mean-sea-level pressure using ERA-40 data from 1957 to 2002.

has strong impacts on ecosystems and society, especially in winter. The long history of NAO studies (of which some studies essentially describe the same phenomena, but do not name it NAO) came up with different definitions of what the NAO actually is (Stephenson et al., 2003). To date, there is no consensus on the definition but the essential ideas of what the NAO is, are very similar. The NAO is understood as a dipole structure of low pressure in the northern North-Atlantic with its core around Greenland and Iceland, and high pressure in the area between the Azores and Portugal. Many different indices describing the phases of this dipole exist. These indices range from simple station based measures between Portugal and Iceland to more complex principle component analysis of sea-level pressure or 500 hPa-geopotential height. In most cases, the correlation of these indices is quite high and can be used interchangeable, but seasonal variations in the center of action of the NAO and noise due to transient eddies favor gridded sea-level pressure data (Jones et al., 2003).

As mentioned earlier, the NAO explains climate variability especially in winter, and

as such, only the winter NAO is discussed in this chapter. Figure 5.1 shows the NAO in terms of a homogeneous correlation map of the first Empirical Orthogonal Function (EOF) from mean-sea-level pressure anomalies. Many indices describe two different phases of the NAO. They are generally understood as a positive and a negative phase relative to the climate mean state.

The positive phase of the NAO is characterized by enhanced meridional pressure gradients that results in stronger westerly winds towards northern and central Europe. As a consequence, relatively warm and moist air masses are transported into northern and central Europe leading to wet and warm conditions in these regions. Southern Europe simultaneously faces drier conditions. The negative phase of the NAO, in turn, has weaker meridional pressure gradients and weaker westerlies. In this case, central and northern Europe are under the influence of cold and dry air masses, whereas southern Europe has more storms and wetter conditions.

The basic structure of the NAO is likely to evolve from the internal, nonlinear dynamics of the atmosphere, but there is evidence that it can be modulated by external forcings like sea-surface temperature anomalies, snow pack, sea-ice extend, and trace gas compositions (see Thompson et al., 2003, for a review). The ability to modulate the NAO by external forcings also gives rise to the hope of some predictability of the NAO on a seasonal to interannual basis, although it is most likely to be low (Hurrell et al., 2003). Most indices describe the NAO as a monthly or seasonal mean because transient eddies can introduce a lot of fluctuations (or noise) on a daily basis, especially when using station data. There are, however, important changes of the NAO phase within one month. Therefore, daily indices have been developed.

5.1.1   The Daily NAO Index

To account for day to day variability in the NAO state, a daily NAO index is calculated from ERA-40 data. The construction of the index used in this study, was originally defined by Blessing et al. (2005). Here, a modified version developed by Pinto et al. (2009) is used. The procedure of constructing the daily NAO index is as follows: First, the first EOF from monthly mean mean-sea-level pressure anomalies from October to March for the Euro-Atlantic sector (90°W–50°E and 20°N–80°N) over the entire ERA-40 period (September 1957–August 2002) is calculated. Second, the pattern of the first EOF is projected onto daily mean mean-sea-level pressure anomalies. The daily anomalies are calculated with respect to monthly mean mean-

Table 5.1: Definition of the different NAO phases.

	Phase	Index values	number of days	% days
NAO−−	Strong negative	Index < -1.5	135	7.6
NAO−	Negative	$-1.5 \leq$ Index < -0.5	443	24.9
NAO 0	Neutral	$-0.5 \leq$ Index < 0.5	634	35.6
NAO+	Positive	$0.5 \leq$ Index < 1.5	462	26.0
NAO++	Strong positive	Index ≥ 1.5	105	5.9

sea-level pressure data. This is followed by an 5-day running mean smoothing of the index to minimize the influence from single transient eddies.

The calculation of the daily NAO index used in this study was performed by Pinto (2012, *pers. communication*). Similar to Pinto et al. (2009), the daily NAO index is split into five categories from *strong negative* to *strong positive* states of the NAO. Table 5.1 shows this definition of the different NAO phases and the corresponding index values. Column four and five give the absolute and relative number of days for each phase from the period used for the simulation (1979 to 1988). Although only a ten year period is investigated, the distribution of NAO phases is pretty similar to Pinto et al. (2009) bearing in mind that they used National Centers for Environmental Prediction (NCEP) re-analysis from 1958 to 1998. This gives confidence that chosen period is a good representative for the entire ERA-40/NCEP period.

5.2   Results

Before the results from the correlation of the daily NAO index defined above and the domain averaged internal variability are presented in Section 5.2.2, a case study of a strongly negative NAO phase which analyzes processes leading to rapid growth in internal variability is presented in Section 5.2.1. Making use of the link between NAO and jet stream strength, an internal variability index for predicting the strength of internal variability is presented in Section 5.2.3.

5.2.1   Case Study on a Strong Internal Variability Event

For a better understanding of the processes involved in the development of internal variability and to get a glimpse on the daily and spatial variability, an extreme episode of internal variability is presented in this section. The event takes place between January 1 and 12, 1985 which is characterized by a strongly negative NAO phase. Daily charts for all days of this event are shown and explained in detail in Appendix A. A summary of the most important results and a closer look focusing on the interplay between large and small scale processes leading to internal variability in a case study region is given here.

To analyze the local processes that are related to the generation of internal variability, a region in the South of Norway showing strong internal variability during the episode is investigated. The region is indicated in Figure A.1 by the black box. Figure 5.3 shows the spatial averages of near-surface temperature (2m-T), 850 hPa temperature (850 hPa-T), humidity, cloud cover, wind barbs in 500 hPa, and 500 hPa-geopotential height (500 hPa-Φ) over South Norway. Two ensemble members that show large differences in most of the parameters are highlighted with blue and green lines and symbols, respectively. These two members are explored more thoroughly in Appendix A. The ensemble spread is given as gray shaded area (except for the wind barbs, where other ensemble members are displayed in gray).

In the beginning of the episode, the ensemble stays close together, which can be seen by the narrow gray band in each parameter. Differences up to the 5th of January are mostly driven by differences in the large scale flow, which can be seen in the 500 hPa-geopotential height. This leads to a relatively small spread in temperature and humidity. During this early phase, the near-surface temperature and 850 hPa temperatures stay close together in terms of their internal variability. Starting around January 6 differences can also be seen in the 500 hPa wind-direction and speed. These differences indicate flows of different air-masses into South Norway. Drier and colder air-masses are transported by more easterly winds, whereas warmer and moister air-masses by more westerly winds. This results in a larger spread in cloud cover because of the different air masses. As a consequence, near-surface temperature internal variability becomes much larger than 850 hPa temperature internal variability because of large differences in the energy balance at the surface (not shown). The near-surface temperature internal variability is now strongly modulated by the cloud cover internal variability which can lead to temperature differences of up to 15 K (e.g., around January 11). The near-surface temperature internal

variability is much stronger during this phase compared to the 850 hPa temperature internal variability. Thus 850 hPa temperature internal variability is influenced more strongly by the large scale flow internal variability.

This *cloud cover feedback* is most effective in snow covered areas, due to the good insulation properties of snow. It can partly explain why the maximums in the spatial distribution are found more towards Northern Europe and why internal variability correlates well with snow-pack (see also Section 3.2). This feedback can be understood as a local positive feedback, which injects more internal variability into the system and modulates the internal variability coming from the large scale. It also explains an additional part of the spread in the internal variability associated with the circulation types in Chapter 4.

Figure 5.2 (a) shows an interesting feature of the ensemble which is a clustering of ensemble members. Clustering suggests that there is no single solution, but also no complete freedom in the solutions. In regards to the temporal and spatial evolution this is expressed in the forming of clusters consisting of ensemble members that stay close together. At the same time, the difference between these clusters is large compared to the differences within one cluster. In Figure 5.2 (a) this behavior is expressed by roughly three different groups of solutions. One group is formed by the *red* and the *black* member with only one low pressure core over West Russia. The second group consists of the *orange* and *blue* member. showing a bigger core over West Russia and a second over the Southern Baltic Sea. The third group shows one big system and is formed by 5 members. One member (green) is not so easy to group because it shows a mixture between group two and three. This is consistent to the findings of Alexandru et al. (2007) who investigate the evolution of a low pressure system in an ensemble of regional climate model simulations. They found a similar behavior and explain it by the existence of multiple attractors in situations of strong internal variability. This means that during strong internal variability events multiple states in the space of solutions emerge. However, if the forcing becomes too weak such clusters are hard to detect as seen in Figure 5.2 (b), where the ensemble members show a rather chaotic behavior over South Eastern Europe. After such an event when the boundary forcing becomes stronger again, the solution is forced back to a quasi-unique state and internal variability is low. This behavior also explains the episodic character of internal variability.

Another feature is that the REMO ensemble can show consistently different solutions compared to the forcing (seen at the beginning of the episode in Figures A.2 and
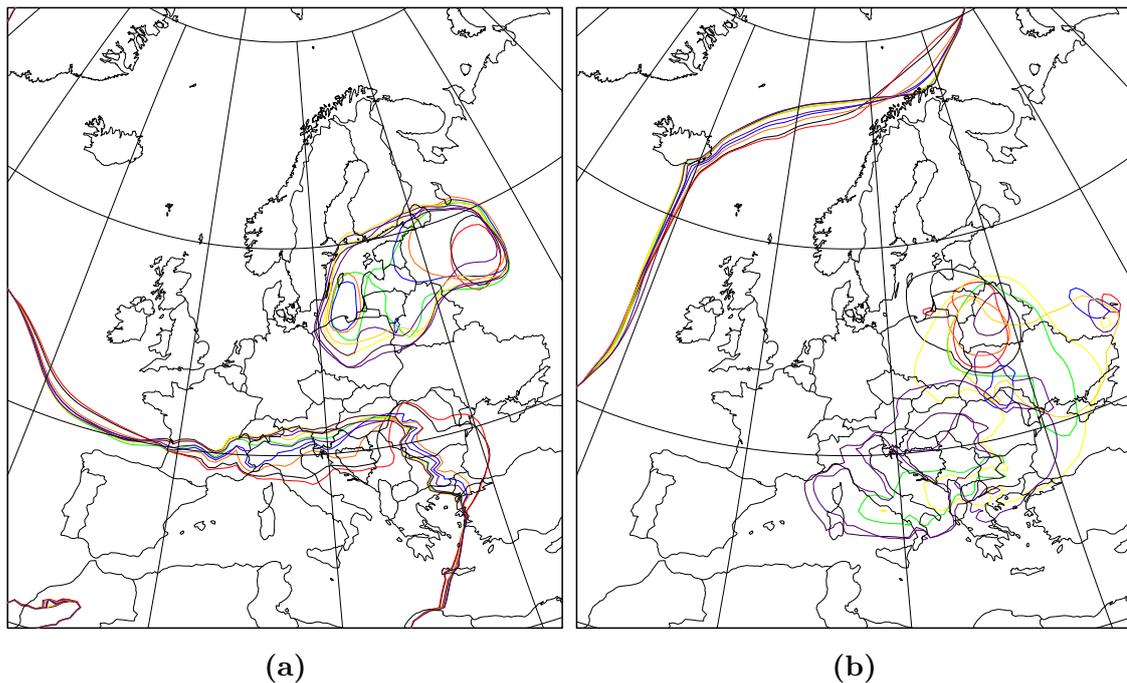
Figure 5.2: Spaghetti plots for two different days during the strong internal variability event. (a) shows the 1010 hPa contour line of mean-sea-level pressure of all ensemble members in different colors for January 6, 1985. (b) shows the same for January 12, 1985.

A.3). The differences in mean-sea-level pressure and 500 hPa-geopotential height to the *observed* solution can be interpreted as model error, because it is an systematic deviation in all ensemble members. It is important to say that this only holds for perfect boundary conditions such as ERA-40. In the case where a global climate model acts as a driver, differences might as well be due to errors in or insufficient resolution of the boundary forcing.

During the entire period discussed here, the jet stream meanders quite significantly. It is a known feature, that such situations are difficult to predict for weather forecast models. It seems likely that situations that bare potential of non-linear behavior, like a meandering jet, can also cause situations of high internal variability. It has been already stated by Nikiema and Laprise (2011) and Diaconescu et al. (2012) that non-linear processes, such as convection and hydrodynamic instabilities, are sources of internal variability.
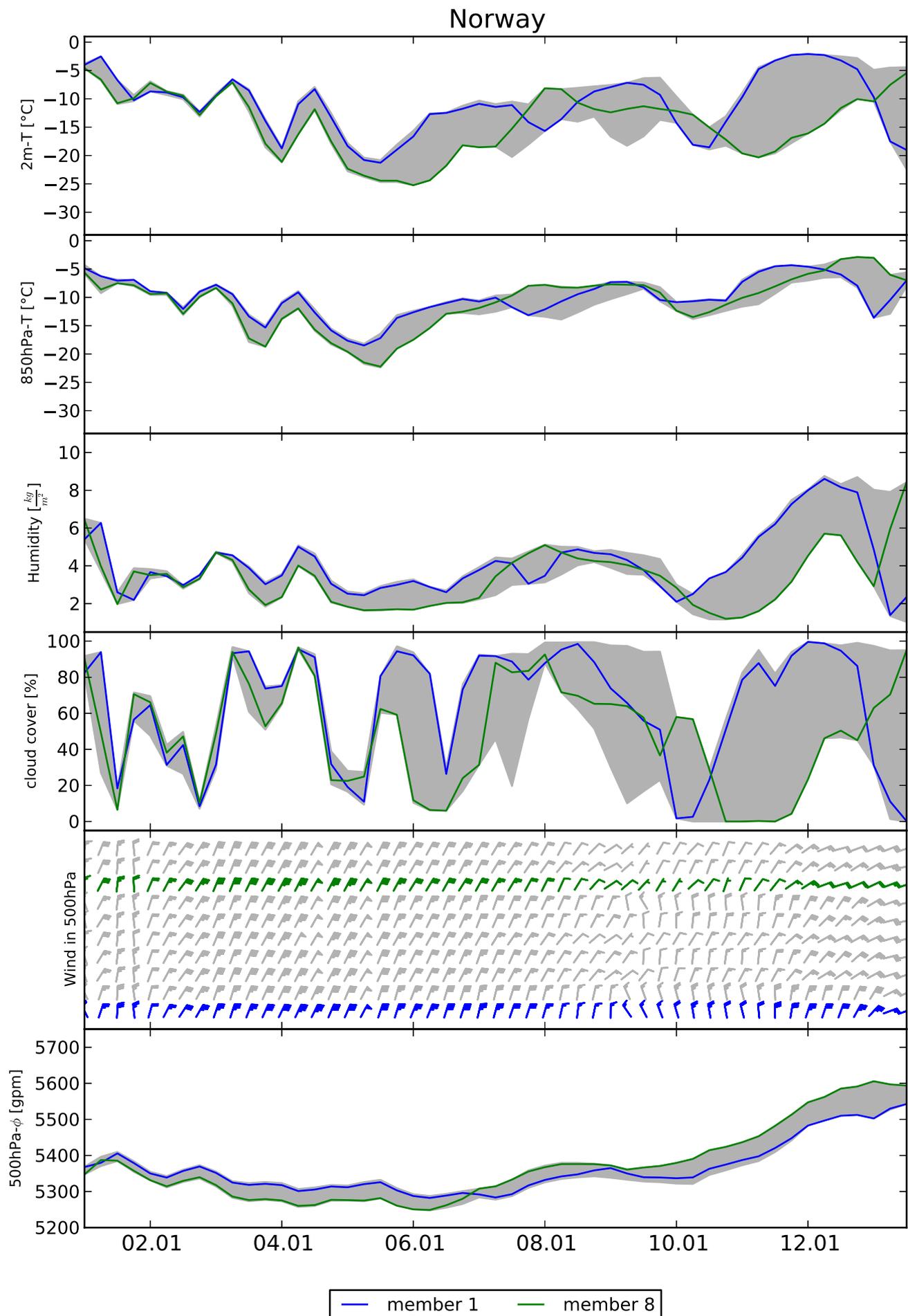
Figure 5.3: Temporal evolution of different parameters over a case study region in Norway (indicated by the black box in Figure A.1). Two different ensemble members are highlighted with blue and green lines. The ensemble spread is indicated by the gray shaded area.
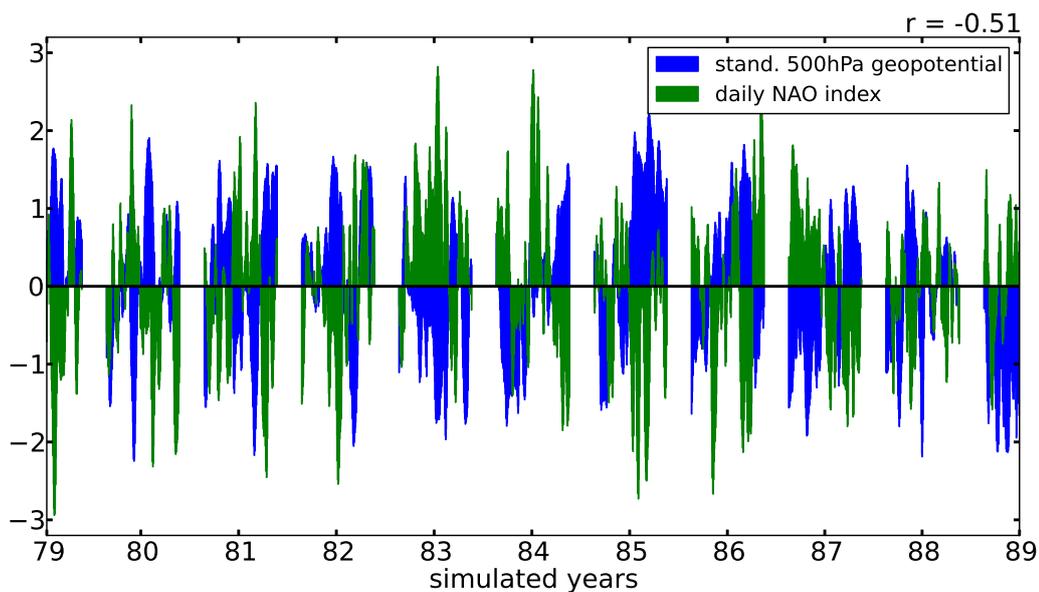
Figure 5.4: Standardized anomalies of 500 hPa-geopotential height internal variability (blue bars) and daily NAO index (green bars) for the extended winter seasons (October-March) of all simulation years. A five day running mean has been applied to the 500 hPa-geopotential height internal variability prior to the standardization to have a comparable smoothing to the daily NAO index. On the upper right the linear correlation of both time series is given.

5.2.2   Internal Variability and the Daily NAO Index

To generalize the analysis to all NAO phases, the daily NAO index introduced in Section 5.1.1 is used and compared to the domain averaged internal variability. A time series of standardized anomalies of the 500 hPa-geopotential height internal variability is computed followed by a five day running mean calculation, to better visualize the correlation to the daily NAO index. The standardization of internal variability is achieved by taking the logarithm of internal variability to get an approximate Gaussian distribution, because the internal variability data follows approximately a log-normal distribution. This is followed by subtracting the temporal mean and dividing by the standard deviation of the distribution.

Figure 5.4 shows the standardized anomalies of the 500 hPa-geopotential height internal variability and the daily NAO index for the extended winter season from October to March. Both time series are negatively correlated for periods of a couple of weeks, e.g., in winters 82/83 and 86/87. Other periods, e.g., in the middle of winter 83/84 show no correlation or even correlations of positive sign. Overall

the Pearson correlation coefficient of both time series is -0.51, which indicates that negative daily NAO is correlated with positive anomalies in internal variability and vice versa. Similar results are obtained with other parameters ranging from correlations of -0.45 for near-surface temperature to -0.48 for mean-sea-level pressure (not shown). This confirms the results from the circulation type analysis (see Chapter 4) that NAO phases are associated with strong and weak phases of internal variability.

Using the definitions for different states of the NAO from Table 5.1, Figure 5.5, depicts the level of domain averaged 500 hPa-geopotential height internal variability. For negative phases of the NAO the median of internal variability is strongly enhanced compared to positive phases. This Indicates that in NAO negative phases the internal variability for 500 hPa-geopotential height is much higher, thus confirming the circulation type analysis results. The same holds for all investigated variables such as mean-sea-level pressure, near-surface temperature and precipitation. Nevertheless, the boxplot also shows a large spread for each NAO phase; especially for the more negative phases.

Some of the high outliers in the neutral and positive range of the NAO phase result from transitions of longer lasting negative NAO phases to a positive phase. In the case of neutral NAO, half of the outliers at the high end come from one event in winter 1984/1985. Here, a phase of strong negative NAO in the beginning of 1985 is followed by a neutral to positive phase (see Figure 5.4). The internal variability of the model stays relatively high. This can be seen as a memory in the system and was already reported by other authors (e.g., Lucas-Picher et al., 2008a; Nikiema and Laprise, 2011). They claim that once internal variability is present, it has to be either dissipated or transported out of the model domain to vanish.

Memory effects, however, are not the only contributing factor to the large spread especially in the negative NAO phases. Negative NAO phases should be more viewed as necessary condition for high internal variability states, but low internal variability phases are still possible. Other factors like *local enhancement* that can increase internal variability drastically, as discussed in case study in Section 5.2.1.
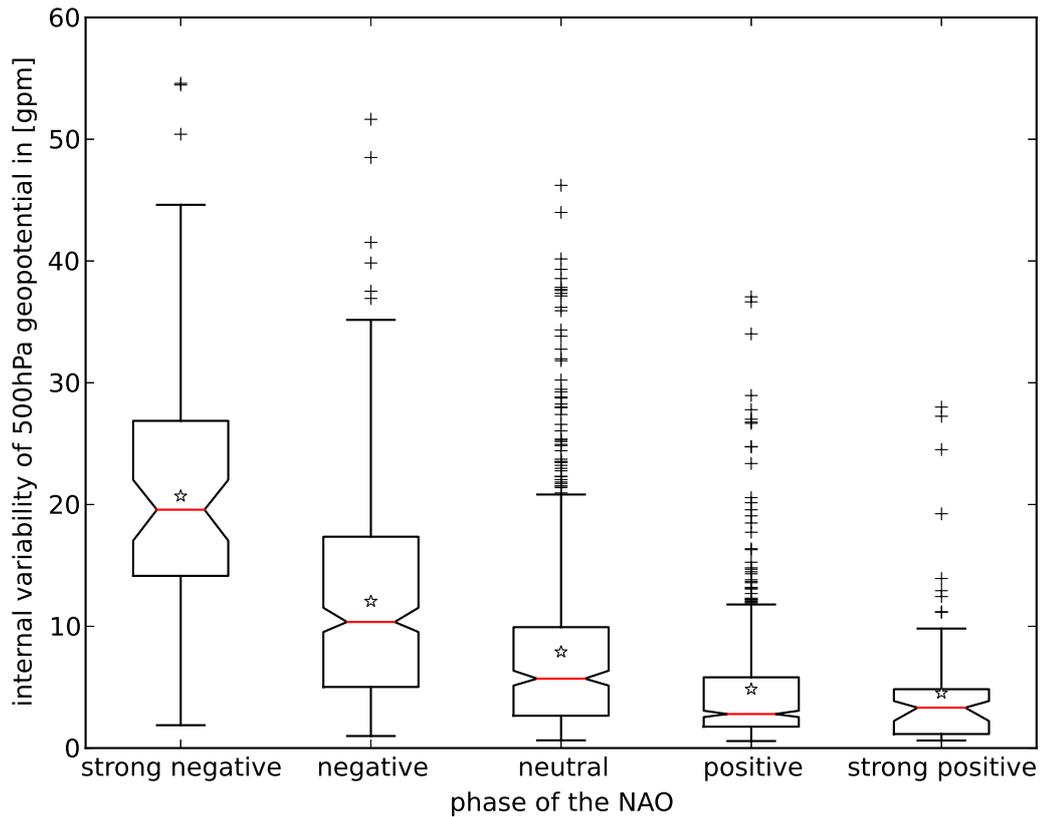
Figure 5.5: Boxplot of the 500 hPa-geopotential height internal variability for different phases of the NAO. Stars mark the mean of each distribution, the read line the median with notches marking the confidence interval using bootstrapping. The box covers the inner quartile range and whiskers are a function of the inner quartile with a maximum length of 1.5 times the inner quartile range. Outliers are marked with fliers.
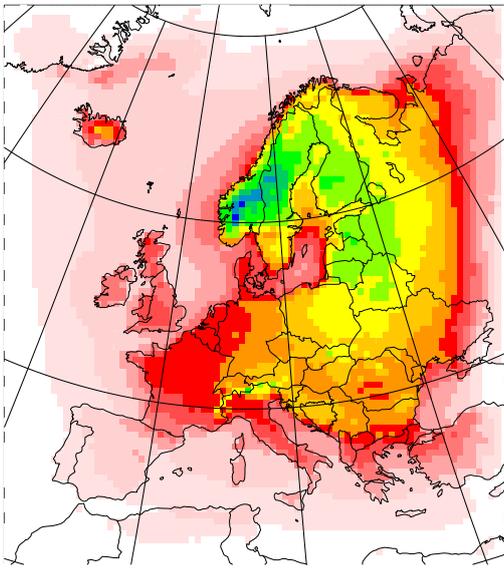
(a) Strong negative
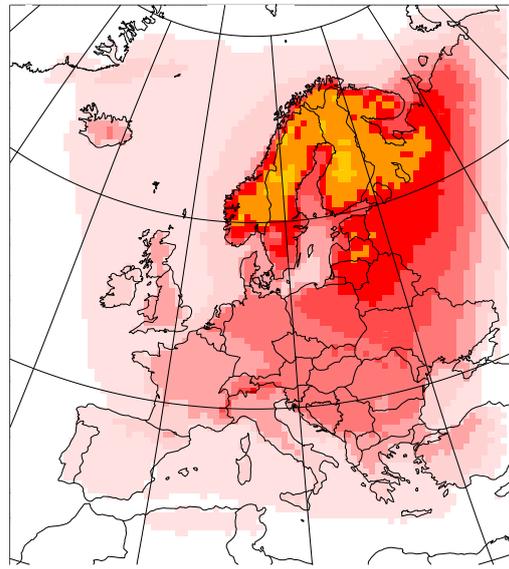
(b) Negative
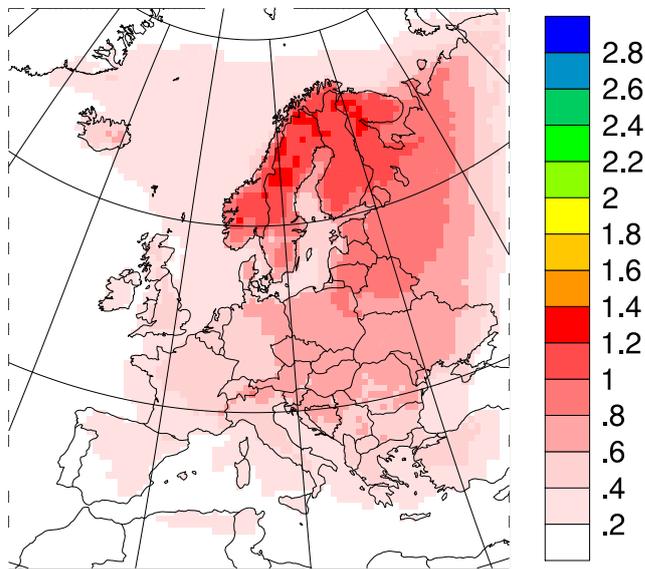
(c) Neutral
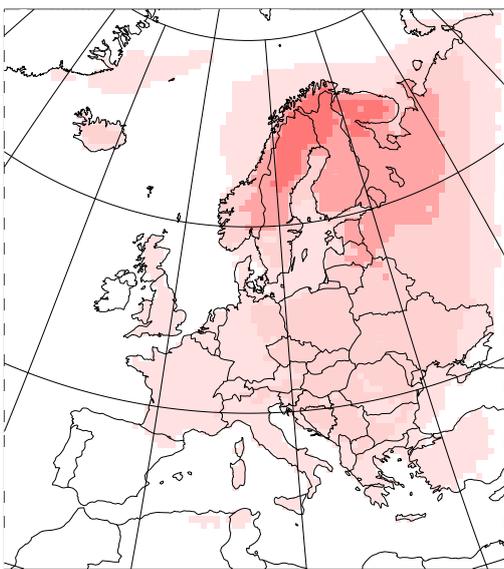
(d) Positive
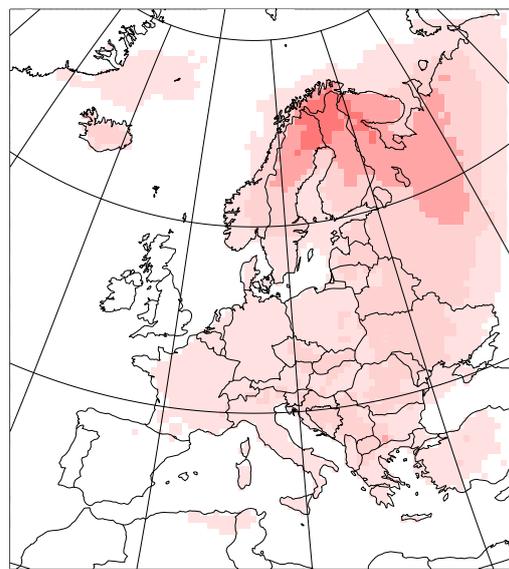
(e) Strong positive

Figure 5.6: Near-surface temperature internal variability in K for different phases of the NAO defined in Table 5.1.

Figure 5.6 shows composites of the spatial patterns of near-surface temperature internal variability for the five classes of the NAO phase. In case of a strong negative NAO phase (Figure 5.6 (a)) the spatial pattern of internal variability shows high values of more than 1 K throughout most of the land points. Over water the internal variability is generally strongly reduced due to the prescribed sea-surface temperature that correlates strongly with the near-surface temperature(see also Section 3.1). Maximum values of around 2.8 K can be found in the Norwegian mountains. Most of the Baltic Sea catchment area shows high levels of internal variability of more than 1.4 K in the South-Western and more than 2 K in the North-Eastern parts. Towards more positive NAO the center of the pattern moves to the North and becomes much weaker. For the strong positive NAO case the internal variability pattern does not exceed values of more than 1 K (Figure 5.6 (e)).

The patterns are very similar to the ones in Figure 4.4 (a) and (b) where the composites of positive/negative NAO-like circulation types show similar results. The differences can be partly explained by the different temporal means considered for the plots. In Figure 4.4 (a) and (b) only a subset (December-February) of the data used for the NAO comparison was used. As internal variability of near-surface temperature is highest from December to February (see Figure 3.2 (b)) it is not surprising that the strength of internal variability is higher in the composites of the NAO-like circulation types. If only the overlapping period is considered, the strong negative NAO case even reaches internal variability values of up to 3.5 K west of the Baltic Sea (not shown).

5.2.3 Diagnosing Internal Variability

The correlation of winter NAO states to the strength of domain averaged internal variability raises the question, whether it is possible to determine the strength of internal variability from the driving fields. As mentioned before, the mechanism leading to strong internal variability in NAO negative states, is mainly the weaker forcing from the predominant westerly flow compared to NAO positive states. This is used, to construct an index based on the strength of the (unrotated) zonal wind in 500 hPa from the driving fields. To filter noise from individual synoptic disturbances, a twenty-day running-mean is applied to the zonal wind data. In the following step, the zonal wind is correlated with the twenty-day running-mean of domain averaged internal variability.

Figure 5.7 shows the Pearson correlation of zonal-wind with the logarithm of domain averaged mean-sea-level pressure internal variability. The logarithm is used because the distribution of domain averaged mean-sea-level pressure internal variability values is closer to a log-normal rather than a normal distribution, thus making the Pearson correlation more meaningful. In Figure 5.7 (a) the entire period used for the daily NAO index is presented, whereas Figure 5.7 (b) only shows the winter season. Both periods show correlations coefficients of more than 0.6 over the Mediterranean Sea. During December to February the correlation even reaches values up to 0.7. The opposite correlation can be found over Scandinavia with negative correlations of less than -0.5 for October to March. If only December to February is considered, a wide band between $50\,°\mathrm{N}$ and $60\,°\mathrm{N}$ tilting to the North after $10\,°\mathrm{W}$ with negative correlations less than -0.6 can be seen.

The correlation pattern relates well to the theory on jet stream regimes (see, e.g., Woollings et al., 2010a, and references therein). Woollings et al. (2010a) found out that the variability of the North-Atlantic eddy-driven jet stream has three preferred latitudinal positions or regimes. Here, the mean-sea-level pressure internal variability shows negative correlation with the northern regime and positive correlation with the southern regime for the winter season. Franzke et al. (2011) show that these regimes are closely related to a negative NAO for the Southern and positive NAO for the Northern regime. This connection allows the usage of the zonal wind to infer on the strength of internal variability inside the domain. The correlations in other seasons are not as good which can be expected based on the results from Chapter 4, where the connection of the internal variability inside the domain to circulation types became weaker in the transition season and was almost absent in summer. This also explains the weaker correlation in the extended winter season (October-March).

This relation of zonal wind in $500\,\mathrm{hPa}$ from the forcing and internal variability inside the domain can now be used to construct an internal variability index to infer on the strength of internal variability from the driving data. Several tests were performed to find the most promising index including different choices in height for the wind data and using only positive or negative correlations. The best performance was achieved by using the difference of zonal wind speeds over the maximum correlation and anti-correlation regions. The regions are indicated in Figure 5.7 by the small black squares. The internal variability index is defined by

(a) October-March   **(b)** December-February
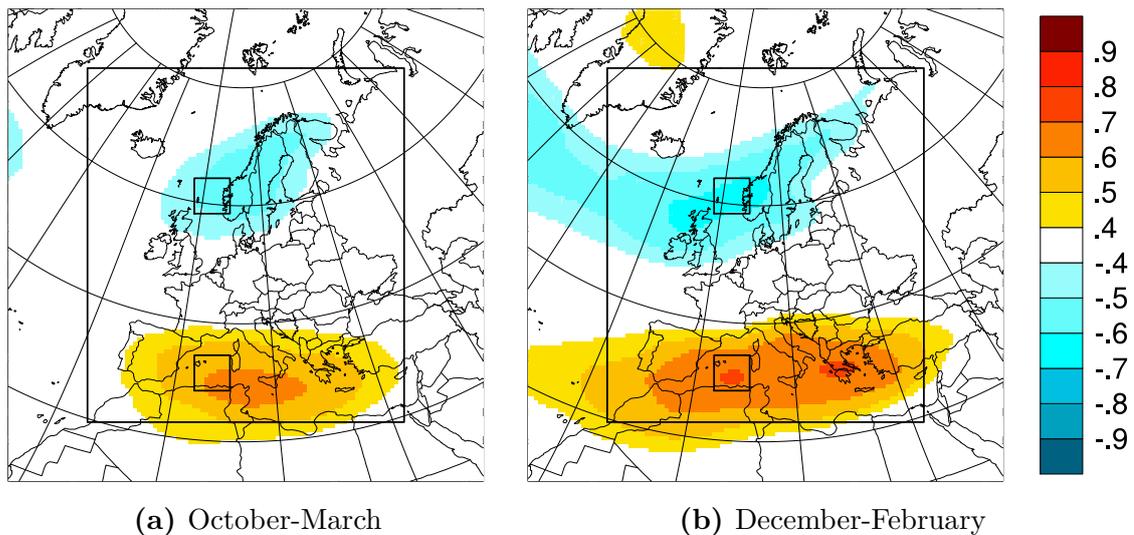
Figure 5.7: Correlation of 500 hPa zonal wind speed and the logarithm of mean-sea-level pressure internal variability. A twenty day running mean has been applied to both parameters.

$$IV_{index} = \frac{\{u_{maxcorr}\} - \{u_{mincorr}\}}{u_{max}} \qquad (5.1)$$

where $\{u_{maxcorr}\}$ is the box mean zonal wind speed of the maximum correlation square and $\{u_{mincorr}\}$ the box mean zonal wind speed of the minimum correlation square. The parameter u_{max} is used for normalization and is set to $30\,\mathrm{m\,s^{-1}}$.

Figure 5.8 shows the internal variability index in relation to the logarithm of mean-sea-level pressure internal variability. For both seasons a positive correlation of the internal variability index with the strength of internal variability is seen. As expected from Figure 5.7, the correlation is better for the meteorological winter season from December to February with a correlation coefficient of 0.7. For the extended season from October to March the correlation coefficient drops down to 0.61, which is once again related to the weaker connection of domain averaged internal variability to circulation types in the transition seasons. The internal variability index varies between -1 to 1, where negative values usually mean a less than average internal variability and positive values correspond to higher than average internal variability. A multiple linear regression with using both box means as covariates was also tested, but did not yield better results (not shown).
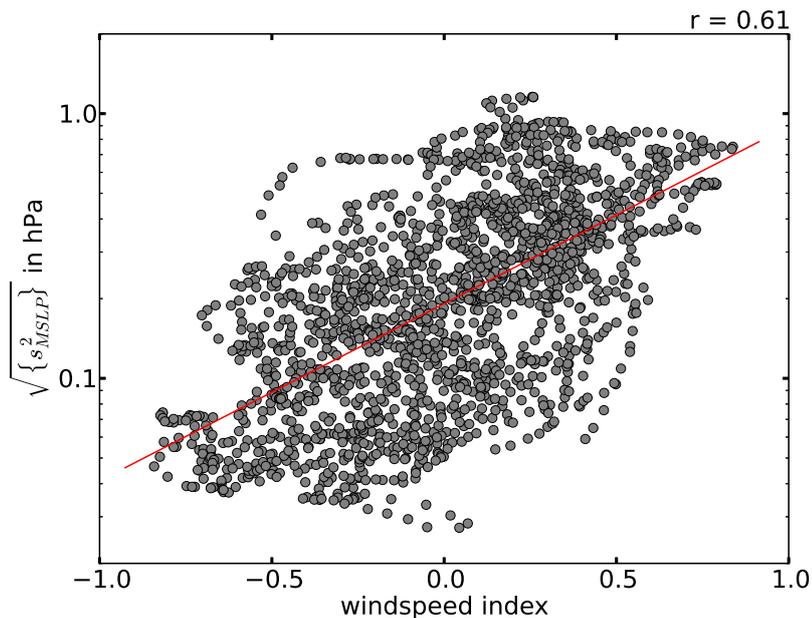
(a) October-March
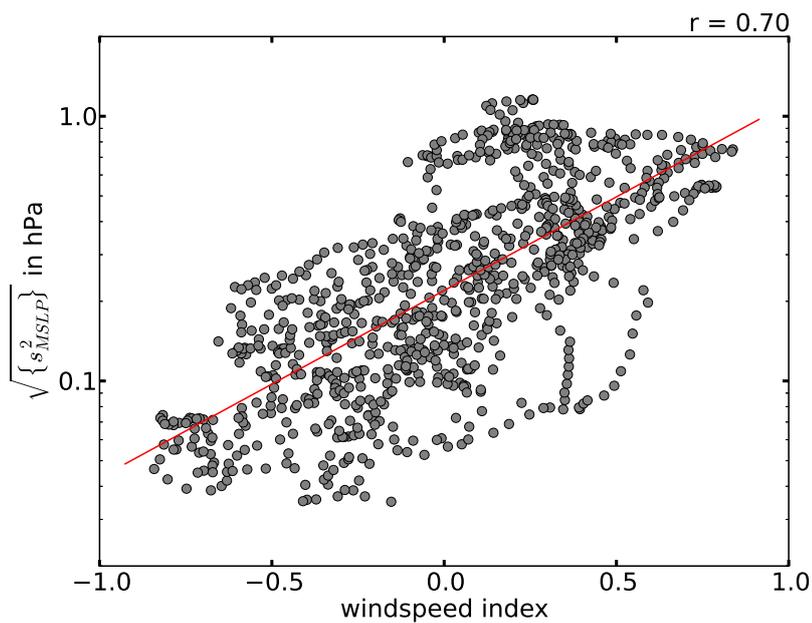
(b) December-February

Figure 5.8: Scatter plot of wind speed index calculated from the boundary forcing data against the domain averaged square root of mean-sea-level pressure internal variability for two seasons of the entire simulation period from 1979 to 1988. The red line indicates the best fit of a linear regression with the Pearson correlation coefficient given on the top right.

5.3 Conclusions

Focusing on a specific case of a strong internal variability episode during a strongly negative NAO phase it shows that deviations in the large scale flow between two ensemble members can be locally enhanced by strong internal variability in the energy budget at the surface due to cloud cover internal variability. This process is particularly effective when the area is snow covered and can explain parts of the large spread in internal variability associated with the circulation types discussed in Chapter 4. Furthermore, it has been shown that there is a connection between winter NAO and the internal variability of a regional climate model over Europe. Using a daily NAO-index for the extended winter season October to March shows that positive NAO phases reduce the internal variability inside the domain and negative NAO phases result in increased internal variability, thus confirming results from the circulation type classification found in the previous Chapter 4. For the first time, it has been demonstrated, how to infer from the driving data onto the strength of the internal variability inside the domain. This is achieved by constructing an internal variability index based on the unrotated zonal wind speed in 500 hPa. It should now be possible, to use this index to determine the strength of internal variability in winter for other decades in the ERA-40 period without running the full ten member ensemble. There are some limitations to the usage, though: First, the derived internal variability values can only be used for the exact same domain and resolution. Changing the domain size and/or location would lead to a different behavior in internal variability. Second, it is very likely that the exact numbers only hold for REMO. A qualitative estimate though should also work for other models using the same domain, assuming that the connection between forcing strength and the internal variability of the model is fundamental.

Chapter 6

Conclusions

A ten member ensemble of the regional climate model REMO has been used to investigate internal variability in terms of the ensemble standard deviation over a European domain. The ensemble has been initialized with a one day lag and forced with the same lateral boundary forcing during the entire integration. To the authors best knowledge, it is the first systematic study of internal variability in a regional climate model over Europe, which is needed in order to judge on the significance of regional climate information. In this study, three research questions presented in Chapter 1 are answered.

- *How does internal variability change with season over Europe?*

It is shown that internal variability over a European domain is similar to other locations in the mid-latitudes. Typical is the episodic nature of internal variability with strong and weak phases in the temporal evolution. Even after several years of integration these phases are present. During the four meteorological seasons similarities, but also important differences to earlier studies for other locations on the globe has been found. In summer, the internal variability is typically large with low temporal variability as shown by other studies, e.g., Giorgi and Bi (2000); Caya and Biner (2004). Similarly, autumn shows expected results with roughly half the internal variability in mean-sea-level pressure and near-surface temperature and less than a third in precipitation compared to summer. Winter and spring in the present study differ more from previous findings. The internal variability in mean-sea-level pressure and near-surface temperature for these two seasons is on average slightly stronger compared to summer, but shows a much stronger temporal and inter-annual

variability. Only in Lucas-Picher et al. (2008b) a similar seasonal behavior has been reported. They explained the differences to earlier studies (e.g. Giorgi and Bi, 2000; Caya and Biner, 2004) by their substantially larger domain size. In the present study, the domain size is comparable to Giorgi and Bi (2000), but has yearly cycles similar to Lucas-Picher et al. (2008b). In a follow-up study, Lucas-Picher et al. (2008a) found that internal variability is larger if the residence time of air-parcels inside the domain is longer. Laprise et al. (2012) concluded from this finding that internal variability inside a regional climate model domain is connected to the strength of the lateral boundary forcing. This hypothesis has been adopted and leads to the second research question:

- *How do weather regimes influence the internal variability of a regional climate model throughout different seasons?*

A deeper analysis of the weather regimes in the lateral boundary forcing and its connection to the internal variability has been performed using the SANDRA circulation type classification. For the first time such a comprehensive circulation type classification has been used to investigate internal variability of a regional climate model. Results suggest that NAO positive and negative like circulation types are linked to the strength of internal variability inside the domain during winter. Summer circulation types only marginally modulate the internal variability and thus the main origin of internal variability in summer are most likely local processes such as local scale variations in convection, and condensation between members of the ensemble as shown in a case study by Nikiema and Laprise (2011). The transition seasons spring and autumn have a mixed behavior, but significant differences in the strength of internal variability for NAO-like circulation types have been found.

As NAO phases play an important role for the strength of internal variability, a daily NAO index has been used to investigate the connection between NAO and internal variability inside the model domain during the extended winter season from October to March. Results have confirmed the findings of the circulation type classification that strong negative NAO phases show the strongest internal variability, whereas strong positive NAO phases coincide with weak internal variability. This can be explained by looking at the physical processes connected to the state of the NAO. One important feature is the strength of the eddy-driven jet stream. In NAO positive phases the meridional pressure gradient between Iceland and the Azores is enhanced leading to a stronger jet and thus stronger forcing from the boundary conditions.

In NAO negative phases the pressure gradient is weakened resulting in a weaker forcing.

The strong variability in the strength of internal variability during NAO negative phases suggests that NAO negative phases are a necessary condition for strong internal variability in winter, but that the reverse argument does not hold. This means that NAO negative phases provide the right environment for strong internal variability to occur, but other processes are needed for a growth. A case study on a strong internal variability event showed that internal variability takes time to develop. It also showed that local processes such as differences in the radiative cloud forcing and small spatial deviations of fronts between the members of the ensemble, can lead to rapid growth of internal variability. The latter finding is in good agreement with Diaconescu et al. (2012) who showed that hydrodynamic instabilities associated with baroclinic processes play an important role in the growth of internal variability. To explore the potential of the connection between internal variability and the lateral boundary forcing the final question of this study is:

- *Is it possible to determine the strength of internal variability from the variability of the boundary data?*

Based on the connection between the state of the NAO and therefore between the strength of the jet across the domain and internal variability in winter, an internal variability index has been constructed using the zonal wind speed in 500 hPa. The index shows high significant positive correlation with the internal variability inside the domain for the extended winter season from October to March. The correlation is even better if only December to February is considered. With this it has been shown for the first time that it is possible to determine the strength of the internal variability in a regional climate model from the variability in the lateral boundary forcing.

The index is of importance for model development, because it makes it possible to judge on the significance of model result differences during sensitivity studies in winter. It could also be useful for the downscaling of monthly or seasonal forecasts. If low index values are derived from the forcing additional uncertainty from the regional climate models internal variability could be neglected.

After summing up the most important results of the present study, it is important to state that the usage of the internal variability index underlies certain limitations.

The index is only valid for the winter half-year from October to March and shows best performance from December to February. So far, it has not been validated for other lateral boundary forcings and/or other periods such as the end of the 21$^{\text{st}}$ century in climate change predictions. There is evidence from modeling studies that the occurrence of circulation types might change in a changing climate. Demuzere et al. (2009) found that towards the end of the 21$^{\text{st}}$ century western and anticyclonic circulation types increase significantly under an A1B scenario for the extended winter season from October to April. On the one hand, this would mean that internal variability in the model for winter would decrease. On the other hand Demuzere et al. (2009) state that their model showed an overall overestimation in western circulation types during the control period and that further modeling studies are needed to gain more robustness in their results. Nevertheless, Donat et al. (2010) could find changes in the same direction, namely an increase of westerly flow under an A1B scenario using an ensemble of general circulation models. Likewise, Woollings et al. (2010b) found in a doubled CO_2 experiment that NAO positive phases are increasing, but deficiencies in modeling a correct NAO in the control run lower confidence in this finding.

It should be in principle possible to transfer the results from the present study to slightly larger and higher resolved domains such as MiKlip or EUROCORDEX. The strength of internal variability would grow with a larger domain as shown by Alexandru et al. (2007), but the timing of strong and weak phases in winter should be similar. If the assumed relationship holds, it is possible to get an estimate for the internal variability from a much cheaper model configuration regarding computing time, thus allowing to get an qualitative assumption on the internal variability of the higher resolved domain without running an entire ensemble.

Internal variability of a regional model can be largely reduced when the large scales of the regional model are forced to the solutions of the driving model. Techniques such as spectral nudging are an option to achieve that. The problem of forcing the large scales is that it influences meso-scale circulations generated by the model to a large extend – potentially suppressing circulations that are, e.g., not resolved by the large scale forcing due to insufficient resolution. It is still under debate if deviations of regional climate models from the large-scale flow in the forcing are due to errors in the forcing or the regional model itself (Laprise et al., 2008). If on the one hand the errors are due to the driving model there is even potential to correct for it in the regional model. If on the other hand the regional model deteriorates the large scale, a forcing of the large scales is preferable.

The internal variability of the climate on the investigated domain is rather small for most variables after one season and does not play a role after one year. This means that internal variability of a regional climate model is small compared to other sources of uncertainty such as scenario uncertainty. As mentioned above, internal variability grows with the model domain and internal variability of the climate can be important on very large domains used by Lucas-Picher et al. (2008b) at least on the time scale of a decade. For some variables such as precipitation on the catchment scale, the internal variability of the regional climate model plays an important role in the uncertainty of the climate change signal. This has been recently shown by Braun et al. (2012) for the North-East of Canada. For Europe internal variability seems to be even more important, because it is already quite large in the comparably small domain used in this study. On bigger domains with more grid points and higher resolution (e.g., the domains used in MiKlip or EUROCORDEX), the level of internal variability is expected to be larger and internal variability of the climate may play a role on a European domain at least on decadal time scales.

Appendix A

Daily Charts for the Case study on a Strong Internal Variability Event

An extreme case of an internal variability event is presented. Shown are instantaneous weather charts for each day at 6 h from January 1 to 12, 1985. At the top of each panel, the driving fields from the interpolated ERA-40 data are depicted. Colored contour shades represent mean-sea-level pressure in hPa and contour lines the 500 hPa-geopotential height in gpm. In the center, the same charts from two selected members of the REMO ensemble are shown, which show large differences during this event. At the bottom of each panel, the internal variability of mean-sea-level pressure MSLP and near-surface temperature NST for the entire ensemble is depicted.

Figure A.2 shows instantaneous maps from January 1, 1985. In Figure A.2 (a) the forcing ERA-40 data is shown (cut to the model domain). Shades depict the mean-sea-level pressure and contour lines the 500 hPa geopotential height. Figure A.2 (b) and (c) show the same for two different members of the ten member ensemble. Figure A.2 (d) and (e) depict the internal variability of mean-sea-level pressure and near-surface temperature, respectively. The synoptic situation in the ERA-40 data is a high pressure ridge stretching from the Iberian peninsula to the Arctic. A low pressure system is located over northern Russia. In addition, a small low pressure system is found over the German Bight.

Both REMO ensemble members show some deviations from the driving fields, but quite good agreement amongst one another. The ridge is simulated stronger in both members compared to the driving field. The low pressure system over the German

Bight is missing because it is simulated further to the East and already started to merge with the low pressure over Russia in both simulations. Most of the ensemble members show a similar behavior so that the internal variability is low.

From the 1st to the 3rd of January the weather situation does not change drastically. The high pressure ridge on the Western boundary stays pretty stationary, but looses strength. The low pressure system moves southward and a high pressure system form Siberia starts to move into the North-East corner of the domain. In the charts of January 4 it is shown that the high pressure system moved to the Norwegian Sea, whereas the low pressure system from Russia moved south to Italy (Figure A.5 (a)). Low pressure over the southern North Atlantic results in an omega shaped flow pattern.

The main features are captured by the REMO ensemble, but towards the outflow boundary the pattern deviates more strongly compared to the days before. One common feature is that both members do not simulate the low pressure system over Italy. Instead, in member 1 ensemble the system moved to East Belarus (Figure A.5 (b)). For member 8 the system split into two cores with lower pressure and centers over West Belarus and West Russia (Figure A.5 (c)). This is also expressed in the internal variability of mean-sea-level pressure in Figure A.5 (d).

For near-surface temperature internal variability Figure A.5 (e) shows that the differences between ensemble members are concentrated in a narrow band along the Russian Belarus border with near-surface temperature internal variability of up to 7 K. The strongest near-surface temperature internal variability is not exactly found in the same point as mean-sea-level pressure internal variability as already seen in the mean fields in Section 3.2, but increases consistently in the same vicinity. It is caused by the difference in location of a front.

Figure A.1 shows the fronts of the two members using the Thermal Front Parameter (TFP). The TFP is commonly used to detect fronts in, e.g., analysis of daily weather charts. Here, it is calculated from the 850 hPa to 1000 hPa thickness. It can be seen that both members show a front in Belarus, but in slightly different locations. This causes the an area of near-surface temperature internal variability. This result is consistent with a case study by Diaconescu et al. (2012) who found that a large part of the rapid growth in internal variability is explained by baroclinic conversion.

On January 5 and 6, 1985 the high pressure over Iceland intensifies (Figure A.6 (a) through Figure A.7 (a)) which is also simulated by the two example members (Fig-

(a) Member 1   **(b)** Member 8
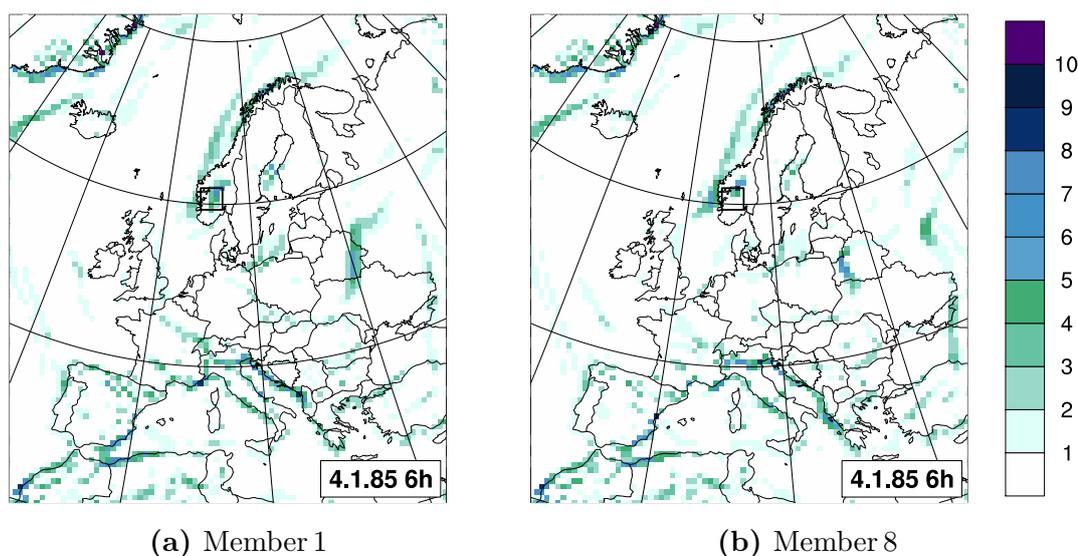
Figure A.1: Thermal front parameter calculated from the 850 hPa to 1000 hPa thickness for January 4, 1985 at 6 UTC and two ensemble members. The black box in each figure indicates the area used for the investigation of local parameters used in Figure 5.3.

ure A.6 (b)–(c) through Figure A.7 (b)–(c)). This system acts as a block and lets the pockets of internal variability develop further (Figure A.6 (d)-(e) through Figure A.7 (d)–(e)), as there is no strong constrain for the development of the low pressure system south of the Baltic Sea. From January 7 to 9, 1985 the blocking high weakens again and forms a ridge again than a separated high over Iceland. The deviations of the members grows even larger, where member 8 resembles the forcing data more accurate than member 1.

From January 10 to 12, 1985 the ridge moves to the British Isles. Thus still blocking the flow and leading to a peak in internal variability during this episode. The REMO ensemble shows different flows inside the domain (Figure A.12). Noteworthy is that member 1 (Figure A.12 (b)) now shows a more consistent pattern with the ERA-40 forcing (Figure A.12 (a)). In member 1 and the forcing a high pressure system is located over the British Isles. Low pressure is sitting east of the Baltic Sea, but is stronger simulated in REMO member 1. For member 8 (Figure A.12 (c)) the situation is different. Here, the low pressure system is found more to the south forming a cut-off low with two minimums over Belarus and Italy at sea-level height. In this realization, the high pressure is weaker and more moved to the north. This results in near-surface temperature internal variability to become quite large (Figure A.12 (d)). Almost entire continental Europe has internal variability values with 1 K and larger. Especially in regions where slight changes in wind direction cause

the advection of quite different air masses internal variability can grow large. This is particularly the case at the Norwegian coast. In other parts it is more difficult to disentangle where internal variability is coming from, because of the moving pockets of internal variability.
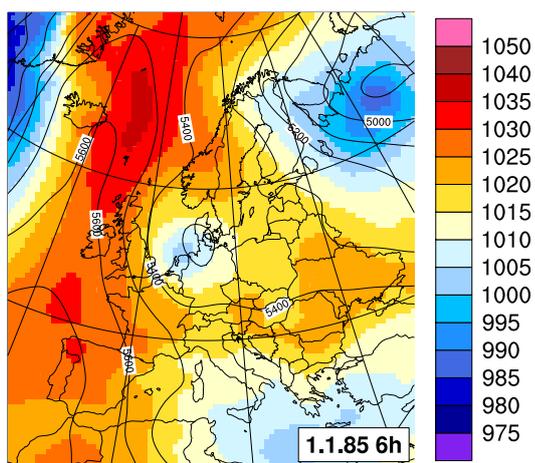
(a) Forcing
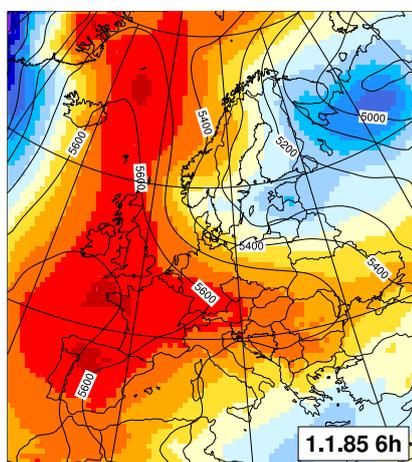
(b) Member 1
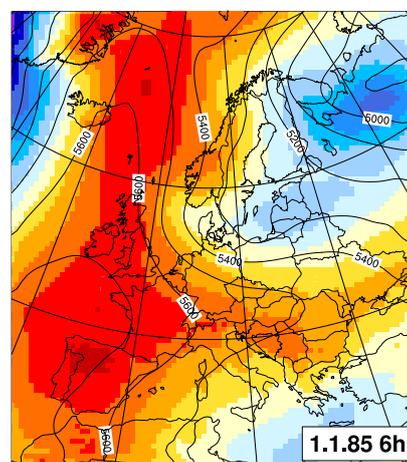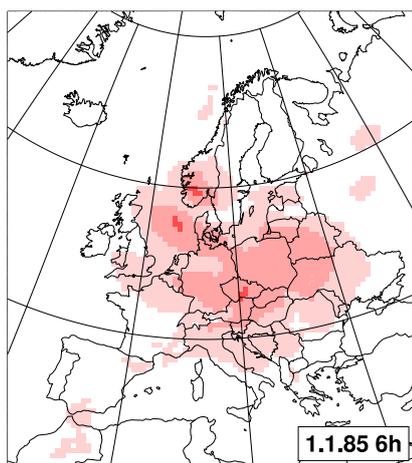
(c) Member 8

(d) MSLP internal variability (hPa)
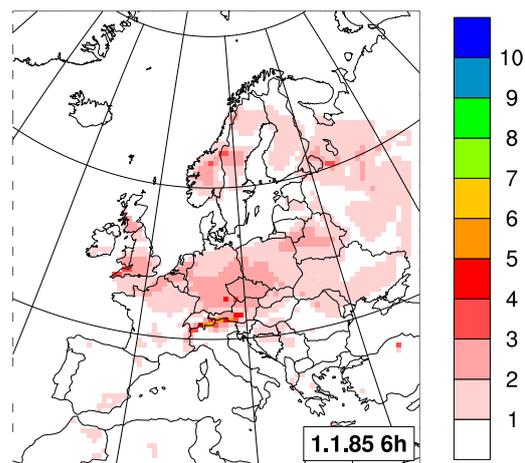
(e) NST internal variability (K)

**Figure A.2:** Case study 1.1.1985.
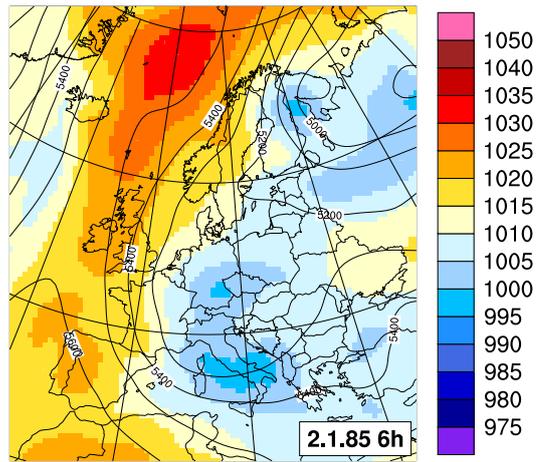
(a) Forcing
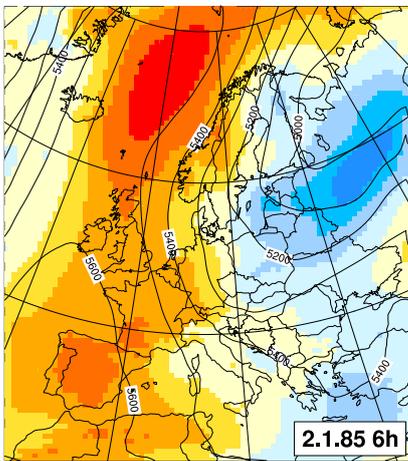
(b) Member 1
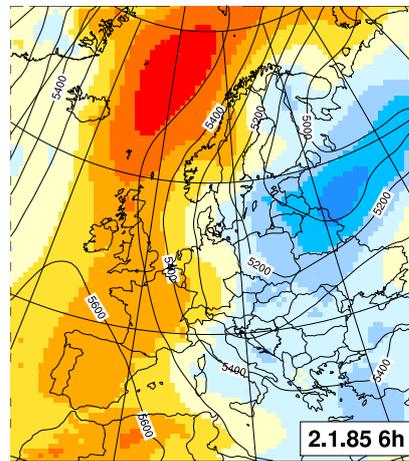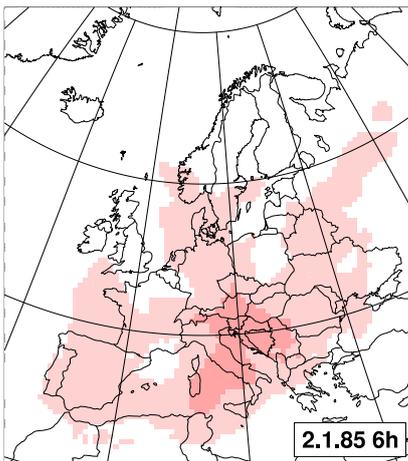
(c) Member 8

(d) MSLP internal variability (hPa)
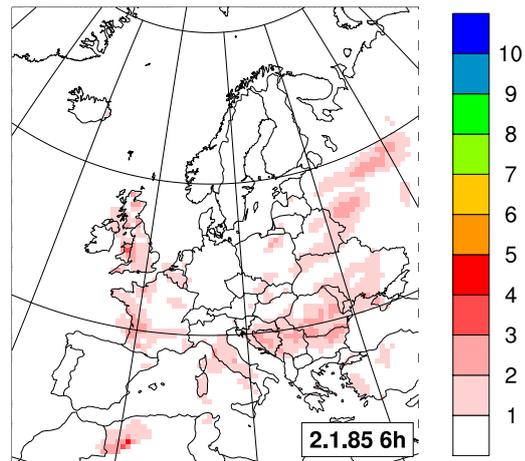
(e) NST internal variability (K)

Figure A.3: Case study 2.1.1985.
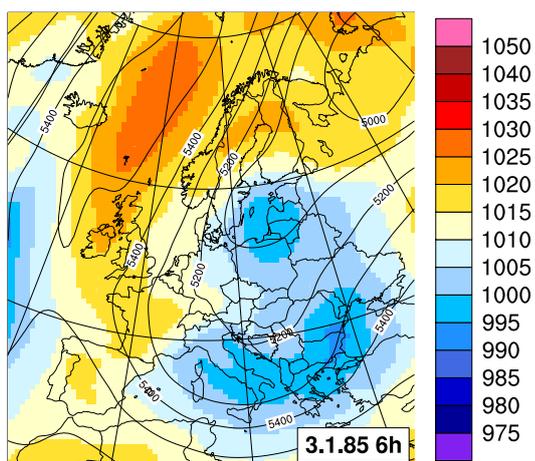
(a) Forcing
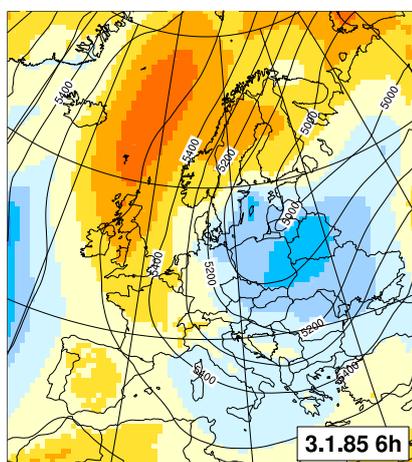
(b) Member 1
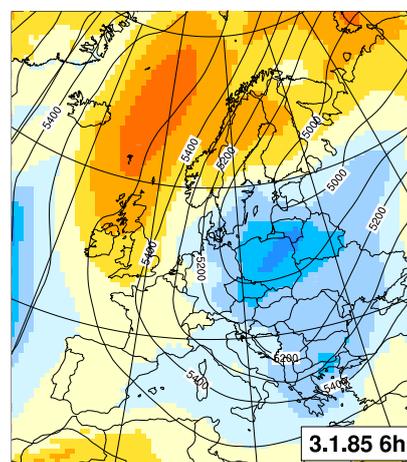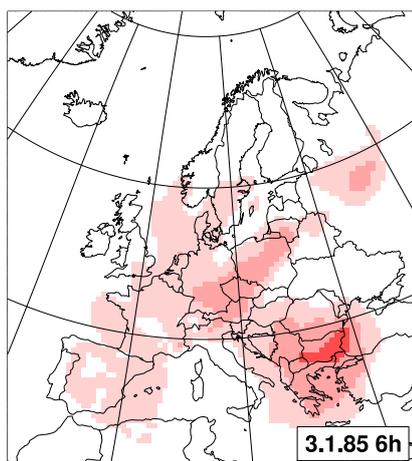
(c) Member 8

(d) MSLP internal variability (hPa)
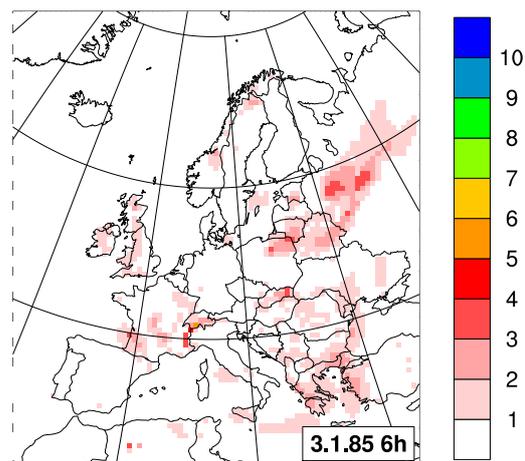
(e) NST internal variability (K)

Figure A.4: Case study 3.1.1985.
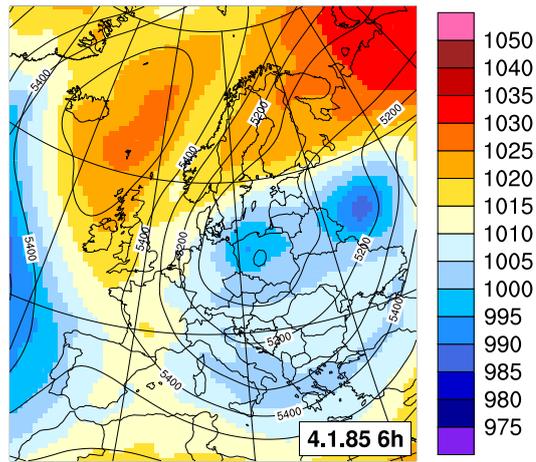
(a) Forcing
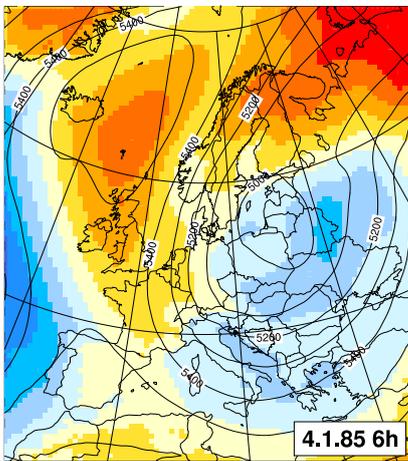
(b) Member 1
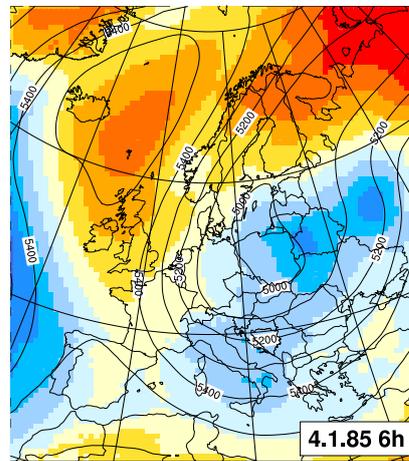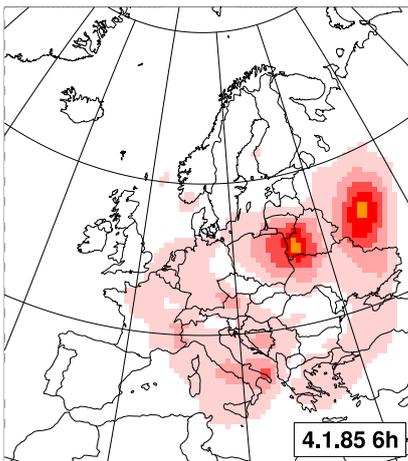
(c) Member 8

(d) MSLP internal variability (hPa)
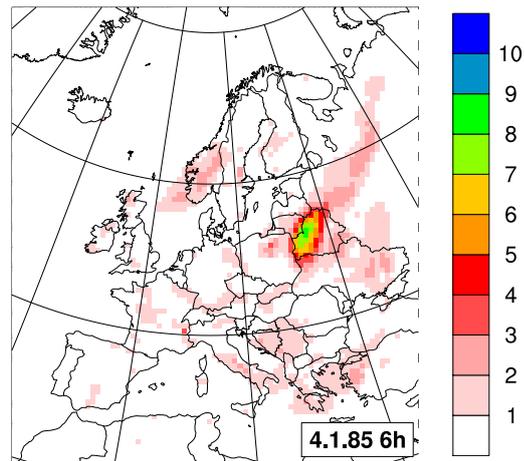
(e) NST internal variability (K)

Figure A.5: Case study 4.1.1985.
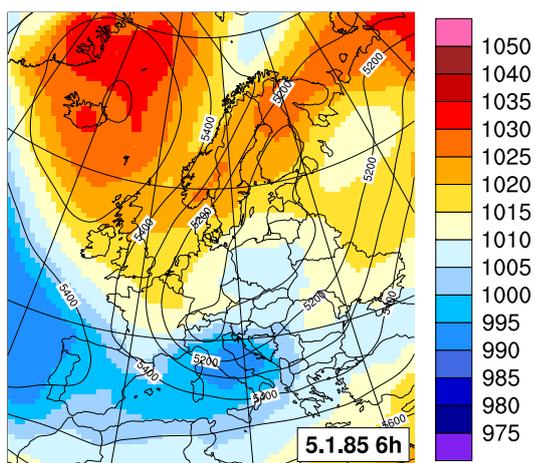
(a) Forcing
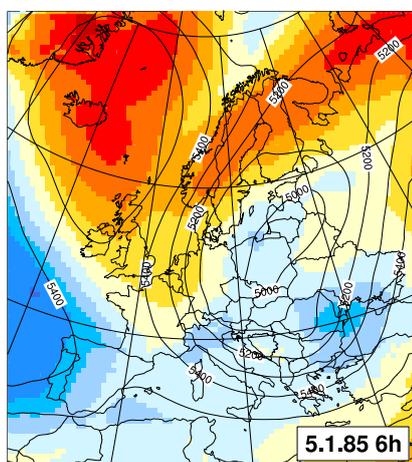
(b) Member 1
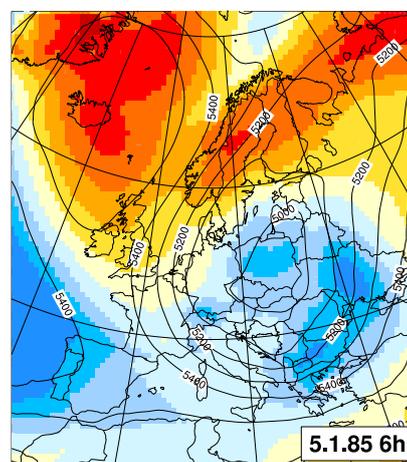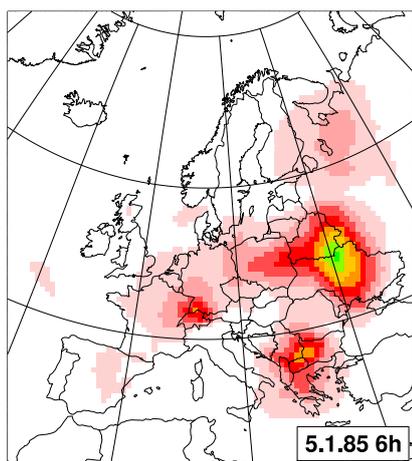

(c) Member 8

(d) MSLP internal variability (hPa)
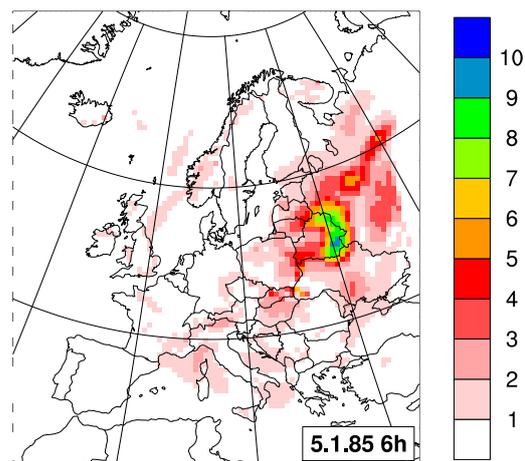
(e) NST internal variability (K)

Figure A.6: Case study 5.1.1985.
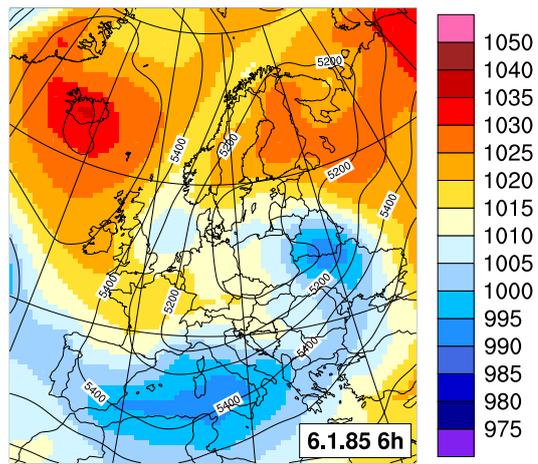
(a) Forcing
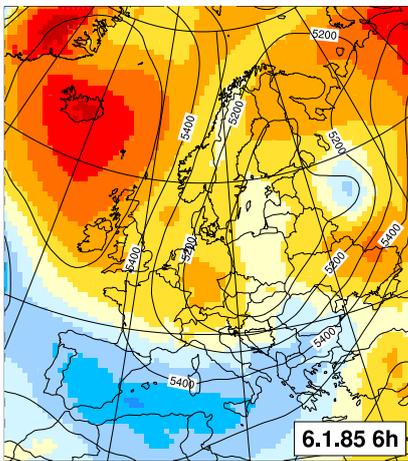
(b) Member 1
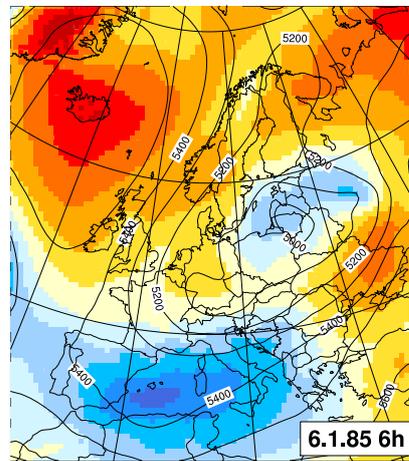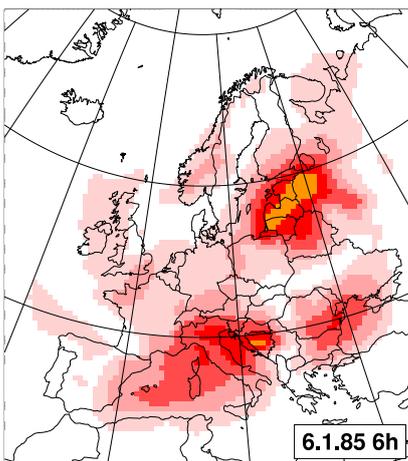
(c) Member 8

(d) MSLP internal variability (hPa)
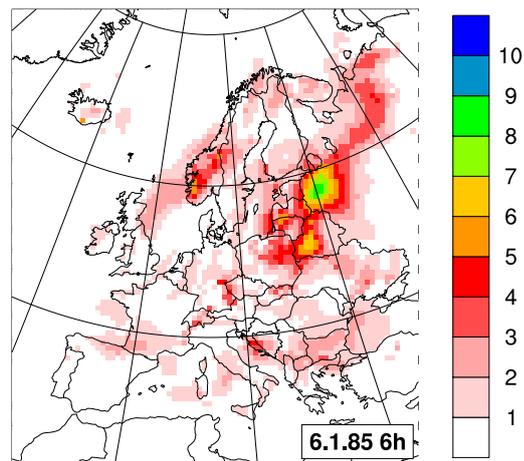
(e) NST internal variability (K)

Figure A.7: Case study 6.1.1985.
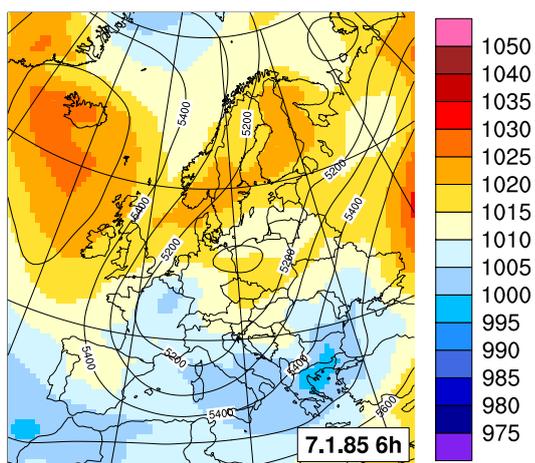
(a) Forcing
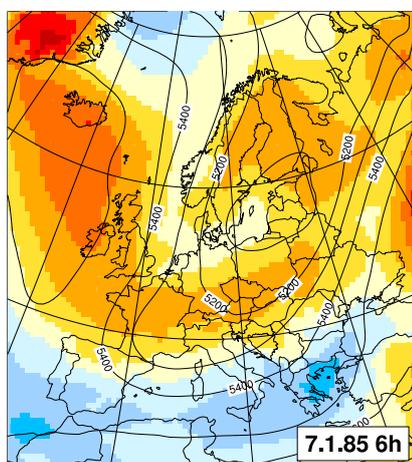
(b) Member 1
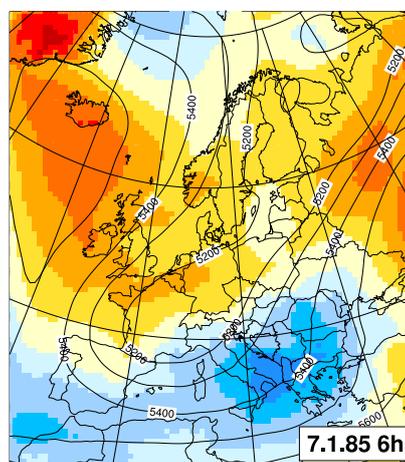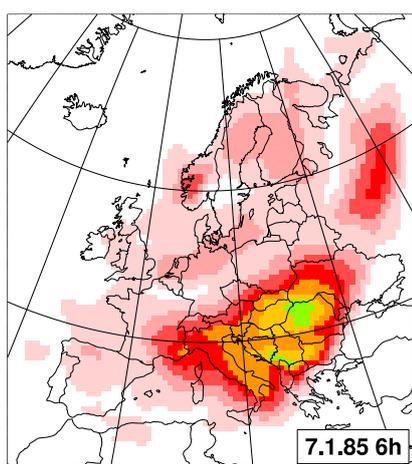
(c) Member 8

(d) MSLP internal variability (hPa)
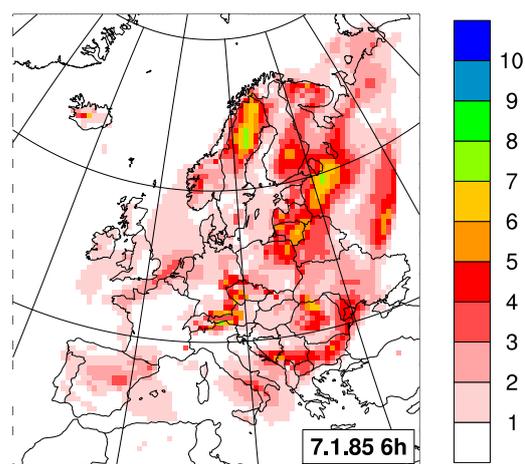
(e) NST internal variability (K)

Figure A.8: Case study 7.1.1985.
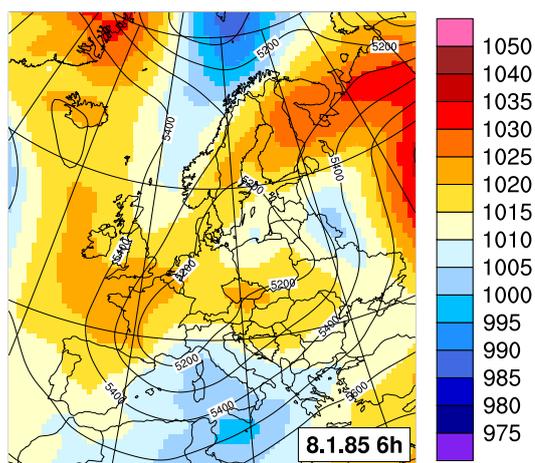
(a) Forcing
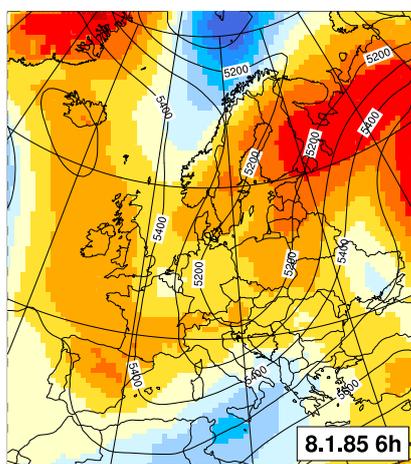
(b) Member 1
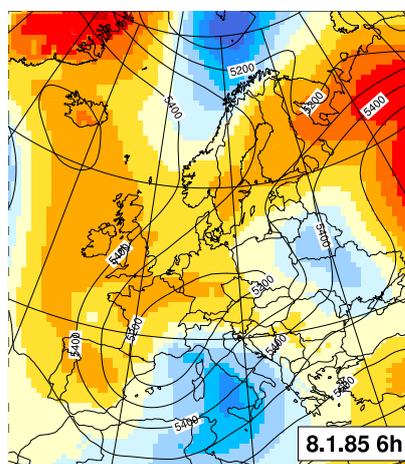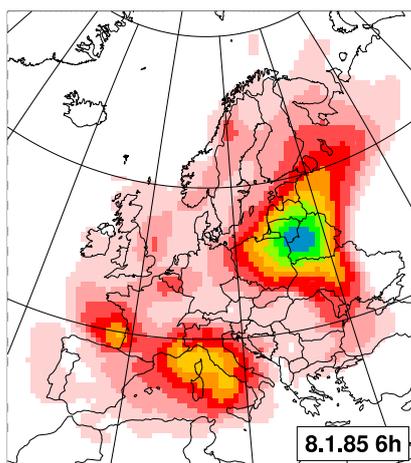
(c) Member 8

(d) MSLP internal variability (hPa)
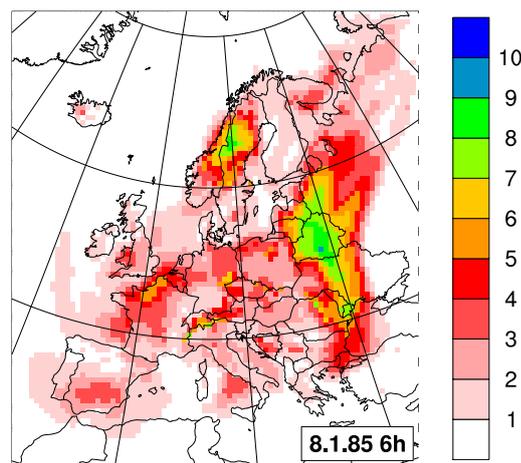
(e) NST internal variability (K)

Figure A.9: Case study 8.1.1985.
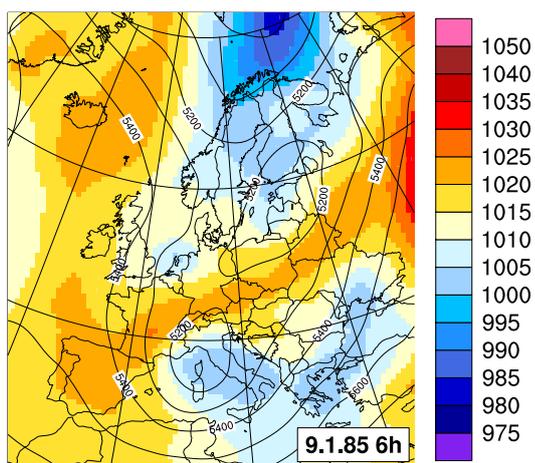
(a) Forcing
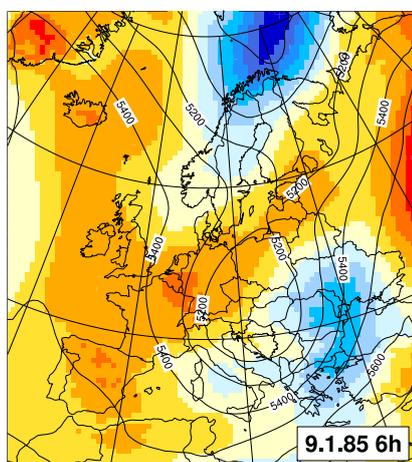
(b) Member 1
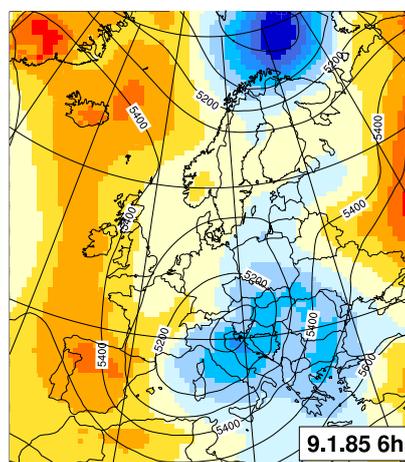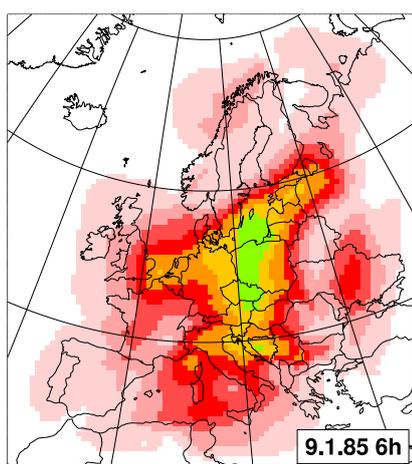
(c) Member 8

(d) MSLP internal variability (hPa)
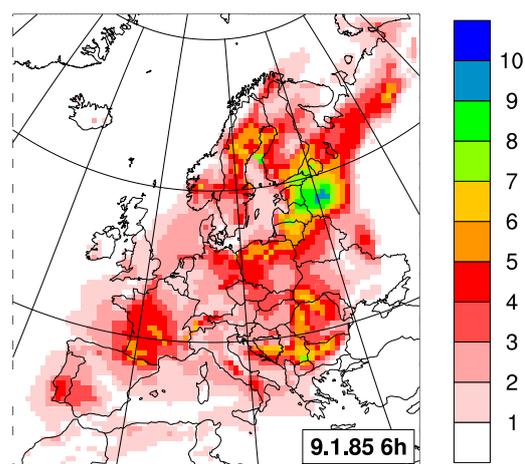

(e) NST internal variability (K)

**Figure A.10:** Case study 9.1.1985.
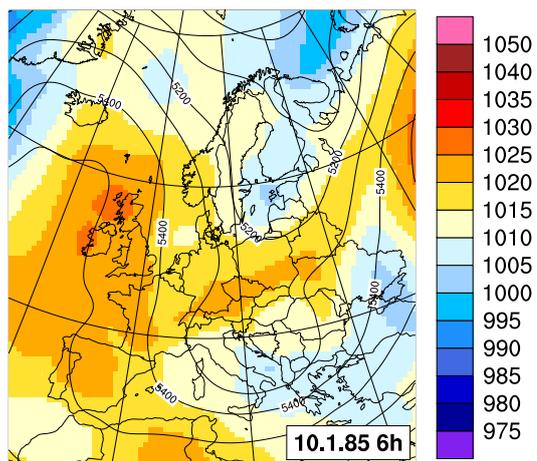
(a) Forcing
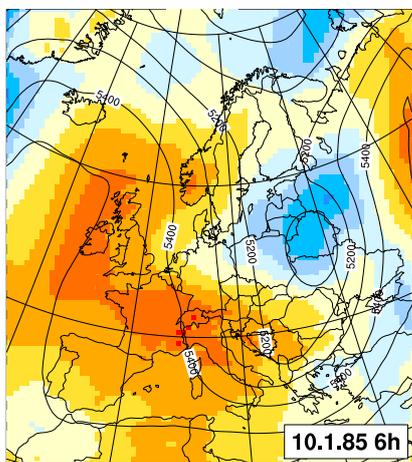
(b) Member 1
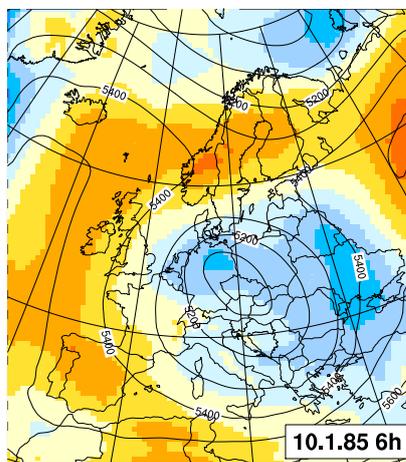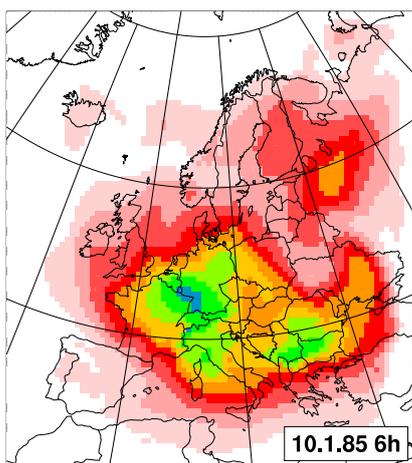
(c) Member 8

(d) MSLP internal variability (hPa)
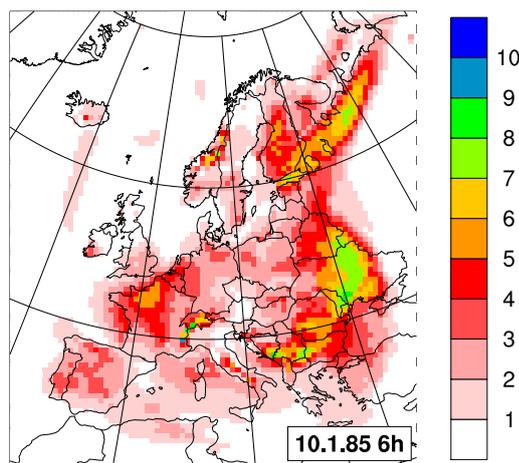
(e) NST internal variability (K)

Figure A.11: Case study 10.1.1985.
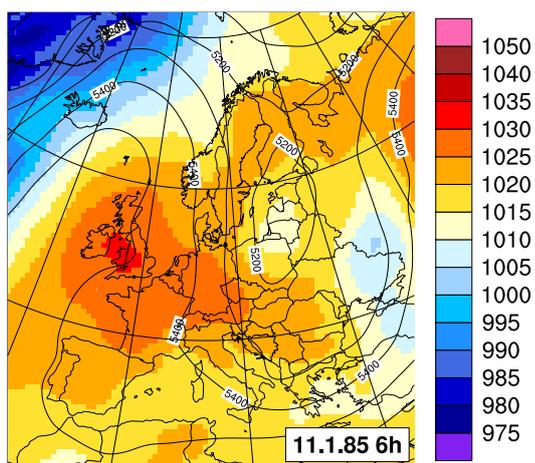
(a) Forcing
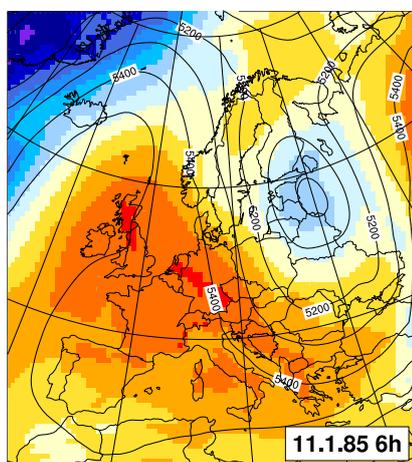
(b) Member 1
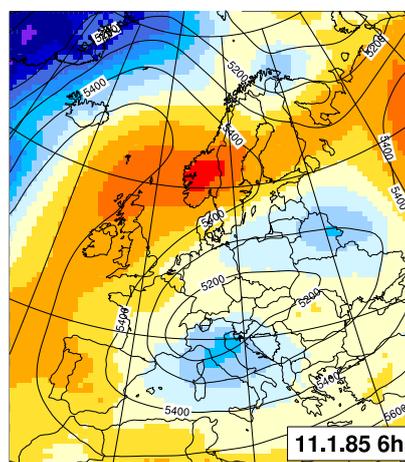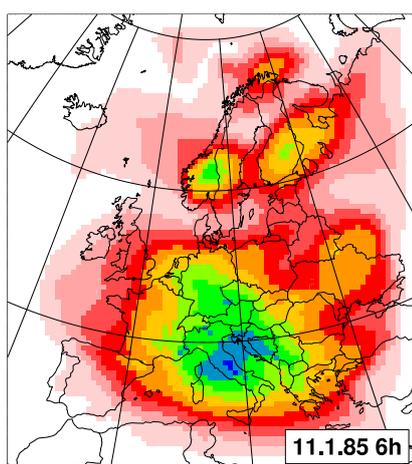
(c) Member 8

(d) MSLP internal variability (hPa)
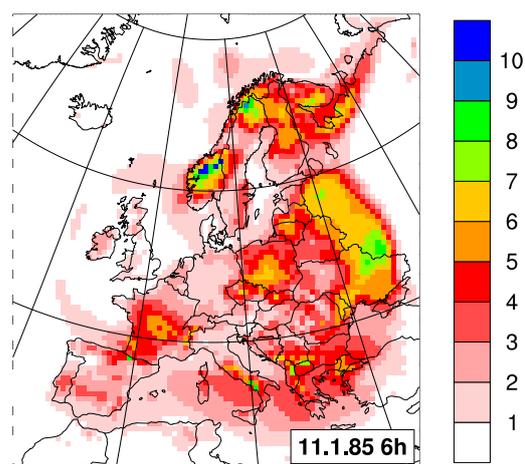
**(e)** NST internal variability (K)

Figure A.12: Case study 11.1.1985.
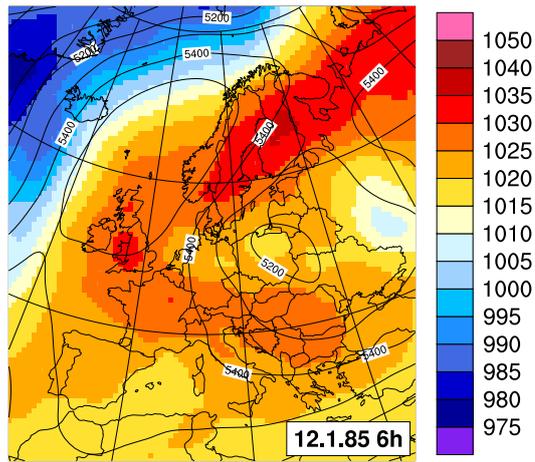
(a) Forcing
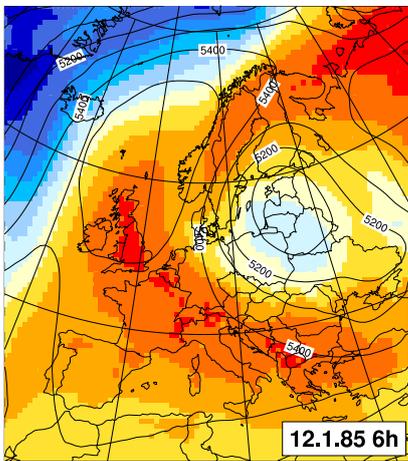
(b) Member 1
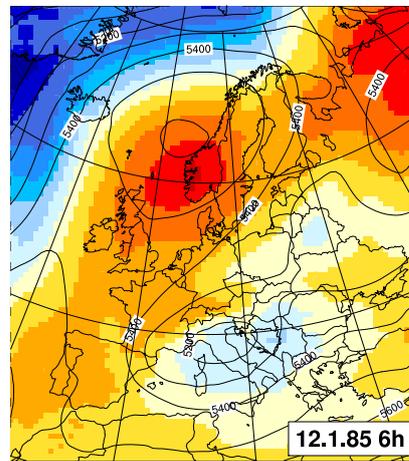
(c) Member 8
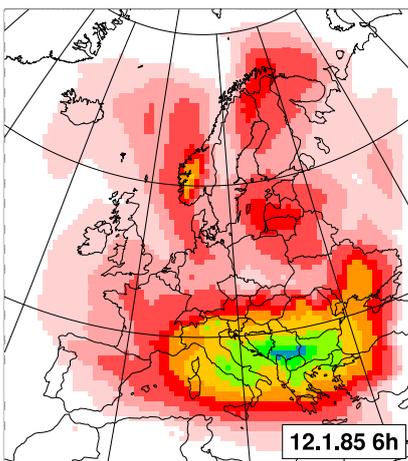
(d) MSLP internal variability (hPa)
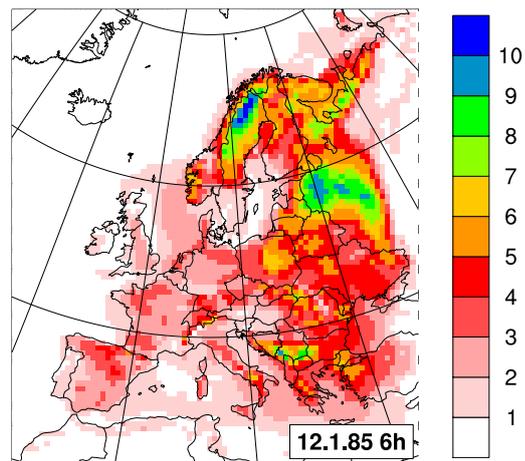
**(e)** NST internal variability (K)

Figure A.13: Case study 12.1.1985.

References

Alexandru, A., R. de Elia and R. Laprise (2007). Internal variability in regional climate downscaling at the seasonal scale. *Monthly Weather Review*, **135**(9), 3221–3238.

Arakawa, A. and V. Lamb (1977). Computational design and the basic dynamical processes of the UCLA general circulation Model. *Methods in Computational Physics*, **17**, 173–265.

Asselin, R. (1972). Frequency filter for time integrations. *Monthly Weather Review*, **100**, 487–490.

Beck, C. and A. Philipp (2010). Evaluation and comparison of circulation type classifications for the European domain. *Physics and Chemistry of the Earth*, **35**(9-12), 374–387.

Bellprat, O., S. Kotlarski, D. Luethi and C. Schaer (2012). Objective calibration of regional climate models. *Journal of Geophysical Research-atmospheres*, **117**, D23115.

Blessing, S., K. Fraedrich, M. Junge, T. Kunz and F. Lunkeit (2005). Daily North-Atlantic Oscillation (NAO) index: Statistics and its stratospheric polar vortex dependence. *Meteorologische Zeitschrift*, **14**(6), 763–769.

Bougeault, P. (1983). A Non-reflective Upper Boundary-condition For Limited-height Hydrostatic Models. *Monthly Weather Review*, **111**(3), 420–429.

Braun, M., D. Caya, A. Frigon and M. Slivitzky (2012). Internal Variability of the Canadian RCM's Hydrological Variables at the Basin Scale in Quebec and Labrador. *Journal of Hydrometeorology*, **13**(2), 443–462.

Brinkop, S. and E. Roeckner (1995). Sensitivity of a general circulation model to parameterizations of cloud-turbulence interactions in the atmospheric boundary layer. *Tellus Series A-Dynamic Meteorology and Oceanography*, **47**(2), 197–220.

Caya, D. and S. Biner (2004). Internal variability of RCM simulations over an annual cycle. *Climate Dynamics*, **22**(1), 33–46.

Christensen, O. B., M. A. Gaertner, J. A. Prego and J. Polcher (2001). Internal variability of regional climate models. *Climate Dynamics*, **17**(11), 875–887.

Collins, M., S. F. B. Tett and C. Cooper (2001). The internal climate variability of HadCM3, a version of the Hadley Centre coupled model without flux adjustments. *Climate Dynamics*, **17**(1), 61–81.

Cretat, J., C. Macron, B. Pohl and Y. Richard (2011). Quantifying internal variability in a regional climate model: a case study for Southern Africa. *Climate Dynamics*, **37**(7-8), 1335–1356.

Cretat, J. and B. Pohl (2012). How Physical Parameterizations Can Modulate Internal Variability in a Regional Climate Model. *Journal of the Atmospheric Sciences*, **69**(2), 714–724.

D'Andrea, F., S. Tibaldi, M. Blackburn, G. Boer, M. Deque, M. R. Dix, B. Dugas, L. Ferranti, T. Iwasaki, A. Kitoh, V. Pope, D. Randall, E. Roeckner, D. Straus, W. Stern, H. Van den Dool and D. Williamson (1998). Northern Hemisphere atmospheric blocking as simulated by 15 atmospheric general circulation models in the period 1979-1988. *Climate Dynamics*, **14**(6), 385–407.

Davies, H. C. (1976). A lateral boundary formulation for multi-level prediction models. *Quarterly Journal of the Royal Meteorological Society*, **102**, 405–418.

de Boor, C. (1978). A practical guide to splines. Springer New York, 392 pp.

Demuzere, M., M. Werner, N. P. M. van Lipzig and E. Roeckner (2009). An analysis of present and future ECHAM5 pressure fields using a classification of circulation patterns. *International Journal of Climatology*, **29**(12), 1796–1810.

Deque, M., D. P. Rowell, D. Luthi, F. Giorgi, J. H. Christensen, B. Rockel, D. Jacob, E. Kjellstrom, M. de Castro and B. van den Hurk (2007). An intercomparison of regional climate simulations for Europe: assessing uncertainties in model projections. *Climatic Change*, **81**, 53–70.

Deser, C., A. Phillips, V. Bourdette and H. Teng (2012). Uncertainty in climate change projections: the role of internal variability. *Climate Dynamics*, **38**(3-4), 527–546–.

Diaconescu, E. P., R. Laprise and A. Zadra (2012). Singular vector decomposition of the internal variability of the Canadian Regional Climate Model. *Climate Dynamics*, **38**(5-6), 1093–1113.

Donat, M. G., G. C. Leckebusch, J. G. Pinto and U. Ulbrich (2010). European storminess and associated circulation weather types: future changes deduced from a multi-model ensemble of GCM simulations. *Climate Research*, **42**(1), 27–43.

Fouquart, Y. and B. Bonnel (1980). Computations of solar heating of the Earth's atmosphere: a new parameterization. *Contributions to Atmospheric Physics*, **53**(1), 35–62.

Franzke, C., T. Woollings and O. Martius (2011). Persistent Circulation Regimes and Preferred Regime Transitions in the North Atlantic. *Journal of the Atmospheric Sciences*, **68**(12), 2809–2825.

Gerstengarbe, F. W. and P. C. Werner (2005). Katalog der Großwetterlagen Europas (1881-2004) nach Paul Hess und Helmut Brezowsky, 6., verbesserte und ergänzte Auflage. PIK Reports 100, Potsdam Institute for Climate Impact Research (PIK).

Giorgi, F. and X. Q. Bi (2000). A study of internal variability of a regional climate model. *Journal of Geophysical Research-Atmospheres*, **105**(D24), 29503–29521.

Göttel, H. (2009). Einfluss der nichthydrostatischen Modellierung und der Niederschlagsverdriftung auf die Ergebnisse regionaler Klimamodellierung. PhD thesis, MPI-MET.

Hagedorn, R., F. J. Doblas-Reyes and T. N. Palmer (2005). The rationale behind the success of multi-model ensembles in seasonal forecastingI. Basic concept. *Tellus Series A-Dynamic Meteorology and Oceanography*, **57**(3), 219–233.

Hagemann, S., B. Machenhauer, R. Jones, O. Christensen, M. Déqué, D. Jacob and P. Vidale (2004). Evaluation of water and energy budgets in regional climate models applied over Europe. *Climate Dynamics*, **23**(5), 547–567.

Hartigan, J. (1975). Clustering Algorithms. Wiley Series in Probability and Mathematical Statistics.

Hasselmann, K. (1976). Stochastic Climate Models .1. Theory. *Tellus*, **28**(6), 473–485.

Hess, P. and H. Brezowsky (1952). Katalog der Großwetterlagen Europas. Technical report, Deutscher Wetterdienst in der US-Zone, Bad Kissingen, Germany.

Holton, J. R. (2004). An Introduction to Dynamic Meteorology, Vol. 88 of *International Geophysics Series*. Elsevier Academic Press, 4th edition, 535 pp.

Hurrell, J. W., Y. Kushnir, G. Ottersen and M. Visbeck (eds.) (2003). The North Atlantic Oscillation: Climatic Significance and Environmental Impact, Vol. 134. AGU, Washington, DC, 279 pp.

Huth, R. (1996). An intercomparison of computer-assisted circulation classification methods. *International Journal of Climatology*, **16**(8), 893–922.

Huth, R., C. Beck, A. Philipp, M. Demuzere, Z. Ustrnul, M. Cahynova, J. Kysely and O. E. Tveito (2008). Classifications of Atmospheric Circulation Patterns Recent Advances and Applications. *Trends and Directions In Climate Research*, **1146**, European Meteorol Soc.

Jacob, D. (2009). Regional climate models: linking global climate change to local impacts, chapter Climate Modeling, Global Warming and Weather Prediction, pp. 7591–7602. Springer.

Jacob, D., H. Goettel, J. Jungclaus, M. Muskulus, R. Podzun and J. Marotzke (2005). Slowdown of the thermohaline circulation causes enhanced maritime climate influence and snow cover over Europe. *Geophys. Res. Lett.*, **32**(21), L21711.

Jacob, D. and R. Podzun (1997). Sensitivity studies with the regional climate model REMO. *Meteorol. Atmos. Phys.*, **63**(1-2), 119–129.

Jacob, D., B. J. J. M. Van den Hurk, U. Andrae, G. Elgered, C. Fortelius, L. P. Graham, S. D. Jackson, U. Karstens, C. Kopken, R. Lindau, R. Podzun, B. Rockel, F. Rubel, B. H. Sass, R. N. B. Smith and X. Yang (2001). A comprehensive model inter-comparison study investigating the water budget during the BALTEX-PIDCAP period. *Meteorology and Atmospheric Physics*, **77**(1-4), 19–43.

James, P. M. (2007). An objective classification method for Hess and Brezowsky Grosswetterlagen over Europe. *Theoretical and Applied Climatology*, **88**(1-2), 17–42.

Jones, P. D., T. J. Osborn and K. R. Briffa (2003). Pressure-based measures of the North Atlantic Oscillation (NAO): A comparison and an assessment of changes in the strength of the NAO and in its influence on surface climate parameters. In *Geophys. Monogr. Ser.*, Vol. 134, pp. 51–62. AGU, Washington, DC.

Klemp, J. B. and D. R. Durran (1983). An Upper Boundary-condition Permitting Internal Gravity-wave Radiation In Numerical Mesoscale Models. *Monthly Weather Review*, **111**(3), 430–444.

Kotlarski, S., D. Jacob, R. Podzun and F. Paul (2010). Representing glaciers in a regional climate model. *Climate Dynamics*, **34**(1), 27–46.

Langmann, B. (2000). Numerical modelling of regional scale transport and photochemistry directly together with meteorological processes. *Atmospheric Environment*, **34**(21), 3585–3598.

Laprise, R., R. de Elia, D. Caya, S. Biner, P. Lucas-Picher, E. Diaconescu, M. Leduc, A. Alexandru and L. Separovic (2008). Challenging some tenets of Regional Climate Modelling. *Meteorology and Atmospheric Physics*, **100**(1-4), 3–22.

Laprise, R., D. Kornic, M. Rapaic, L. Separovic, M. Leduc, O. Nikiema, A. D. Luca, E. Diaconescu, A. Alexandru, P. Lucas-Picher, R. de Elia, D. Caya and S. Biner (2012). Climate Change, chapter Considerations of Domain Size and Large-Scale Driving for Nested Regional Climate Models: Impact on Internal Variability and Ability at Developing Small-Scale Details, p. 244. Springer-Verlag Wien.

Louis, J. F. (1979). Parametric Model of Vertical Eddy Fluxes In the Atmosphere. *Boundary-layer Meteorology*, **17**(2), 187–202.

Lucas-Picher, P., D. Caya, S. Biner and R. Laprise (2008a). Quantification of the Lateral Boundary Forcing of a Regional Climate Model Using an Aging Tracer. *Monthly Weather Review*, **136**(12), 4980–4996.

Lucas-Picher, P., D. Caya, R. de Elia and R. Laprise (2008b). Investigation of regional climate models' internal variability with a ten-member ensemble of 10-year simulations over a large domain. *Climate Dynamics*, **31**(7-8), 927–940.

Majewski, D. (1991). The Europa-Modell of the Deutscher Wetterdienst. In *ECMWF*, Vol. 2 of *ECMWF Seminar on numerical methods in atmospheric models*, pp. 147–191.

Morcrette, J. . J., L. Smith and Y. Fouquart (1986). Pressure and temperature dependence of the absorption in longwave radiation parameterizations. *Contributions to Atmospheric Physics*, **59**(4), 455–69.

Nikiema, O. and R. Laprise (2011). Diagnostic budget study of the internal variability in ensemble simulations of the Canadian RCM. *Climate Dynamics*, **36**(11-12), 2313–2337.

Nordeng, T. E. (1994). Extended versions of the convective parametrization scheme at ECMWF and their impact on the mean and transient activity of the model in the tropics. Technical Memorandum 206, ECMWF.

Palmer, T. N. and P. D. Williams (eds.) (2009). Stochastic Physics and Climate Modelling. Cambridge University Press, 496 pp.

Pfeifer, S. (2006). Modeling cold cloud processes with the regional climate model REMO. PhD thesis, Max Planck Institute for Meteorology.

Philipp, A., J. Bartholy, C. Beck, M. Erpicum, P. Esteban, X. Fettweis, R. Huth, P. James, S. Jourdain, F. Kreienkamp, T. Krennert, S. Lykoudis, S. C. Michalides, K. Pianko-Kluczynska, P. Post, D. Rasilla Alvarez, R. Schiemann, A. Spekat and F. S. Tymvios (2010). Cost733cat-A database of weather and circulation type classifications. *Physics and Chemistry of the Earth*, **35**(9-12), 360–373.

Philipp, A., P. M. Della-Marta, J. Jacobeit, D. R. Fereday, P. D. Jones, A. Moberg and H. Wanner (2007). Long-term variability of daily North Atlantic-European pressure patterns since 1850 classified by simulated annealing clustering. *Journal of Climate*, **20**(16), 4065–4095.

Pietikäinen, J.-P., D. O'Donnell, C. Teichmann, U. Karstens, S. Pfeifer, J. Kazil, R. Podzun, S. Fiedler, H. Kokkola, W. Birmili, C. O'Dowd, U. Baltensperger, E. Weingartner, R. Gehrig, G. Spindler, M. Kulmala, J. Feichter, D. Jacob and A. Laaksonen (2012). The regional aerosol-climate model REMO-HAM. *Geoscientific Model Development*, **5**(6), 1323–1339.

Pinto, J. G., S. Zacharias, A. H. Fink, G. C. Leckebusch and U. Ulbrich (2009). Factors contributing to the development of extreme North Atlantic cyclones and their relationship with the NAO. *Climate Dynamics*, **32**(5), 711–737.

Plavcova, E. and J. Kysely (2011). Evaluation of daily temperatures in Central Europe and their links to large-scale circulation in an ensemble of regional climate models. *Tellus Series A-dynamic Meteorology and Oceanography*, **63**(4), 763–781.

Rechid, D. (2009). On biogeophysical interactions between vegetation phenology and climate simulated over Europe. PhD thesis, Max Planck Institute for Meteorology.

Rechid, D. and D. Jacob (2006). Influence of monthly varying vegetation on the simulated climate in Europe. *Meteorologische Zeitschrift*, **15**(1), 99–116.

Rinke, A. and K. Dethloff (2000). On the sensitivity of a regional Arctic climate model to initial and boundary conditions. *Climate Research*, **14**(2), 101–113.

Roeckner, E., K. Arpe, L. Bengtsson, M. Christoph, M. Claussen, L. Dümenil, M. Esch, M. Giorgetta, U. Schlese and U. Schulzweida (1996). The atmospheric general circulation model ECHAM-4: Model description and simulation of present-day climate. Report 218, Max Planck Institute for Meteorology, Hamburg.

Semmler, T. (2002). Der Wasser- und Energiehaushalt der arktischen Atmosphäre. PhD thesis, Max Planck Institute for Meteorology.

Simmons, A. and D. Burridge (1981). An Energy and Angular-Momentum Conserving Vertical Finite-Difference Scheme and Hybrid Vertical Coordinates. *Monthly Weather Review*, **109**(4), 758–766.

SRES (2000). Special Report on Emission Scenarios. Cambridge University Press, 608 pp.

Stephenson, D. B., H. Wanner, S. Brönnimann and J. Luterbacher (2003). The history of scientific research on the North Atlantic Oscillation. In *Geophys. Monogr. Ser.*, Vol. 134, pp. 37–50. AGU, Washington, DC.

Stier, P., J. Feichter, S. Kinne, S. Kloster, E. Vignati, J. Wilson, L. Ganzeveld, I. Tegen, M. Werner, Y. Balkanski, M. Schulz, O. Boucher, A. Minikin and A. Petzold (2005). The aerosol-climate model ECHAM5-HAM. *Atmospheric Chemistry and Physics*, **5**, 1125–1156.

Sundqvist, H. (1978). Parameterization Scheme For Non-convective Condensation Including Prediction of Cloud Water-content. *Quarterly Journal of the Royal Meteorological Society*, **104**(441), 677–690.

Tebaldi, C. and R. Knutti (2007). The use of the multi-model ensemble in probabilistic climate projections. *Philosophical Transactions of the Royal Society A: Mathematical, Physical and Engineering Sciences*, **365**(1857), 2053–2075.

Teichmann, C. (2009). Climate and Air Pollution Modelling in South America with focus on Megacities. PhD thesis, International Max Planck Research School on Earth System Modelling.

Thompson, D. W. J., S. Lee and M. P. Baldwin (2003). Atmospheric processes governing the Northern Hemisphere annular mode/North Atlantic Oscillation. In *Geophys. Monogr. Ser.*, Vol. 134, pp. 81–112. AGU, Washington, DC.

Tiedtke, M. (1989). A Comprehensive Mass Flux Scheme For Cumulus Parameterization In Large-scale Models. *Monthly Weather Review*, **117**(8), 1779–1800.

Timmreck, C. (2012). Modeling the climatic effects of large explosive volcanic eruptions. *Wiley Interdisciplinary Reviews: Climate Change*, **3**(6), 545–564.

Uppala, S. M., P. W. Kallberg, A. J. Simmons, U. Andrae, V. D. Bechtold, M. Fiorino, J. K. Gibson, J. Haseler, A. Hernandez, G. A. Kelly, X. Li, K. Onogi, S. Saarinen, N. Sokka, R. P. Allan, E. Andersson, K. Arpe, M. A. Balmaseda, A. C. M. Beljaars, L. Van De Berg, J. Bidlot, N. Bormann, S. Caires, F. Chevallier, A. Dethof, M. Dragosavac, M. Fisher, M. Fuentes, S. Hagemann, E. Holm, B. J. Hoskins, L. Isaksen, P. A. E. M. Janssen, R. Jenne, A. P. McNally, J. F. Mahfouf, J. J. Morcrette, N. A. Rayner, R. W. Saunders, P. Simon, A. Sterl, K. E. Trenberth, A. Untch, D. Vasiljevic, P. Viterbo and J. Woollen (2005). The ERA-40 re-analysis. *Quarterly Journal of the Royal Meteorological Society*, **131**(612), 2961–3012.

Vuuren, D., J. Edmonds, M. Kainuma, K. Riahi, A. Thomson, K. Hibbard, G. Hurtt, T. Kram, V. Krey, J.-F. Lamarque, T. Masui, M. Meinshausen, N. Nakicenovic, S. Smith and S. Rose (2011). The representative concentration pathways: an overview. *Climatic Change*, **109**(1-2), 5–31.

Wallace, J. M., Y. Zhang and K. H. Lau (1993). Structure and Seasonality of Interannual and Interdecadal Variability of the Geopotential Height and Temperature-fields In the Northern-hemisphere Troposphere. *Journal of Climate*, **6**(11), 2063–2082.

Weisse, R., H. Heyen and H. von Storch (2000). Sensitivity of a regional atmospheric model to a sea state-dependent roughness and the need for ensemble calculations. *Monthly Weather Review*, **128**(10), 3631–3642.

Woollings, T., A. Hannachi and B. Hoskins (2010a). Variability of the North Atlantic eddy-driven jet stream. *Quarterly Journal of the Royal Meteorological Society*, **136**(649), 856–868.

Woollings, T., A. Hannachi, B. Hoskins and A. Turner (2010b). A Regime View of the North Atlantic Oscillation and Its Response to Anthropogenic Forcing. *Journal of Climate*, **23**(6), 1291–1307.

Acknowledgements

First and foremost, I would like to thank my supervisor Daniela Jacob for supporting my choice of a thesis topic. I would also like to thank her for sharing her thoughts in the most constructive manner and for her strength to keep the group together during the difficult times. My thanks to Martin Claußen for giving me the opportunity to pursue my doctoral studies at the Max Planck Institute for Meteorology and reviewing my thesis. A very special thank-you goes to Ralf Podzun who always had time for my questions and provided invaluable advice for all sorts of REMO problems that arose. Unfortunately, he left us well before his time. My thanks to Joaquim Pinto for providing the daily NAO data and fruitful discussion on the results. I would also like to thank Jürgen Bader for the many hours he spent to discuss my work and for the helpful suggestions.

An office full of laughter makes for the best work environment and I would like to thank Claas for sharing his great sense of humor. I would like to thank the REMO group of MPI and the climate system group of CSC for their support and for making both institutes places where I like to be. I would also thank Thomas, Christine, Alberto, Laura, and Florian for introducing me the world of *Gewaltkicker* and improving my skills of trash-talking. My thanks to the entire MPI football team for all the fun we had at practices, the game or two we won per season, and for all the beers after the game. Many thanks to my lunch crew from the wind tunnel who showed me how to find the funniest short clips on youtube in the most efficient way. A special thank goes to Frank. His only weakness is his choice for a Bundesliga team, but other than that he is a great support in all circumstances.

I would like to thank my family for their great support over all these years, for their patience, and for always believing in me. Last but not least I would like thank Christine for her support and encouragement, for struggling through this thesis trying to diminish the misuse of her language, and for simply being there.